Circuit quantum acoustodynamics with surface acoustic waves

Riccardo Manenti

Brasenose College, Oxford

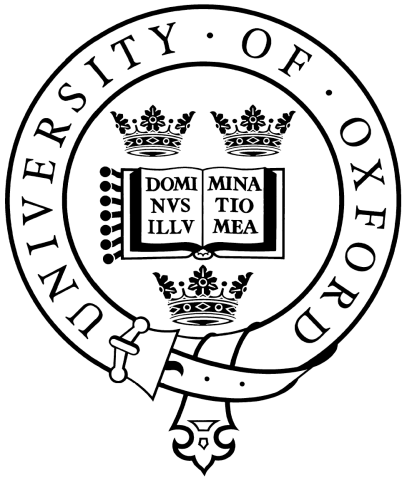

Trinity Term 2017

Supervised by Dr. Peter Leek

Clarendon Laboratory

University of Oxford

Circuit quantum acoustodynamics with surface acoustic waves

Riccardo Manenti, Brasenose College, University of Oxford

Trinity Term 2017

Abstract of thesis submitted for the degree of Doctor of Philosophy

A highly successful architecture for the exchange of single quanta between coupled quantum systems is circuit quantum electrodynamics (QED), in which the electrical interaction between a qubit and a high-quality microwave resonator offers the possibility to reliably control, store, and read out quantum bits of information on a chip. This architecture has also been implemented with mechanical resonators, showing that a vibrational mode can in principle be manipulated via a coupled qubit. The work presented in this thesis consists of realising an acoustic version of circuit QED that we call circuit quantum acoustodynamics (QAD), in which a superconducting qubit is piezoelectrically coupled to an acoustic cavity based on surface acoustic waves (SAWs).

Designing and building this novel platform involved the following main accomplishments: a systematic characterisation of SAW resonators at low temperatures; successfully developing a recipe for the fabrication of Josephson junction on quartz and diamond; measuring the coherence time of superconducting 3D transmon qubits on these substrates and demonstrating the dispersive coupling between a SAW cavity and a qubit on a planar geometry.

This thesis presents evidence of the coherent interaction between a SAW cavity and a superconducting qubit in several ways. First of all, a frequency shift of the mechanical mode as a function of qubit frequency is observed. We also measure the acoustic Stark shift of the qubit due to the population of the SAW cavity. The extracted coupling is in agreement with theoretical expectations. A time delayed acoustic Stark shift serves to further demonstrate that the Stark shifts that we observe are indeed due to the acoustic field of the SAW mode. The dispersive coupling between these two quantum systems offers the possibility to perform qubit spectroscopy using the SAW resonator as readout component, indicating that these acoustic resonators can, in principle, be adopted as an alternative qubit readout scheme in quantum information processors. We finally present preliminary measurements of the direct coupling between a SAW resonator and a transmon on diamond, suggesting that strong coupling can in principle be obtained.

Contents

Chapter 1

Introduction

If everything is made up of little particles and all little particles follow quantum mechanics, then shouldn't everything just follow quantum mechanics?

At the beginning of the last century when the theory of quantum mechanics was first proposed by W. Heisenberg [37] and E. Schrödinger [82], the principal intent was to explain the physics of the hydrogen atom in a non-relativistic context. As the years passed by, numerous phenomena, such as black body radiation and atomic emission spectra, were convincingly explained by quantum mechanics. The increasing number of experimental results in favour of the new theory raised some fundamental questions regarding its domain of applicability: Do macroscopic objects behave according to the laws of quantum mechanics? Can a macroscopic object be prepared in a superposition state?

One possible approach to answer these questions is to perform quantum mechanical tests on systems with mesoscopic dimensions. Young's double-slit experiment is a prime example of this line of research: firstly performed with electrons [42, 89], and neutrons [97], it was then implemented with objects of increasing size such as atoms [18] and giant molecules [63]. In the latter experiment, it was experimentally demonstrated that C_{60} molecules infringing against a double-slit recreate the interference

pattern typical of wave-like objects showing that even a molecule with a well defined inner geometry can be found in a superposition state of position. More recently, molecules with more than 800 atoms have shown a similar behaviour in agreement with quantum mechanical predictions [25].

Unfortunately, this approach cannot be easily extended to systems with larger dimensions and other techniques must be adopted. Nowadays, a common way to investigate quantum mechanics at a macroscopic level consists of selecting a mechanical vibrational mode of an object with resonance frequency in the range $0.1\,\mathrm{MHz} < f_\mathrm{m} < 10\,\mathrm{GHz}$ and probing it at millikelvin temperatures, where thermal fluctuations are strongly suppressed [73]. The mechanical resonators investigated under these conditions span a broad range of system sizes and resonance frequencies, from meter-scale mirrors used for gravitational wave detection in the 100 Hz range [1] to nanoscale structures that can reach resonance frequencies above 1 GHz [66, 19, 20]. Obtaining high quality (Q) factors in such resonators is typically much harder at higher frequencies [26, 40], though Q factors approaching 10^7 have recently been demonstrated at 3.6 GHz in a silicon nanobeam [58].

Two main strategies have been used to reach the quantum limit in mechanical systems. The first approach consists of measuring mechanical devices with relatively high frequencies $f_\mathrm{m} \approx 2\text{-}10\,\mathrm{GHz}$ at temperatures of the order of $T = 10\,\mathrm{mK}$. Under these conditions, the mechanical frequency is high enough to satisfy the requirement $hf_\mathrm{m} \gg k_\mathrm{B}T$. This implies that thermal phonons with average frequency $k_\mathrm{B}T/h \approx 0.2\,\mathrm{GHz}$ are not energetic enough to populate the levels of the mechanical resonator and the system is found in its quantum ground state. Another approach is to use mechanical devices with lower frequencies $f_\mathrm{m} < 1\,\mathrm{GHz}$ and higher quality factors. When measured at millikelvin temperatures, thermal phonons have enough energy to

populate the resonator levels. In order to actually reach the quantum ground state, the upper levels must be depopulated by actively cooling the device via sideband transitions [7].

The primary goal of these two techniques has been the demonstration of the quantum behaviour of macroscopic objects when suitably isolated from their environment. Pioneering work has now experimentally proven the possibility of preparing them close to their quantum ground state [88, 19] and coherently manipulating their state [66]. These results have encouraged new lines of research utilising mechanical quantum devices, including the development of microwave-optical converters [4], mechanical quantum memories [68] and quantum limited amplifiers [56], the generation of squeezed vacuum states of mechanical objects [94, 72], and the detection of non-classical correlations of photon-phonon pairs [76].

An interesting line of research concerning mechanical resonators in the quantum regime is their integration with superconducting devices. In this context, a highly successful architecture for the exchange of single quanta between coupled quantum systems is circuit quantum electrodynamics (QED) [92], in which the electrical interaction between a qubit and a high-quality microwave resonator offers the possibility to reliably control, store, and read out quantum bits of information on a chip. In recent years, theoretical and experimental investigations have transposed this technology to mechanical resonators, where a localised vibration is coupled to a superconducting qubit [45, 66, 71, 78] exploiting a circuit-QED type of interaction, which in principle enables full control of the quantum state of the mechanical mode via the qubit.

In contrast to these experiments involving localised mechanical modes, studies have also recently emerged on the coupling of superconducting qubits to traveling surface acoustic waves (SAWs) [34, 5], which are mechanical perturbations that prop-

agate on the surface of a crystal [62], and are naturally coupled to superconducting circuits using the piezoelectric effect. As well as being of fundamental interest to study such acoustic waves at the quantum level, they may find uses in quantum signal processing, since their slow speed of travel (five orders of magnitude slower than light) means many-wavelength signals can be manipulated on a mm-scale chip [5, 44]. It has been demonstrated that Fabry-Perot SAW cavities formed using superconducting surface Bragg mirrors can reach quality factors in the 10^5 range at microwave frequencies [52, 50], opening up the possibility of realising surface acoustic cavity QED, either with superconducting qubits, or with other solid-state quantum systems [83]. SAW cavities have also been proposed as a potential quantum acousto-optic transducer between superconducting qubits and optical photons by exploiting stimulated Brillouin scattering [84].

This thesis mainly focuses on the experimental investigation of SAW resonators in the quantum regime and their coupling to superconducting qubits [52]. Hereafter, we use the term SAW to mean a Rayleigh wave travelling on the surface of a crystal. Such acoustic vibrations can be excited in different ways: by means of a laser beam or, more commonly, by applying an oscillating voltage to the electrodes of a metallic interdigitated transducer (IDT) patterned on the surface of a piezoelectric crystal. The propagating SAW can eventually be confined in a small region of the chip by placing two reflectors on the two sides of the IDT. These reflectors consist of an array of shorted or open-circuit electrodes (or shallow grooves etched into the surface) to implement a half-wavelength period modulation of the impedance of the wave medium similar to a Bragg grating in optics. This configuration forms what is commonly known as a surface acoustic wave resonator (SAWR), the acoustic equivalent of a Fabry-Perot optical cavity. Since a SAW typically travels at a few km/s, res-

onators in the gigahertz range have μm-scale wavelengths, and devices can therefore be fabricated with standard lithographic techniques.

These acoustic resonators were first proposed in the 1970s by Ash [6] and have long been used in electrical engineering finding a wide range of applications in communications technology [62]. A detailed history and a thorough presentation of microwave devices based on SAW can be found in the comprehensive review by D. Morgan [61]. In the 1970s, the performance of SAW resonators at room temperature was investigated in detail by several authors [9, 87, 69] and the propagation loss of Rayleigh waves was measured in the 4.2 - 300 K range [15, 36], showing that the acoustic attenuation follows a ωT^4 dependence as predicted by Maradudin and Mills [53]. The insertion loss of SAW devices with frequencies up to 10 GHz has been measured at low temperatures [96] and high frequency devices in the range 12 - 16 GHz have been fabricated with different techniques, including nanoimprint lithography [17]. In recent years, traveling surface acoustic waves have been detected at the quantum level [35] and coupled to a superconducting qubit in an open transmission line configuration [34].

This thesis aims to present a systematic study of SAW resonator performance at millikelvin temperatures at or close to the quantum regime, showing how their geometry and design might affect the device internal loss. Furthermore, it presents measurements of the coherence time of superconducting qubits fabricated on quartz and diamond, two key materials in this field. Finally, it presents experimental results concerning a novel acoustic platform, in which a tuneable superconducting qubit is piezoelectrically coupled to a SAW resonator [51]. The interaction between the SAW cavity and the qubit is observed in several ways, including the acoustic Stark shift of the qubit and spectroscopic measurements of the qubit using the SAWR as readout

component. These measurements mimic the experiments performed a decade ago in circuit QED, the main difference being the acoustic nature of the cavity.

This thesis is divided in several chapters. In the second chapter, the theory of piezoelectricity is briefly presented. It follows a presentation of the frequency response of SAW resonators paying particular attention to their equivalent circuit. Chapter 3 is devoted to the experimental techniques employed to probe SAW resonators in the quantum regime. Chapter 4 reports an experimental study of SAW resonators at millikelvin temperatures, including a discussion on their internal quality factor as a function of drive power and several geometrical parameters. Chapter 5 includes a brief presentation of experiments conducted on superconducting qubits fabricated on quartz and diamond and tested with electromagnetic cavities. These results lead to Chapter 6, where the interaction between a SAW cavity and a transmon qubit on quartz and diamond is presented in detail, suggesting potential applications of this architecture in the field of quantum information processing.

Chapter 2

Theory of SAW devices

.

If a crystal has a center of symmetry,
then it is not piezoelectric.

2.1 Rayleigh waves

In nature, solids can be found in different shapes and geometries. At the two extremes, there are crystalline solids and amorphous solids. The former have internal constituents arranged according to a well-defined regular pattern. In contrast, amorphous solids instead do not have an ordered internal distribution of ions. Piezoelectric materials are crystalline solids with some special symmetries. In this section, we introduce some basic crystallographic concepts that will be useful to discuss piezoelectricity later on in the chapter.

Crystals

From X-ray diffraction experiments, it has been observed that crystals are not isotropic, i.e. their internal constituents are arranged along preferential axes. It has also been observed that they are homogenous[1], meaning that any microscopic

[1]Here, the terms isotropic and homogeneous are related to the inner geometry of the crystals, and not to their optical properties.

Figure 2.1 | **Lattice.** **a,** Representation of a 2-dimensional regular lattice. **b,** Example of a 2-dimensional lattice with symmetry A_2, A_3 and A_6.

region of the crystal has similar surroundings. From a theoretical point of view, these properties can be better appreciated by introducing the abstract concept of unit cell and lattice. A unit cell is a region in space containing one or more lattice points that defines the symmetry and structure of the body. The repetitive translation of a unit cell along some preferential axes forms the entire lattice which can be intuitively visualised as a three dimensional grid of points.

A lattice point O can be regarded as the origin of a coordinate system (see Fig. 2.1a). Any point of the lattice can be obtained from O by operating a rigid translation along a combination of three fixed vectors $\mathbf{a}$, $\mathbf{b}$ and $\mathbf{c}$, where we assume that the lattice extends indefinitely. The position of a lattice point P is specified by the vector:

$$\mathbf{OP} = n_1\mathbf{a} + n_2\mathbf{b} + n_3\mathbf{c},$$

where n_1, n_2, $n_3 \in \mathbb{Z}$.

A lattice might be invariant with respect to a specific geometrical transformation. For instance, a 180° rotation of a lattice around a line passing through the origin might generate a lattice identical to the original one (see Fig. 2.1b). This is an example of a rotational symmetry (specifically A_2) and the line around which the rotation is performed is called a symmetry axis. The most important rotational symmetries are listed below:

$$
\begin{array}{rrrl}
I = A_1 & \text{identity} & 360^\circ & \text{rotation} \\
A_2 & \text{dyad} & 180^\circ & \text{rotation} \\
A_3 & \text{triad} & 120^\circ & \text{rotation} \\
A_4 & \text{tetrad} & 90^\circ & \text{rotation} \\
A_6 & \text{hexad} & 60^\circ & \text{rotation}
\end{array}
$$

where A_n indicates that a rotation of $360^\circ/n$ around a particular axis leaves the lattice unchanged. Rotational symmetries are sometimes called direct symmetries. Note that n successive applications of A_n are equal to the identity: $(A_n)^n = I$.

An ideal crystal is a repetition of identical structural units in three dimensional space. The periodicity is described by a mathematical lattice and an atomic group, i.e. a specific arrangement of the atoms in a unit cell of the lattice:

$$\text{crystal} \quad = \quad \text{lattice} \quad + \quad \text{atomic group.}$$

In the simplest atomic group, a single atom is placed at each node of the lattice. This is the case for several crystals with so-called face-centered cubic lattices such as gold, aluminium and nickel, in which a cubic cell contains four atoms at coordinates (0, 0, 0), (1/2, 1/2, 0), (1/2, 0 ,1/2), and (0, 1/2, 1/2).

Crystals are classified according to their symmetries. There are, in total, seven crystal systems: triclinic, monoclinic, orthorhombic, trigonal, tetragonal, hexagonal and cubic. These are called primitive lattices and their unit cell is a parallelepiped. The lattices belonging to one of these crystal systems share the same group of symmetries. It is possible to create new lattices by adding extra nodes to the cells of these primitive lattices, as long as the environment of each node is invariant. Performing this procedure leads to the 14 Bravais lattices shown in Fig. 2.2. The Bravais lattices represent all of the possible ways of arranging an infinite number of nodes in space such that they all have the same environment. Note that quartz, an important material in the field of SAW devices, belongs to the trigonal system.

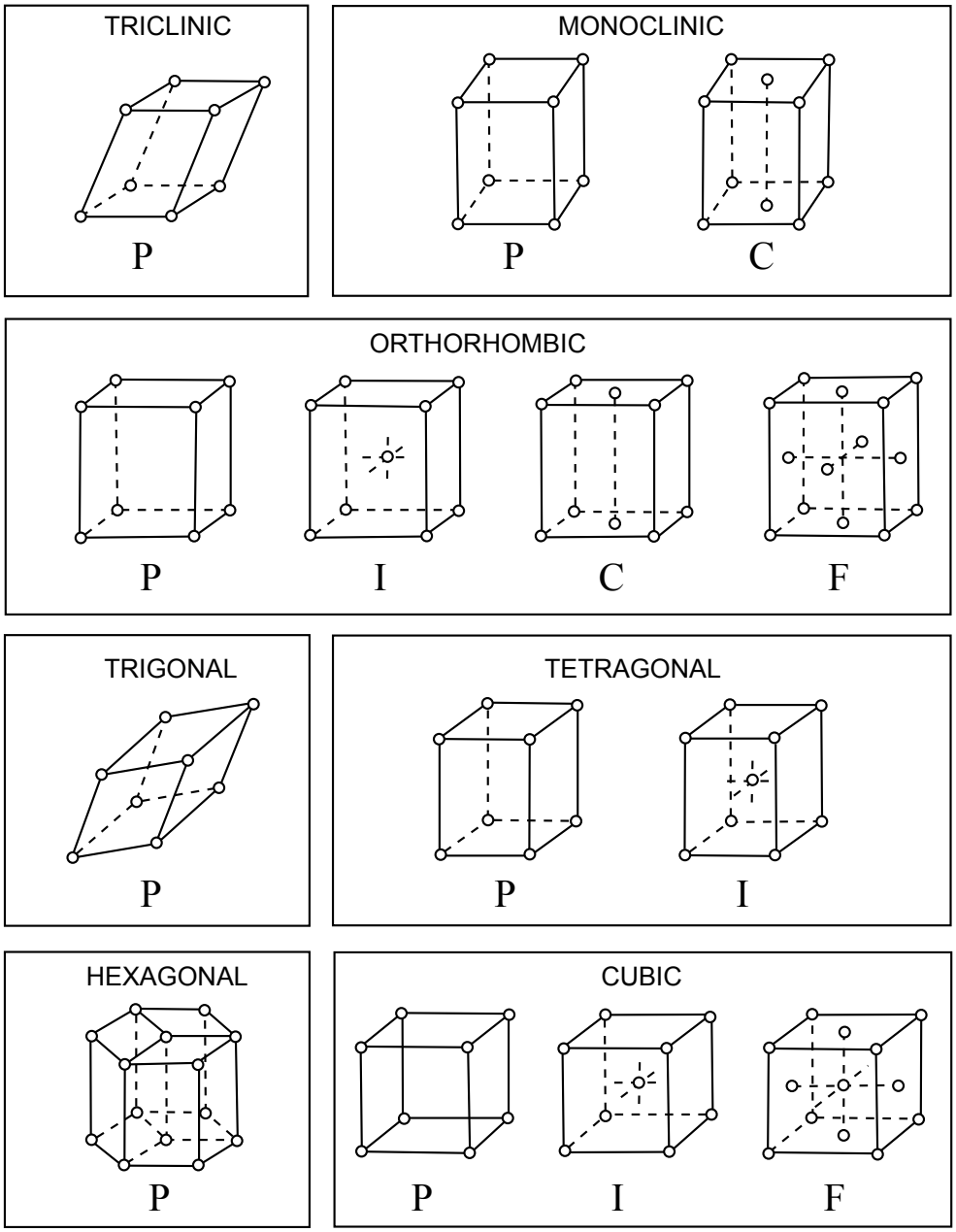

Figure 2.2 | The fourteen Bravais lattices. The letter P stands for primitive. Letters F and C indicate face-centered lattices. Letter I instead denotes a body-centered lattice.

Elasticity

A solid deforms when subjected to external mechanical forces. When this happens, the interatomic distances are altered from their initial values and the microscopic as well as macroscopic appearance of the body might significantly change. If a solid tends to naturally restore its original geometrical shape, it is said to behave elastically.

When an external electric field is applied to many solids, they undergo mechanical compressions proportional to the modulo square of the applied electric field. This commonplace phenomenon is called electrostrictive coupling and it is a weak second order effect. By contrast, the rarer phenomenon of piezoelectricity is a linear effect present in crystalline materials with certain symmetries that couples external electric fields to mechanical motions within an elastic body. If the spatial periodicity of the mechanical perturbations is longer than the interatomic distances, the solid can be mathematically modelled as a continuum and its internal mechanical state can be described by two tensorial fields: the strain field and the stress field. We now introduce these two fields and their relations.

Strain

The concept of strain can be understood by considering a simple example. Suppose that an external force is applied to a rope so that its length changes from the initial value L to L'. In such a case, the normalised elongation $(L' - L)/L$ is a dimensionless quantity indicating how much the rope length has changed compared to its initial value. Unfortunately, elongation is a global quantity that does not give detailed information about the local behaviour within the the body. For this reason, it is convenient to introduce a local elongation, called *strain*, that takes into account the fact that mechanical forces might induce contractions as well as elongations in

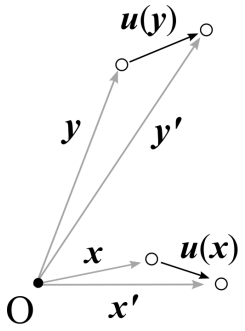

Figure 2.3 | Displacement. Two geometric points $\mathbf{x}$, $\mathbf{y}$ within a crystal are displaced due to an external mechanical force.

different parts of the body.

The mathematical definition of strain can be introduced in the following way. Consider two points close together $\mathbf{x} = (x_1, x_2, x_3)^{\mathrm{T}}$, $\mathbf{y} + \mathrm{d}\mathbf{x} = (y_1, y_2, y_3)$ and suppose that an external force is applied to the solid (see Fig. 2.3). These two points will move to the new positions $\mathbf{x}' = (x_1', x_2', x_3')^{\mathrm{T}} = \mathbf{x} + \mathbf{u}(\mathbf{x})$, $\mathbf{y}' = (y_1', y_2', y_3') = \mathbf{y} + \mathbf{u}(\mathbf{y})$, where we have defined the displacement field:

$$\mathbf{u}(\mathbf{x}) = \mathbf{x}' - \mathbf{x}.$$

This vector field indicates the magnitude and direction of the local displacement. For weak mechanical forces, the displacement vectors $\mathbf{u}(\mathbf{x})$, $\mathbf{u}(\mathbf{y})$ are similar to each other. To first order, the following approximation is valid:

$$u_i(y_j) = u_i(x_j + \mathrm{d}x_j) = u_i(x_j) + \left(\frac{\partial u_i}{\partial x_j}\right)_{x_j} dx_j.$$

The subscript indicates the component of the corresponding vector. If the solid undergoes a global translation, then $\partial u_i/\partial x_j = 0$. On the other hand, when the solid experiences a mechanical deformation $\partial u_i/\partial x_j \neq 0$. We would be tempted to define the local elongation as the dimensionless quantity $\partial u_i/\partial x_j$. However, this would not be a wise choice. In fact, when a solid is rotated around an axis, no internal mechanical deformations are generated and yet the term $\partial u_i/\partial x_j$ is different from

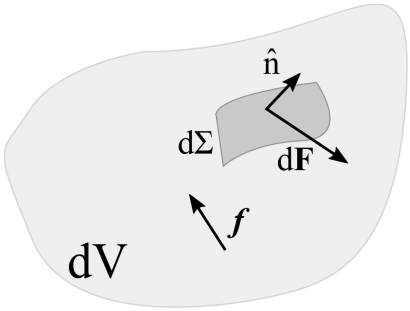

Figure 2.4 | Representative elementary volume. Little volume within a solid subject to an external mechanical force d**F** and internal forces **f**.

zero. To overcome this issue, we can write the Jacobian $\partial u_i/\partial x_j$ as the sum of two terms:

$$J_{ij}(\mathbf{x}) = \frac{\partial u_i(\mathbf{x})}{\partial x_j} = A_{ij}(\mathbf{x}) + S_{ij}(\mathbf{x}),$$

where $A_{ij}(\mathbf{x}) = [\partial u_i(\mathbf{x})/\partial x_j - \partial u_j(\mathbf{x})/\partial x_i]/2$ is an antisymmetric tensor and:

$$\boxed{S_{ij}(\mathbf{x}) = \frac{1}{2}\left(\frac{\partial u_i(\mathbf{x})}{\partial x_j} + \frac{\partial u_j(\mathbf{x})}{\partial x_i}\right)} \tag{2.1}$$

S_{ij} is a symmetric tensor and it represents the local elongation or *strain*. This mathematical definition of strain is consistent with S_{ij} being null both for overall translations and rotations. Furthermore $S_{ij} = S_{ji}$, which implies that only six of the nine components are independent. Note that, in general, the strain tensor is time dependent.

Stress

When an external mechanical force is exerted on the face of a solid, small deformations start propagating from the contact point to other regions of the body along well-defined surfaces. This phenomenon takes place because mechanical traction forces are generated that act to restore the mechanical equilibrium of the body. The origin of these forces are interactions between neighbouring ions.

Stress is the generalised concept of force within a body. Its mathematical definition can be introduced in the following way. Consider a little volume $\mathrm{d}V$ in a solid and define a surface vector $\mathrm{d}\mathbf{\Sigma} = \mathrm{d}\Sigma s\,\hat{n}$ with $\hat{n}$ being a unit vector pointing towards the outside of the volume. Suppose that a local force $\mathrm{d}\mathbf{F}$ is applied to the little volume. The traction force $\mathbf{R}$ is defined as:

$$\mathbf{R}\left(\hat{n}\right) = \lim_{\mathrm{d}\Sigma \to 0} \frac{\mathrm{d}\mathbf{F}}{\mathrm{d}\Sigma},$$

where the vector $\mathbf{R}$ is not necessarily collinear to $\hat{n}$ (see Fig. 2.4). The resultant traction force $\mathbf{F}_\Sigma$ is given by a surface integral of the local vector $\mathbf{R}\left(\hat{n}\right)$ over the entire area enclosing the volume: $\mathbf{F}_\Sigma = \int_\Sigma \mathbf{R}\left(\hat{n}\right) \mathrm{d}\Sigma$. Within the solid, there exist some internal forces per unit volume that tend to counterbalance the traction forces (these internal forces $\boldsymbol{f}$ could be gravitational forces, for example). The resultant force due to these internal forces is given by $\mathbf{F}_V = \int_V \boldsymbol{f}\ \mathrm{d}V$. At mechanical equilibrium, traction and internal forces are balanced $\mathbf{F}_\Sigma = -\mathbf{F}_V$. This expression can be written in integral form:

$$\int_\Sigma R_i\left(\hat{n}\right) \mathrm{d}\Sigma = -\int_V f_i \mathrm{d}V. \tag{2.2}$$

It is always possible to express the internal forces f_i as the divergence of a *stress* tensor field, $f_i = -\left(\nabla \cdot \mathbf{T}\right)_i = -\partial_j T_{ij}$. Substituting this expression in equation (2.2) and applying the divergence theorem we obtain:

$$\int_\Sigma R_i\left(\hat{n}\right) d\Sigma = \int_V \left(\nabla \cdot \mathbf{T}\right)_i dV = \int_\Sigma \sum_j T_{ij} n_j d\Sigma,$$

from which follows:

$$\boxed{R_i\left(\hat{n}\right) = \sum_j T_{ij} n_j = T_{i1} n_1 + T_{i2} n_2 + T_{i3} n_3.}$$

This relation implies that the force per unit area R_i exerted on the surface of a little volume within a solid is given by $R_i = T_{ij} n_j$. In the particular case in which the

surface element $\mathrm{d}\mathbf{\Sigma}$ is collinear to one axis, we have $R_i(n_j) = T_{ij}$. In other words, the stress tensor entry T_{12} is the x component of the force per unit area acting on a surface perpendicular to the y axis. Note that if a solid is not subject to an applied torque, then the stress tensor is symmetric $T_{ij} = T_{ji}$.

Hooke's law

Hooke's law states that strains are proportional to stresses if the latter are small. In the one dimensional case, Hooke's law has the familiar form $\mathbf{F} = k\Delta\mathbf{x}$, where k is a spring constant. Within a solid, this law asserts that the stress tensor T_{ij} is proportional to the strain tensor S_{kl}:

$$\boxed{T_{ij} = c_{ijkl} S_{kl}}$$

where we have introduced the stiffness tensor c_{ijkl} :

$$\boxed{c_{ijkl} = \left(\frac{\partial T_{ij}}{\partial S_{kl}}\right)_{S_{kl}=0}}$$

The stiffness tensor is a 3-dimensional generalisation of the spring constant. It is a 4-rank tensor with $n^4 = 3^4$ components. The requirement $S_{kl} = S_{lk}$ translates into the condition $c_{ijkl} = c_{ijlk}$, which means that the number of independent components reduces to $n^4 - n^3(n-1)/2$. From the condition $T_{ij} = T_{ji}$, we have $c_{ijkl} = c_{jikl}$. This constraint further reduces the number of independent components to $n^4 - n^3(n-1)/2 - [n(n-1)]^2/2 = 36$. This also implies that two indices are sufficient to characterise the stiffness tensor[2]:

$$c_{\alpha\beta} \equiv c_{ijkl}, \qquad \alpha = (i,j) \quad \beta = (k,l),$$

[2]Hereafter, it is understood that latin indices vary in the range 1-3, while greek indices take values in the range 1-6.

where α and β are two indices with values between 1 and 6:

$$1 \leftrightarrow (11) \qquad 2 \leftrightarrow (22) \qquad 3 \leftrightarrow (33)$$

$$4 \leftrightarrow (23) = (32) \qquad 5 \leftrightarrow (31) = (13) \qquad 6 \leftrightarrow (12) = (21).$$

The stiffness tensor can thus be specified with a 6×6 matrix $c_{\alpha\beta}$. From thermodynamic considerations, it is possible to show that the stiffness tensor satisfies the condition:

$$c_{ijkl} = c_{klij},$$

i.e. $c_{\alpha\beta} = c_{\beta\alpha}$. This implies that only $(2n)^2 - n\,(2n-1) = 21$ components are actually independent and the matrix form of $c_{\alpha\beta}$ can be written as:

$$c_{\alpha\beta} = c_{\beta\alpha} = \begin{bmatrix} c_{11} & c_{12} & c_{13} & c_{14} & c_{15} & c_{16} \\ c_{12} & c_{22} & c_{23} & c_{24} & c_{25} & c_{26} \\ c_{13} & c_{23} & c_{33} & c_{34} & c_{35} & c_{36} \\ c_{14} & c_{24} & c_{34} & c_{44} & c_{45} & c_{46} \\ c_{15} & c_{25} & c_{35} & c_{45} & c_{55} & c_{56} \\ c_{16} & c_{26} & c_{36} & c_{46} & c_{56} & c_{66} \end{bmatrix}.$$

The symmetries of a crystal reduce the number of independent components of the stiffness tensor. For example, the stiffness tensor of an isotropic body has only two independent components:

$$c_{ijkl} = \lambda\delta_{ik}\delta_{kl} + \mu\left(\delta_{ik}\delta_{jl} + \delta_{il}\delta_{jk}\right) = \begin{bmatrix} c_{11} & c_{12} & c_{12} & 0 & 0 & 0 \\ c_{12} & c_{11} & c_{12} & 0 & 0 & 0 \\ c_{12} & c_{12} & c_{11} & 0 & 0 & 0 \\ 0 & 0 & 0 & c_{66} & 0 & 0 \\ 0 & 0 & 0 & 0 & c_{66} & 0 \\ 0 & 0 & 0 & 0 & 0 & c_{66} \end{bmatrix}, \tag{2.3}$$

where $c_{11} = \lambda + 2\mu$, $c_{12} = \lambda$, $c_{66} = \mu$ and λ, μ are called Lamé constants. On the other hand, it can be shown that the stiffness tensor of lattices in the trigonal system has the form:

$$c_{\alpha\beta} = \begin{bmatrix} c_{11} & c_{12} & c_{13} & c_{14} & 0 & 0 \\ c_{12} & c_{11} & c_{13} & -c_{14} & 0 & 0 \\ c_{13} & c_{13} & c_{33} & 0 & 0 & 0 \\ c_{14} & -c_{14} & 0 & c_{44} & 0 & 0 \\ 0 & 0 & 0 & 0 & c_{44} & c_{14} \\ 0 & 0 & 0 & 0 & c_{14} & \frac{c_{11}-c_{12}}{2} \end{bmatrix}$$

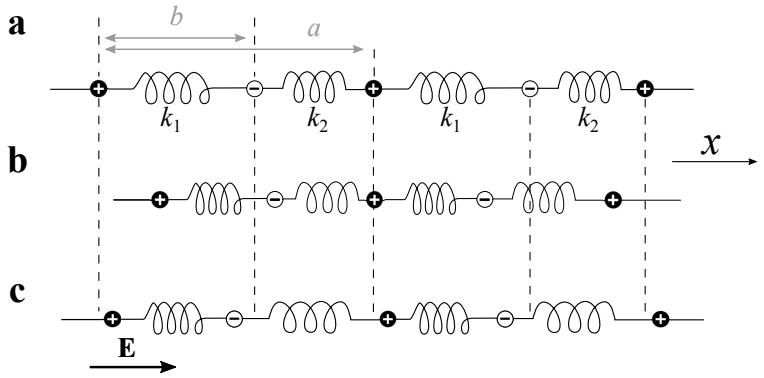

Figure 2.5 | Zinc-Oxide model. Chain of Zinc-Oxide ions at rest (**a**), when subjected to mechanical compression (**b**), when subject to an external electric field collinear to the chain (**c**). The elastic forces between ions are represented by springs.

and the stiffness tensor for quartz is given by:

$$c_{\alpha\beta} = \begin{bmatrix} 87.26 & 6.57 & 11.95 & -17.18 & 0 & 0 \\ 6.57 & 87.26 & 11.95 & 17.18 & 0 & 0 \\ 11.95 & 11.95 & 105.8 & 0 & 0 & 0 \\ -17.18 & 17.18 & 0 & 57.15 & 0 & 0 \\ 0 & 0 & 0 & 0 & 57.15 & -17.18 \\ 0 & 0 & 0 & 0 & -17.18 & 40.34 \end{bmatrix}$$

where the numerical values were taken from [38] and are expressed in GPa. These values refer to natural α-quartz at 22 °C and 10^{-3} Torr.

Piezoelectricity

A solid is piezoelectric if an applied mechanical compression electrically polarises it (direct effect) and if an external electric field mechanically deforms it (Lippman effect). The direct effect was observed for the first time by Pierre Curie and Jacques Curie in 1880, whereas the inverse effect was predicted by Gabriel Lippman the following year.

Piezoelectricity can be understood by considering the dynamics of zinc oxide when subjected to an external electric field. Crystal of zinc oxide are formed from alternating layers of zinc and oxygen ions. Lines perpendicular to these layers alternately intersect the two ions as shown in Fig. 2.5. At equilibrium, the ions are well localised

and their interactions can be qualitatively modelled with elastic restoring forces with spring constants k_1 and k_2. The electric polarisation of the material is given by:

$$\mathbf{P}_0 = n\ \mathbf{p}_0 = n \sum_i q_i\ \mathbf{d}_i = n\frac{q}{2}\,(a - 2b)\ \ \hat{\mathbf{u}}_x,$$

where $\mathbf{d}$ is a spatial vector connecting a negatively charged element to a positively charged element in a unit cell, a and b are the two distances shown in Fig. 2.5a and n is the volumetric density of ZnO diatomic elements. Suppose that the body is subject to a mechanical compression along the x axis, which reduces the lengths a and b by the amounts Δa and Δb respectively (see Fig. 2.5b). Due to this mechanical force, the variation of polarisation is:

$$\mathbf{P} = n\frac{q}{2}\,(\Delta a - 2\Delta b)\,\hat{\mathbf{u}}_x. \tag{2.4}$$

This is the direct piezoelectric effect: a mechanical deformation generates a variation of the material's polarisation.

If an external electric field $\mathbf{E}$ is applied along the x axis, it will move the zinc and oxygen ions in two opposite directions (they have opposite charge distributions, see Fig. 2.5c). At equilibrium, the forces sum up to zero, $-\,(k_1 + k_2)\,\Delta b\ \hat{\mathbf{u}}_x = qE\ \hat{\mathbf{u}}_x - k_1 \Delta a\ \hat{\mathbf{u}}_x$, which implies:

$$\Delta b = -\frac{qE}{k_1 + k_2} + \frac{k_1}{k_1 + k_2}\Delta a. \tag{2.5}$$

We can substitute this expression into equation (2.4) to obtain[3]:

$$\mathbf{P} = \frac{nq^2}{k_1 + k_2} E\ \hat{\mathbf{u}}_x + \frac{nq\,(k_2 - k_1)}{2\,(k_1 + k_2)}\Delta a\ \hat{\mathbf{u}}_x = \chi_{\text{ion}}\mathbf{E} + e\ \mathbf{S}.$$

The first term is proportional to the electric field and the proportionality constant is the ionic susceptibility $\chi_{\text{ion}} = nq^2/\,(k_1 + k_2)$. The second term expresses the direct

[3]In this simple example, both χ_{ion} and e are scalar quantities. As we shall see later, in three dimensions these quantities are expressed with tensors.

piezoelectric effect and includes both the strain $\mathbf{S} = \Delta a/a\ \hat{\mathbf{u}}_x$ and the piezoelectric constant:

$$e = \frac{nq\,(k_2 - k_1)}{2\,(k_1 + k_2)} a. \tag{2.6}$$

If we also take into account the electronic susceptibility χ_e, the overall polarisation reads $\mathbf{P} = (\chi_\mathrm{ion} + \chi_\mathrm{e})\ \mathbf{E} + e\ \mathbf{S}$ and the electric displacement vector can be written:

$$\boxed{\mathbf{D} = \varepsilon\ \mathbf{E} + e\ \mathbf{S},} \tag{2.7}$$

where $\varepsilon = \varepsilon_0 + \chi_\mathrm{ion} + \chi_\mathrm{e}$. This is one of the fundamental equations of the piezoelectric effect: the displacement vector is not only proportional to the electric field but also to strain.

Finally, we can relate stress to the applied electric field. The chain shown in Fig. 2.5 indefinitely extends in the x direction. In ZnO, there are an infinite number of collinear chains and half of them will be shifted by half a period along the x direction. This means that a plane perpendicular to the x axis intersects an equal number of springs with spring constant k_1 and k_2. The force per unit area exerted on this perpendicular plane is given by

$$\mathbf{T} = \frac{na}{2}\left(k_2 \Delta b\ \mathbf{u}_x + k_1 \Delta\,(a - b)\ \ \mathbf{u}_x\right).$$

If the displacements Δb, Δa are due to an external electric field, expression (2.5) still holds and the stress reduces to

$$\boxed{\mathbf{T} \ = \ na\frac{k_1 k_2}{k_1 + k_2}\Delta a\ \hat{\mathbf{u}}_x \ \ - \frac{nq}{2}\frac{k_2 - k_1}{k_1 + k_2} E\ \hat{\mathbf{u}}_x \ = c\ \mathbf{S} - e\ \mathbf{E},} \tag{2.8}$$

where in the second term we recognise the piezoelectric constant e equation (2.6) and we have defined the stiffness coefficient $c = na^2 k_1 k_2/\,(k_1 + k_2)$. The second term $-e\ \mathbf{E}$ expresses the inverse effect: an applied electric field produces internal stresses within a solid.

The relations (2.7)-(2.8) are the fundamental equations of the piezoelectric behaviour of a solid. They can be generalised to three dimensions in the following way:

$$D_i = \varepsilon_{ij}^S E_j + e_{ijk}\, S_{jk} \tag{2.9}$$

$$T_{ij} = c_{ijkl}^E S_{kl} - e_{kij}\, E_k, \tag{2.10}$$

where ε_{ij}^S is the dielectric tensor and e_{ijk} is the 3-rank piezoelectric tensor. The superscripts S and E indicate that the quantities are evaluated keeping the strain or electric field constant, respectively. The formal definition of piezoelectric tensor is:

$$\boxed{\varepsilon_{ijk} = \left(\frac{\partial D_i}{\partial S_{jk}}\right)_E}$$

This is a 3-rank tensor with 27 components. Since $S_{jk} = S_{kj}$, it follows that:

$$\varepsilon_{ijk} = \varepsilon_{ikj}.$$

This condition reduces the number of independent components from 27 to $n^3 - 3n = 18$. The last two indices form a pair that can take only six distinct values. This means that only two indices are needed to describe this tensor:

$$e_{i\alpha} \equiv e_{ijk} \qquad \text{where} \quad i \in \{1,2,3\} \quad \alpha \in \{1,2,3,4,5,6\}\,.$$

The piezoelectric tensor can be expressed as a 3×6 matrix:

$$e_{i\alpha} = \begin{bmatrix} e_{11} & e_{12} & e_{13} & e_{13} & e_{15} & e_{16} \\ e_{21} & e_{22} & e_{23} & e_{24} & e_{25} & e_{26} \\ e_{31} & e_{32} & e_{33} & e_{34} & e_{35} & e_{36} \end{bmatrix}.$$

Depending on the symmetries of the crystal, the number of independent components might decrease.

The most important observation is probably the fact that the piezoelectric tensor of a crystal with a centre of symmetry is null. To see this, suppose that the crystal

is subject to an inversion with respect to a centre C:

$$\alpha_i^j\,(C) = \begin{pmatrix} -1 & 0 & 0 \\ 0 & -1 & 0 \\ 0 & 0 & -1 \end{pmatrix}.$$

If this transformation leaves the crystal unchanged, then the piezoelectric tensor must be invariant as well:

$$e_{ijk} = \alpha_i^p \alpha_j^q \alpha_k^r e_{pqr},$$

which implies $e_{ijk} = -e_{ijk}$, whence $e_{ijk} = 0$. In other words, **if a crystal has a centre of symmetry, then it is not piezoelectric**.

From symmetry considerations, it can be shown that the piezoelectric tensor for crystals in the 32 class of the trigonal system has only two independent components:

$$e_{i\alpha} = \begin{bmatrix} e_{11} & -e_{11} & 0 & e_{14} & 0 & 0 \\ 0 & 0 & 0 & 0 & -e_{14} & -e_{11} \\ 0 & 0 & 0 & 0 & 0 & 0 \end{bmatrix}.$$

Quartz belongs to this particular class and its piezoelectric tensor at room temperature is given by:

$$e_{i\alpha} = \begin{bmatrix} 0.171 & -0.171 & 0 & 0.041 & 0 & 0 \\ 0 & 0 & 0 & 0 & -0.041 & -0.171 \\ 0 & 0 & 0 & 0 & 0 & 0 \end{bmatrix},$$

where the numerical entries are expressed in $\mathrm{C/m^2}$. Note that the piezoelectric effect in quartz is quite weak compared to other materials, notably lithium niobate, in which the entries of e_{ijk} can reach values of $3\,\mathrm{C/m^2}$.

Waves in a piezoelectric crystal

In piezoelectric materials, mechanical variables are strictly related to electromagnetic fields. In order to study the internal dynamics of a solid, it would be necessary to solve a system of coupled equations involving the Newton and Maxwell relations. It must be noted, however, that the speed at which a mechanical perturbation travels

within a solid is approximately 10^5 smaller than the speed of electromagnetic waves and the magnetic field associated with the travelling wave gives only a small contribution to the mechanical perturbation. For this reason, we can make the assumption: $\nabla \times \mathbf{E} = -\partial \mathbf{B}/\partial t \approx 0$. This also implies that the electric field can be expressed in terms of the gradient of a scalar field, $E_i = \partial_i \phi$. On the other hand, the electric displacement obeys the usual relation $\partial_i D_i = \rho_\mathrm{e}$, where ρ_e are free charges eventually present inside the material.

We shall now derive a system of coupled equations which completely describes the internal dynamics of a piezoelectric crystal. First of all, consider Newton's law for a little volume within the crystal:

$$\rho \ddot{u}_i = \partial_j T_{ij}, \tag{2.11}$$

where each dot indicates a time derivative. Since $T_{ij} = c_{ijkl} S_{kl} - e_{kij} E_k$ and $S_{kl} = (\partial_k u_l + \partial_l u_k)/2$, the stress tensor can be written in the form:

$$T_{ij} = \frac{c_{ijkl}}{2} (\partial_k u_l + \partial_l u_k) - e_{kij} E_k = c_{ijkl} \partial_k u_l + e_{kij} \partial_k \phi,$$

where in the second step we used $c_{ijkl} = c_{ijlk}$ and $E_k = -\partial_k \phi$. Substituting this expression in equation (2.11), we finally obtain:

$$\rho \ddot{u}_i = c_{ijkl} \partial_j \partial_k u_l + e_{kij} \partial_j \partial_k \phi.$$

As regards the electric displacement, recall from equation (2.10) that $D_j = \varepsilon_{jk} E_k + e_{jkl} S_{kl}$. Let us suppose that there are no free charges within the volume ($\partial_j D_j = 0$). This implies:

$$\begin{aligned} \partial_j D_j &= \varepsilon_{jk} \partial_j E_k + e_{jkl} \partial_j S_{kl} = \\ &= -\varepsilon_{jk} \partial_j \partial_k \phi + \frac{e_{jkl}}{2} \partial_j (\partial_k u_l + \partial_l u_k) = \\ &= -\varepsilon_{jk} \partial_j \partial_k \phi + e_{jkl} \partial_j \partial_k u_l = 0 \end{aligned}$$

where we have used equation (2.1) and the fact that $e_{ijk} = e_{ikj}$. The system of coupled equations that we were looking for is:

$$\boxed{\begin{cases} \rho\ddot{u}_i = c_{ijkl}\partial_j\partial_k u_l + e_{kij}\partial_j\partial_k\phi \\ e_{jkl}\partial_j\partial_k u_l - \varepsilon_{jk}\partial_j\partial_k\phi = 0. \end{cases}} \tag{2.12}$$

This is a system of four coupled equations with four independent variables, namely u_1, u_2, u_3 and ϕ. It is possible to find analytical solutions of this coupled system in some special cases.

Bulk waves in a non-piezoelectric material

For the special case of a non-piezoelectric material, the system of coupled equations (2.12) reduces to:

$$c_{ijkl}\partial_j\partial_k u_l = \rho\ddot{u}_i. \tag{2.13}$$

The solution of these three equations are plane waves of the form:

$$u_i(\mathbf{x}, t) = A_i e^{i\omega(t - \hat{\mathbf{n}}\cdot\mathbf{x}/v)} = A_i e^{i\omega(t - n_j x_j/v)}.$$

Here, A_i is a polarisation vector, $\hat{\mathbf{n}}$ is the propagation direction and v_i is the speed of the perturbation. These three solutions are bulk waves propagating in the same direction $\hat{\mathbf{n}}$ with three distinct speeds v_i and polarisations A_i. The polarisation indicates the direction in which the displacement of the ions takes place. If the polarisation is in the same direction as the propagation, the correspondent wave is called *longitudinal wave*. If instead the polarisation is in a plane orthogonal to $\hat{\mathbf{n}}$, we refer to these waves as *transverse waves*. As we shall see later, transverse waves tend to have a slower speed than longitudinal waves. It might happen that the two transverse waves have the same speed: in this case the propagation direction is called *acoustic axis*. In general, the propagation direction $\hat{\mathbf{n}}$ will not be collinear to any component

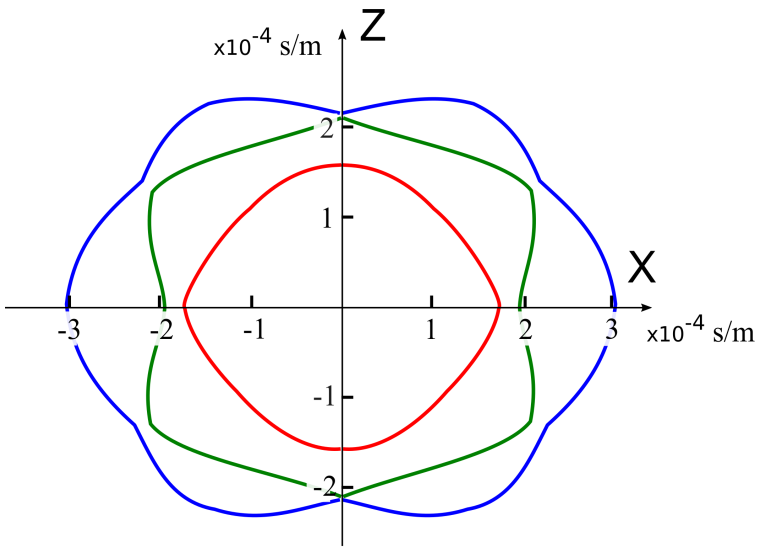

Figure 2.6 | Slowness curve. Quartz slowness curve in the XZ plane (readapted from [79]).

of the polarisation vector. Hence, the wave with polarisation closer to $\hat{\mathbf{n}}$ is called *quasi-longitudinal wave*, and the other two waves are called *quasi-transverse waves*.

We now derive the properties of longitudinal and transverse waves for a given propagation direction $\hat{\mathbf{n}}$. The time and spatial derivatives of the displacement field are given by:

$$\ddot{u}_i = -\omega^2 u_i, \qquad \partial_k u_l = -i\frac{\omega n_k}{v} u_l, \qquad \partial_j \partial_k u_l = -\frac{\omega^2 n_j n_k}{v^2} u_l.$$

Substituting these relations in equation (2.13), we arrive at $\rho v^2 A_i = c_{ijkl} n_j n_k A_l$. This expression can be written in a more convenient form as:

$$\boxed{\Gamma_{il} A_l = \rho v^2 A_i,} \tag{2.14}$$

where we have defined the Christoffel tensor $\Gamma_{il} = c_{ijkl} n_j n_k$. This eigenvalue equation is usually referred to as Christoffel equation and it is of paramount importance: for a fixed direction $\hat{\mathbf{n}}$, the phase velocities and polarisation of plane waves propagating along $\hat{\mathbf{n}}$ are given by the eigenvalues and eigenvectors of the symmetric tensor Γ_{il}.

We shall now derive the speed and polarisation of plane waves for quartz along specific directions. For the time being, we assume that the piezoelectric effect is negligible. Let us suppose that the plane waves are propagating along the x axis. In this case, $n_1 = 1$, $n_2 = 0$, $n_3 = 0$ and the Christoffel tensor becomes:

$$\Gamma_{il} = c_{i11l} = \begin{bmatrix} c_{1111} & c_{1112} & c_{1113} \\ c_{1112} & c_{2112} & c_{2113} \\ c_{1113} & c_{2113} & c_{3113} \end{bmatrix} = \begin{bmatrix} c_{11} & 0 & 0 \\ 0 & c_{66} & c_{14} \\ 0 & c_{14} & c_{44} \end{bmatrix}.$$

The characteristic polynomial of this matrix is $(c_{11} - \lambda)\left[(c_{66} - \lambda)(c_{44} - \lambda) - c_{14}^2\right] = 0$ with solution:

$$\lambda_{(1)} = c_{11} = 87.26\,\text{GPa}, \tag{2.15}$$

$$\lambda_{(2)} = \frac{1}{2}\left[c_{44} + c_{66} + \sqrt{(c_{66} - c_{44})^2 + 4c_{14}^2}\right] = 67.87\,\text{GPa}, \tag{2.16}$$

$$\lambda_{(3)} = \frac{1}{2}\left[c_{44} + c_{66} - \sqrt{(c_{66} - c_{44})^2 + 4c_{14}^2}\right] = 29.62\,\text{GPa}. \tag{2.17}$$

The speeds of the corresponding waves are given by $v_{\text{L}} = \sqrt{\lambda_{(1)}/\rho} = 5742\,\text{m/s}$, $v_{\text{T1}} = \sqrt{\lambda_{(2)}/\rho} = 5064\,\text{m/s}$, $v_{\text{T2}} = \sqrt{\lambda_{(3)}/\rho} = 3345\,\text{m/s}$, where we have used $\rho = 2647\,\text{Kg/m}^3$ for quartz. The corresponding eigenvectors A_1, A_2, A_3 give the polarisation directions[4]. Since the propagation was assumed to be along the x axis, the wave with vector polarisation A_1 and speed v_{L} is the longitudinal wave.

For a general direction, the components of the propagation direction $\hat{\mathbf{n}}$ can be expressed as $n_1 = \sin\theta$, $n_2 = \sin\theta\cos\phi$, $n_1 = \cos\theta$ and the Chistoffel tensor is given

[4]Equations (2.15)-(2.17) directly show that it is possible to estimate the components of the stiffness tensor by measuring the speed of plane waves along specific directions.

by:

$$\begin{aligned}
\Gamma_{11} &= c_{11}n_1^2 + c_{66}n_2^2 + c_{44}n_3^2 + 2c_{14}n_2n_3 \\
\Gamma_{12} &= (c_{12} + c_{66})\, n_1n_2 + 2c_{14}n_1n_3 \\
\Gamma_{13} &= 2c_{14}n_1n_2 + (c_{13} + c_{44})\, n_1n_3 \\
\Gamma_{22} &= c_{66}n_1^2 + c_{11}n_2^2 + c_{44}n_3^2 - 2c_{14}n_2n_3 \\
\Gamma_{23} &= c_{14}\left(n_1^2 - n_2^2\right) + (c_{13} + c_{44})\, n_2n_3 \\
\Gamma_{33} &= c_{44}\left(n_1^2 + n_2^2\right) + c_{33}n_3^2.
\end{aligned}$$

Depending on the angles ϕ and θ, it is sometimes necessary to adopt numerical models to find the eigenvalues of this tensor. If we set $\phi = \pi/2$ and solve this system of equations for a generic angle θ, we obtain the speed of sound in the XZ plane. Figure 2.6 shows the inverse of the sound speed in this plane; this curve is usually called *slowness curve*.

If we take into account the piezoelectric effect, the Christoffel equation changes slightly. In such a case, the system of coupled equations (2.12) has solutions:

$$u_i = A_i e^{i\omega(t - n_j x_j/v)}, \qquad \phi = \phi_0 e^{i\omega(t - n_j x_j/v)}.$$

The time and spatial derivatives of these plane waves are:

$$\ddot{u}_i = -\omega^2 u_i \qquad \partial_j\partial_k u_l = -\frac{\omega^2 n_j n_k}{v^2} u_l \qquad \partial_j\partial_k \phi = -\frac{\omega^2 n_j n_k}{v^2}\phi.$$

Substituting this expression in equation (2.12) we find:

$$\rho v^2 A_i = \Gamma_{il}A_l + \gamma_i\phi_0 \tag{2.18}$$

$$\phi_0 = \frac{\gamma_l}{\varepsilon}A_l \tag{2.19}$$

where we have defined $\Gamma_{il} = c_{ijkl}n_jn_k$, $\gamma_i = e_{kij}n_jn_k$ and $\varepsilon = \varepsilon_{jk}n_jn_k$. Substituting equation (2.19) into equation (2.18), we finally obtain the Christoffel equation for

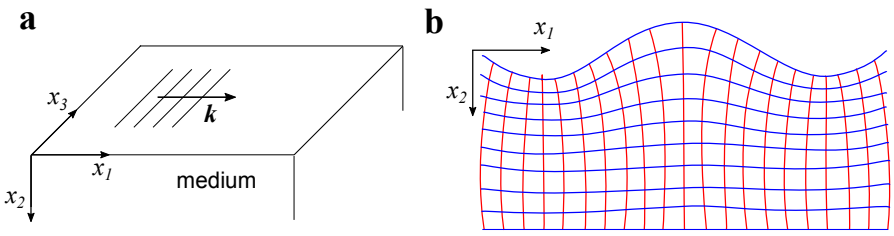

Figure 2.7 | Rayleigh waves. **a,** Orientation of the semi-infinite medium under consideration and surface acoustic waves. **b,** Section of a Rayleigh wave propagating on a semi-infinite medium.

piezoelectric materials:

$$\boxed{\rho v^2 A_i = \tilde{\Gamma}_{il} A_l}$$

where $\tilde{\Gamma}_{il} = \Gamma_{il} + \gamma_i \gamma_l / \varepsilon$. This eigenvalue equation has the same form as equation (2.14) with the substitution $\Gamma_{il} \to \tilde{\Gamma}_{il}$. For some crystals (such as quartz) the piezoelectric effect is so weak that the variation in the slowness curves is negligible.

Rayleigh waves

Rayleigh waves were described for the first time by Lord Rayleigh in 1885 [86]. These are acoustic waves propagating on the surface of a medium whose amplitude decreases exponentially inside the material. We derive their functional form for the special case of an isotropic material. More interesting cases, such as anisotropic piezoelectric materials, often requires numerical approaches. An analytical solution for GaAs can be found in the appendix of reference [83].

Newton's equation for a little volume close to the surface of an isotropic body is given by:

$$c_{ijkl} \partial_j \partial_k u_l = \rho \ddot{u}_i. \tag{2.20}$$

Let us suppose that the wave propagates in the x_1 direction and the normal to the surface is parallel to x_2 as shown in Fig. 2.7. The Rayleigh-type solutions we are

looking for have the form:

$$u_l(\mathbf{x},t) = A\ {}^{\circ}u_l\ e^{-\chi k x_2} e^{i(\omega t - k x_1)},$$

where χ is a positive constant and we are assuming that the wave has no variation along x_3. Here, A is the amplitude of the wave and ${}^{\circ}u_l$ the corresponding polarisation. Solving equation (2.20) with this ansatz will give us three (physical) values χ_r. To each χ_r corresponds a polarisation of the wave ${}^{\circ}\mathbf{u}^{(r)}$. The final solution will be a linear superposition of the form:

$$u_l(\mathbf{x},t) = \sum_{r=1}^{3} \left[A_r\ {}^{\circ}u_l^{(r)} e^{-\chi_r k x_2} \right] e^{i(\omega t - k x_1)}, \tag{2.21}$$

Let us first calculate the values χ_r. The linear operators can be written as: $\partial_1 = -ik$, $\partial_2 = -\chi k$, $\partial_3 = 0$ and $\partial_t^2 = -\omega^2$. Substituting these expressions into equation (2.20), we obtain:

$$\left[-c_{i11l} - c_{i22l} (i\chi)^2 + (c_{i12l} + c_{i21l})(i\chi) \right] u_l = -\rho v^2 u_l, \tag{2.22}$$

where we have defined $v^2 = \omega^2/k^2$. This is the usual Christoffel equation with $\Gamma_{il} = c_{i11l} + c_{i22l}(i\chi)^2 - (c_{i12l} + c_{i21l})(i\chi)$. For an isotropic material, the stiffness tensor has only few components different from zero [see equation (2.3)]. Hence, equation (2.22) becomes:

$$\begin{bmatrix} c_{11} + c_{66}(i\chi)^2 - \rho v^2 & -(c_{12} + c_{66})(i\chi) & 0 \\ -(c_{12} + c_{66})(i\chi) & c_{66} + c_{22}(i\chi)^2 - \rho v^2 & 0 \\ 0 & 0 & c_{66} + c_{66}(i\chi)^2 - \rho v^2 \end{bmatrix} \begin{pmatrix} u_1 \\ u_2 \\ u_3 \end{pmatrix} = 0.$$

Non-trivial solutions can be found by calculating the determinant of this matrix and setting it to zero. This 6^{th} order equation will give us the values of χ_r in terms of the speed of sound. Since the coefficients of the powers of $(i\chi)$ are real, the solutions will be three pairs of complex conjugates χ_r. Only three of them (the ones with $\chi_r > 0$) are physical. For each eigenvalue χ_r, we calculate the corresponding eigenvector ${}^{\circ}\mathbf{u}^{(r)}$,

which determines the polarisation of the wave. After some lengthy calculations (or few lines of Mathematica), we find[5]:

$$\begin{aligned} \chi_1 &= \sqrt{1 - v^2/v_{\mathrm{L}}^2} \qquad & {}^{\circ}\mathbf{u}^{(1)} &= (1, -i\chi_1, 0)^T \\ \chi_2 &= \sqrt{1 - v^2/v_{\mathrm{T}}^2} \qquad & {}^{\circ}\mathbf{u}^{(2)} &= (i\chi_2, 1, 0)^T, \end{aligned}$$

and from equation (2.21) we have

$$\begin{aligned} u_1(\mathbf{x}, t) &= \left[\quad A_1 e^{-\chi_1 k x_2} + i\chi_2 A_2 e^{-\chi_2 k x_2} \right] e^{i(\omega t - k x_1)}, \\ u_2(\mathbf{x}, t) &= \left[-i\chi_1 A_1 e^{-\chi_1 k x_2} + \quad A_2 e^{-\chi_2 k x_2} \right] e^{i(\omega t - k x_1)}. \end{aligned}$$

The last parameters that have to be determined are the speed of sound v and the ratio A_2/A_1. These quantities can be found by setting some boundary conditions to the stress tensor. At the interface $x_2 = 0$, the stress tensor must be null: $T_{12} = T_{22} = T_{32} = 0$. Since $T_{ij} = \partial_k c_{ijkl} u_l$, this implies:

$$T_{ij} = c_{ij11}\partial_1 u_1 + c_{ij12}\partial_1 u_2 + c_{ij21}\partial_2 u_1 + c_{ij22}\partial_2 u_2.$$

The conditions $T_{12}|_{x_2=0} = T_{22}|_{x_2=0} = 0$ thus become:

$$\begin{aligned} c_{66}\left(\partial_1 u_2 + \partial_2 u_1\right)|_{x_2=0} &= 0 \\ c_{21}\partial_1 u_1 + c_{22}\partial_2 u_2|_{x_2=0} &= 0. \end{aligned}$$

In the isotropic case, these constraints read:

$$\begin{aligned} \begin{pmatrix} 2\chi_1 & i\left(1+\chi_2^2\right) \\ i\left(-c_{21} + c_{22}\chi_1^2\right) & \chi_2\left(c_{21} - c_{22}\right) \end{pmatrix} \begin{pmatrix} A_1 \\ A_2 \end{pmatrix} &= \\ = \begin{pmatrix} 2\chi_1 & i\left(1+\chi_2^2\right) \\ i\mu\left(1+\chi_2^2\right) & -2\mu\chi_2 \end{pmatrix} \begin{pmatrix} A_1 \\ A_2 \end{pmatrix} &= 0, \end{aligned} \tag{2.23}$$

[5]Recall from Section 2.1 that for an isotropic material $c_{11} = \lambda + 2\mu$, $c_{12} = \lambda$, $c_{66} = \mu$, $v_{\mathrm{T}}^2 = \mu/\rho$ and $v_{\mathrm{L}}^2 = (\lambda + 2\mu)/\rho$. Furthermore, χ_3 has not been considered, since we assumed that the wave has no variation along x_3.

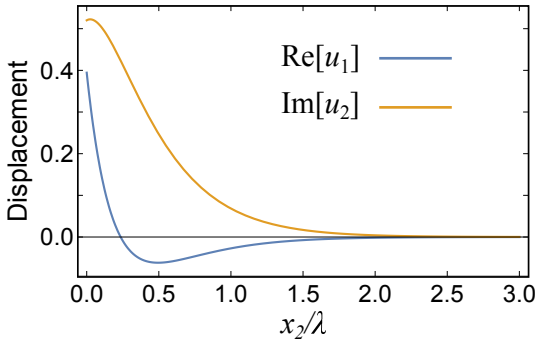

Figure 2.8 | Mechanical displacement due to a Rayleigh wave. a, Displacement of the particles in proximity of the surface of the medium along x_1 and x_2 assuming $A = 1$, $v_\mathrm{T} = 4100\,\mathrm{m/s}$ and $v_\mathrm{L} = 6050\,\mathrm{m/s}$ for fused quartz.

where we used $c_{21} - c_{22} = -2\mu$ and $-c_{21} + c_{22}\chi_1^2 = \mu\left(1 + \chi_2^2\right)$. This is a homogenous system of linear equations with variables A_1 and A_2. The determinant is given by:

$$\left(1 + \chi_2^2\right)^2 - 4\chi_1\chi_2 = 0. \tag{2.24}$$

Substituting the values of χ_1 and χ_2 into equation (2.24) we finally arrive at:

$$\boxed{\left(2 - \frac{v^2}{v_\mathrm{T}^2}\right)^4 = 16\left(1 - \frac{v^2}{v_\mathrm{L}^2}\right)\left(1 - \frac{v^2}{v_\mathrm{T}^2}\right)}$$

This equation has 8 solutions. Only one of them is positive and satisfies the condition $v < v_\mathrm{T}$. This solution is denoted as v_R and it represents the speed of the Rayleigh wave. Note that the value of $v_\mathrm{R}/v_\mathrm{T}$ is determined by the ratio $v_\mathrm{L}/v_\mathrm{T}$. This dependence is valid for any surface acoustic wave travelling on an isotropic material.

Combining equation (2.23) with (2.24), we can compute the ratio $A_2/A_1 = i\sqrt{\chi_1/\chi_2}$ and finally write the form of the displacement in proximity of the surface:

$$\begin{aligned} u_1\left(\mathbf{x}, t\right) &= \quad A_1\left[e^{-\chi_1 k x_2} - \sqrt{\chi_1\chi_2}e^{-\chi_2 k x_2}\right]e^{i(\omega t - k x_1)} \\ u_2\left(\mathbf{x}, t\right) &= iA_1\sqrt{\frac{\chi_1}{\chi_2}}\left[e^{-\chi_2 k x_2} - \sqrt{\chi_1\chi_2}e^{-\chi_1 k x_2}\right]e^{i(\omega t - k x_1)}. \end{aligned}$$

These displacements are in phase quadrature and are represented in Fig. 2.8. The particles close to the surface describe an ellipse whose shape and direction changes as a function of x_2.

2.2 SAW devices

Surface acoustic waves can be generated by applying an oscillating voltage to suitably shaped metallic structures deposited on the surface of a piezoelectric crystal. The simplest pattern consists of an interdigitated capacitor as shown in Fig. 2.9a; this device is called interdigitated transducer (IDT). The gap between adjacent fingers is usually denoted by a, whereas the distance between the centre of adjacent fingers is called p. The ratio between these two geometric parameters is called the metallisation ratio $\eta = a/p$. Finally, the periodicity of this interdigitated structure is denoted $\lambda_0 = 2p$.

When a voltage is applied to the electrodes of an IDT, an electric field is generated between adjacent fingers. In turn, this electric field produces compressions and expansions near the surface, giving rise to various elastic waves including Rayleigh waves. Each finger can thus be regarded as a source of acoustic perturbations. The generated wave reaches the neighbouring finger in a time $t_1 = p/v_R$, where v_R is the speed of the Rayleigh wave. If the oscillating voltage is periodic in time with period $T = 2t_1$, by the time the acoustic wave reaches the neighbouring finger, the voltage has changed sign and a stress add up constructively. The frequency of the corresponding wave $f_0 = v_\mathrm{R}/\lambda_0$ is usually called resonance frequency of the IDT.

The frequency response of an IDT can be studied using a discrete source model. In this model, each finger is considered to be a point-like source labelled by a discrete index $i = \{1, \ldots, N_\mathrm{t}\}$, where N_t is the number of fingers in the IDT. The position of each finger in the x-direction is denoted by x_i. The polarity P_i of each finger is equal to one (zero) if it is connected to a measurement port (ground). The acoustic

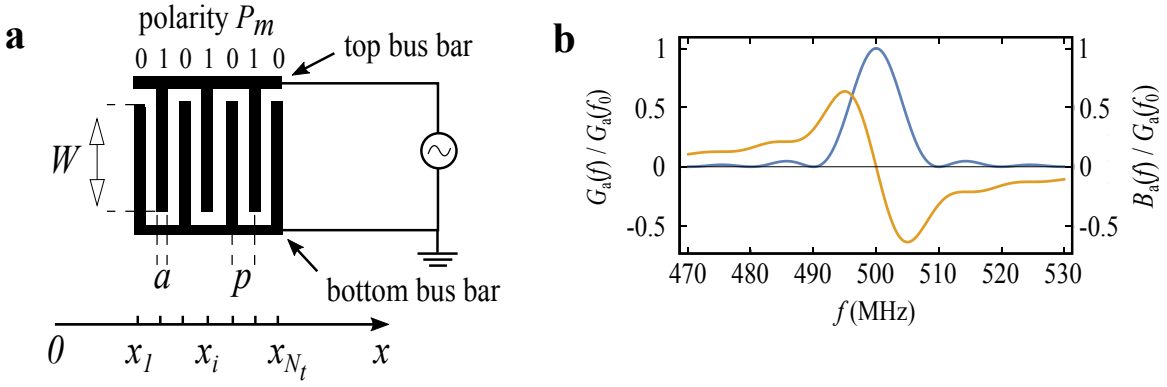

Figure 2.9 | **Transducer. a,** Interdigitated transducer for the generation and collection of SAWs. **b,** Conductance (blue curve) and susceptance (orange curve) of an IDT normalised with respect to $G_a(f_0)$, based on equation (2.27) with $N_\mathrm{p} = 50$ and $f_0 = 500\,\mathrm{MHz}$.

potential produced by the i-th finger of the IDT is given by:

$$\phi_i(x, f) = VE(\eta, f) P_i e^{jk(x-x_i)},$$

where V is the amplitude of the applied oscillating voltage, $j = \sqrt{-1}$, k is the wave number and $E(\eta, f)$ is an element factor that will be discussed later. Since the wave equation is linear, the acoustic potential at a fixed position $x = 0$ can be calculated as the sum of the waves generated by each finger:

$$\phi_S(0, f) = VE(\eta, f) \sum_{i=1}^{N_t} P_i e^{-jkx_i} = VE(\eta, f) A(f)$$

where we have defined the array factor:

$$A(f) = \sum_{i=1}^{N_\mathrm{t}} P_i e^{-jkx_i} = \sum_{m=1}^{N_\mathrm{t}/2} \left(e^{-2jkp}\right)^m = \frac{\sin(N_\mathrm{p} kp)}{\sin(kp)} e^{-jkp(N_\mathrm{p}+1)},$$

and we have introduced the number of fingers pairs in the IDT, $N_\mathrm{p} = N_\mathrm{t}/2$. We are interested in the absolute value of the array factor. Close to resonance, the wave number $k = 2\pi/\lambda$ is similar to $k \approx \pi/p$. Introducing the parameter $\theta = kp - \pi$, we find:

$$|A(f)| \approx \left|\frac{\sin[N_\mathrm{p}(\theta + \pi)]}{\theta}\right| = \left|\frac{\sin(N_\mathrm{p}\theta)}{\theta}\right| = N_\mathrm{p} \left|\frac{\sin X}{X}\right|.$$

The absolute value of the array factor is proportional to a sinc function with argument $X = N_\mathrm{p}\theta$. This simple model predicts an efficient transduction of the IDT centred around the harmonics of the resonance frequency f_0. Unfortunately, this model does not give any information about the prefactor $E(\eta, f)$. In order to calculate this term, a different approach based on a Green function formalism must be adopted. We present the analytical expression of the element factor $E(\eta, f)$ without going into the details of its derivation. By considering the electrical charge distribution on the fingers, theory predicts that this term has the following functional form [62]:

$$E(\eta, f) = j\frac{\Delta v}{v}\frac{2\sin(\pi s)}{P_{-s}(-\cos\Delta)}P_m(\cos\Delta), \qquad m \leq \frac{kp}{2\pi} \leq m+1, \tag{2.25}$$

where $s = -m + kp/2\pi$, $\Delta v/v$ is the coupling coefficient and $\Delta = \pi a/p$. In equation (2.25), $P_{-s}(x)$ is a Legendre function and $P_m(x)$ is a Legendre polynomial. The function $E(\eta, f)$ is plotted in Fig. 2.10a for different values of metallisation ratios η. Note that for $\eta = 0.5$, the element factor $E(\eta, f)$ at the first three harmonics is equal to:

$$\begin{aligned} E(0.5, f_0) &= 1.694j\frac{\Delta v}{v} \\ E(0.5, 2f_0) &= 0 \\ E(0.5, 3f_0) &= -1.694j\frac{\Delta v}{v}. \end{aligned}$$

Interestingly, the element factor is equal to zero at $f = 2f_0$. In other words, the frequency response of a regular single-electrode transducer is null at the second harmonic. However, for values of $\eta \neq 0.5$, the element factor is different from zero at $f = 2f_0$ and this property can be exploited to design transducers with good transduction at the second harmonic.

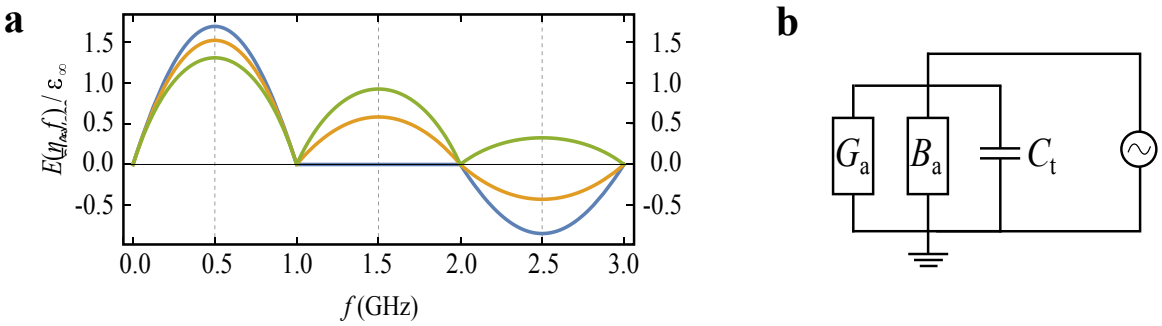

Figure 2.10 | Element factor and equivalent circuit. a, Element factor for a regular single-electrode transducer for different metallisation ratio: $\eta = 0.5$ (blue curve), $\eta = 0.4$ (orange curve) and $\eta = 0.275$ (green curve). **b,** Equivalent circuit of a transducer comprising a conductance G_a, an acoustic susceptance B_a and a geometric capacitance C_t.

Delay line

The behaviour of a regular single-electrode transducer can also be appreciated by considering its equivalent electrical circuit. This comprises three elements in parallel: a conductance $G(f)$, a susceptance $B(f)$ and a capacitance C (see Fig. 2.10b). The latter simply models the geometrical capacitance of the IDT and its analytical form is:

$$C_\mathrm{t} = W N_\mathrm{p} \epsilon_\infty, \tag{2.26}$$

where W is the overlap between the fingers of the IDT and ϵ_∞ is a material parameter. The conductance models the conversion of electrical energy into mechanical waves

$$G_a(f) = G_a(f_0) \left(\frac{\sin X}{X} \right)^2, \tag{2.27}$$

where $G_a(f_0) = 2.87 \epsilon_\infty W N_\mathrm{p}^2 2\pi f_0 \Delta v / v$. Finally, the susceptance can be derived as the Hilbert transform of the conductance

$$B_a(f) = G_a(f_0) \frac{\sin(2X) - X}{2X^2}.$$

The conductance and the susceptance are plotted in Fig. 2.9b. Finally, the admittance of a transducer can be written as:

$$Y_{11}(f) = G_a(f) + j B_a(f) + 2\pi j\, f\, C_\mathrm{t}. \tag{2.28}$$

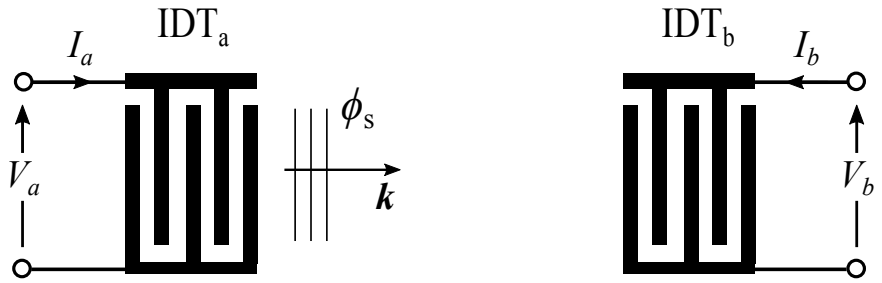

Figure 2.11 | **Delay line.** Delay line comprising two identical single-electrode IDTs.

The equivalent circuit of a transducer can be used to describe the frequency response of a delay line shown in Fig. 2.11. This device consists of two transducers facing each other. For simplicity, let us suppose that the transducers A and B are identical. This electrical network can be described with the following set of equations:

$$\begin{pmatrix} I_A \\ I_B \end{pmatrix} = \begin{pmatrix} Y_{11} & Y_{12} \\ Y_{21} & Y_{22} \end{pmatrix} \begin{pmatrix} V_A \\ V_B \end{pmatrix}$$

where Y_{ij} is the network admittance matrix, V_i is the voltage applied to transducer i and I_i is the short circuit current generated by the absorption of acoustic perturbations. Since we have assumed identical IDTs, $Y_{11} = Y_{22}$ and $Y_{12} = Y_{21}$. In a similar way, we can introduce the S-matrix:

$$\begin{pmatrix} V_{\text{out},A} \\ V_{\text{out},B} \end{pmatrix} = \begin{pmatrix} S_{11} & S_{12} \\ S_{21} & S_{22} \end{pmatrix} \begin{pmatrix} V_{\text{in},A} \\ V_{\text{in},B} \end{pmatrix}.$$

The entries S_{ij} are dimensionless numbers strictly related to Y_{ij}. In a typical experiment, the IDTs are connected to the ports of a vector network analyser (VNA) which measures the complex reflection/transmission coefficients S_{ij} as a function of frequency. These coefficients can be expressed as [74]:

$$S_{11}(f) = \frac{[Y_0 - Y_{11}(f)][Y_0 - Y_{22}(f)] + [Y_{12}(f)\,Y_{21}(f)]}{[Y_0 + Y_{11}(f)][Y_0 + Y_{22}(f)] - [Y_{12}(f)\,Y_{21}(f)]} \tag{2.29}$$

$$S_{12}(f) = \frac{-2Y_{12}(f)\,Y_0}{[Y_0 + Y_{11}(f)][Y_0 + Y_{22}(f)] - [Y_{12}(f)\,Y_{21}(f)]}. \tag{2.30}$$

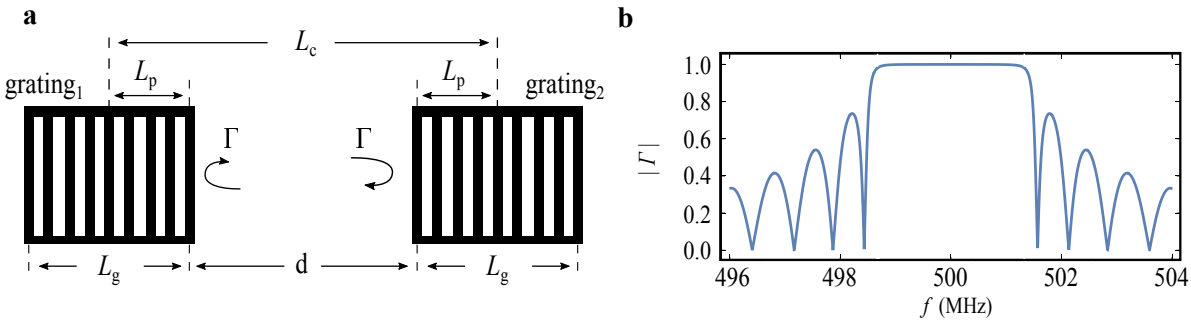

Figure 2.12 | Cavity and reflection coefficient of a grating. a, SAW cavity consisting of two shorted metallic gratings facing each other. **b,** Absolute value of the reflection coefficient Γ as a function of frequency for a grating with reflectivity $|r_s| = 0.9$ and $N_g = 600$ fingers.

Here, Y_0 is the admittance load (typically $Y_0 = 1/50\,[\Omega^{-1}]$). These expressions can be used to obtain the frequency response of a delay line by substituting equation (2.28) in equations (2.29)-(2.30) and taking into account that the modulus of Y_{12} is $|Y_{12}| = \sqrt{G_a^L(f)\,G_a^R(f)}$, where $G_a^L(f)$, $G_a^R(f)$ are the conductances of the left and right IDT respectively.

SAW cavities and SAW resonators

The interdigitated transducer is designed to excite and collect surface acoustic waves. In order to confine these travelling perturbations, a regular array of metallic strips (or shallow grooves etched inside the substrate) can be placed on the two sides of the IDT. This regular array is usually called grating[6]. As the SAW penetrates into a grating, its amplitude decreases. This phenomenon takes place because each metallic finger locally alters the speed of the travelling wave leading to a small reflection of the incoming wave. If the centres of adjacent fingers are separated by an half wavelength, individual reflected waves add up in phase and the overall reflection mechanism becomes significant. Note that the gratings only reflect incoming waves in a specific frequency band usually called stopband.

[6]In the following, we will always assume that the grating consists of *shorted* metallic strips.

A SAW cavity consists of two gratings facing each other and separated by a distance d (see Fig. 2.12a). The reflection coefficient Γ of a grating at the resonance frequency $f_0 = v/2p$ only depends on the number of fingers N_g and their reflectivity r_s:

$$|\Gamma(f_0)| = \tanh(|r_s| N_\mathrm{g})$$

where typical values are $|r_s| = 0.001 - 0.1$ and $N_\mathrm{g} = 500 - 1000$. The more general expression of the reflection coefficient as a function of frequency is given by:

$$\Gamma(f) = \frac{|r_s|}{p} \frac{\sin(sL_\mathrm{g})}{s\cos(sL_\mathrm{g}) + j\delta\sin(sL_\mathrm{g})},$$

where $\delta = 2\pi(f - f_0)/v$ is a detuning parameter, $s = \sqrt{\delta^2 - |r_s/p|^2}$ and L_g is the length of the grating. Figure 2.12b shows the reflection coefficient $|\Gamma(f)|$ for $|r_s| = 0.009$ and $N_\mathrm{g} = 600$. For highly reflective gratings, the first stopband is $\Delta f_\mathrm{1SB} \approx 2|r_s| f_0/\pi$ wide and the device can be considered transparent to waves with frequencies outside of this range.

SAW resonators can have different geometries and purposes. The simplest SAW resonator consists in a regular single-electrode IDT placed between two gratings. This device is usually called 1-port SAW resonator (see Fig. 2.13a). When an oscillating voltage is applied to the bus bars of the IDT, surface acoustic waves are generated in opposite directions. These waves eventually impinge against the gratings and bounce back. As the waves keep bouncing back and forth, standing waves settle inside the cavity.

A 1-port SAW resonator can work as a multimode device depending on the distance between the two gratings. This geometrical parameter is denoted by d^*, where the asterisk indicates that the reference points are situated in the middle of the first finger of the grating. In order to have constructive interference, the distance between

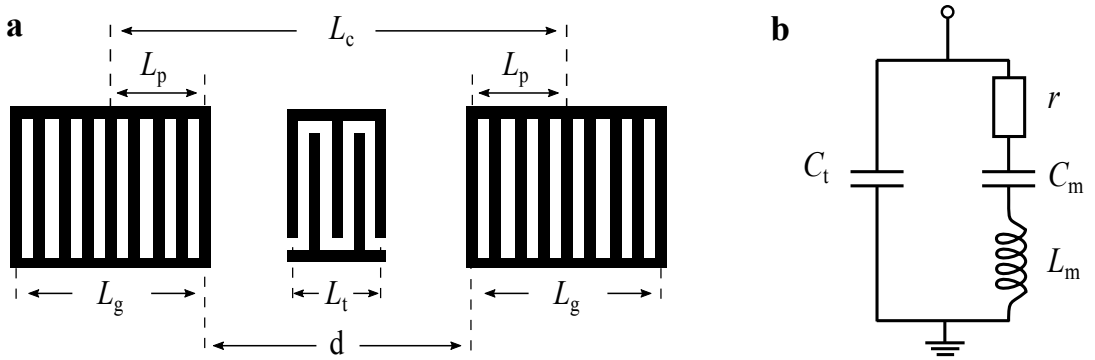

Figure 2.13 | SAW resonator and equivalent circuit. a, 1-port SAW resonator consisting of an IDT placed between two gratings. **b,** Equivalent circuit of a 1-port SAW resonator. It consists of two branches in parallel.

the two gratings must satisfy:

$$d^* = \left(2n - \frac{1}{2}\right)\frac{\lambda_0}{2}$$

where $n \in \mathbb{N}$. As regards the distance between the IDT and each grating d_s^*, its optimal value is given by [24]:

$$d_s^* = \left(\frac{n}{2} - \frac{1}{4}\right)\lambda_0 + \frac{\lambda_0}{8}.$$

The symmetric geometry of a 1-port SAWR implies that it can only sustain symmetric modes. The mode spacing (also called free spectral range FSR) of a 1-port SAWR is defined as:

$$FSR = \frac{v}{L_c},$$

where L_c is the length of the acoustic cavity. The cavity length L_c is slightly longer than d^*; more precisely, the cavity length is defined as:

$$L_c = d + 2L_p,$$

where L_p is the penetration depth, i.e. the distance travelled by the wave into the grating. If the number of fingers in the IDT is considerably high such that

$\tanh(|r_s| N_g) \approx 1$, then the penetration depth is related to the reflectivity of each finger in a simple way $L_p = \lambda_0/4\,|r_s|$. When the FSR is greater than the first stopband $FSR > \Delta f_{1SB}$, the device shows only one resonant mode. On the other hand, when $FSR > \Delta f_{1SB}$, multiple resonances are observed.

SAW resonators equivalent circuit

The electrical response of a 1-port SAW resonator can be modelled with an equivalent electrical circuit as shown in Fig. 2.13b. This circuit consists of two branches in parallel. The first branch comprises a capacitance C_t, which models the geometrical capacitance of the IDT [its value is given by equation (2.26)]. In the second branch, a resistance r, a capacitance C_m and an inductance L_m are present. The resistance models losses in the cavity, such as the finite grating reflectivity. The motional capacitance and inductance are due to the presence of acoustic waves inside the cavity. The analytical form of these variables is given by [62]:

$$\begin{aligned} C_t &= N_p W \varepsilon_\infty \\ r &= \frac{1 - |\Gamma(f)|}{2G_a(f)} \\ L_m &= \frac{L_c}{4vG_a(f)} \\ C_m &\approx 1.8 C_t \frac{L_t}{L_c}\frac{\Delta v}{v}, \end{aligned}$$

where $L_t = (2N_t - 1)\,\lambda_0/4$ is the length of the transducer. The admittance of the equivalent circuit is given by the sum of the admittances of the two branches:

$$Y_{1PR} = Y_{branch1} + Y_{branch2} = j2\pi f C_t + \frac{1}{r + j2\pi f L_m + \frac{1}{j2\pi f C_m}}.$$

By substituting this expression in equation (2.29) we find the expression of the reflection coefficient $S_{11}(f)$ as a function of frequency.

2.3 Circuit quantum electrodynamics

Circuit quantum electrodynamics (QED) deals with the interaction between light and matter on a chip. The original implementation included a Cooper pair box (CPB) coupled to a coplanar waveguide resonator (CPWR) measured in transmission [92]. In this architecture, the CPB served as qubit, whereas the CPWR was mainly adopted as readout component. In the field of superconducting devices, several qubits have been developed and coupled to resonant circuits. All of these qubits include a Josephson junction as non-linear component with the purpose of creating a non-harmonic effective potential. Superconducting qubits can be cataloged into three main flavours [22]: charge qubits, phase qubits and flux qubits. In this thesis, we have focused on charge qubits. As the name suggests, charge qubits are superconducting qubits in which the degree of freedom that is controlled is the electric charge. They were theoretically investigated for the first time by Büttiker [16] and experimentally implemented by the Saclay group [12]. The control of a CPB in the time domain was achieved for the first time by the NEC group in 1999 [64]. Unfortunately, Cooper pair boxes are very sensitive to charge noise and their coherence time is mainly limited by this loss channel. In 2007, the Yale group proposed a new variant of this qubit called the transmon [43], i.e. a Cooper pair box operating in a specific regime with the purpose of mitigating charge fluctuations on the superconducting island and improving its coherence time. Transmons are now widely used in the superconducting qubit community, mainly for their ease of fabrication and high performance.

In the following sections we present the theory of the CPB and the transmon. We will then study the coupling between a charge qubit and a resonator.

The Cooper pair box

A CPB consists of a macroscopic superconducting island connected to a superconducting electron reservoir via a Josephson junction with geometric capacitance C_{J}. The superconducting island can be capacitively coupled to an external voltage source by a gate capacitance C_{g} (see Fig. 2.14). By varying the value of the gate voltage V_{g} is possible to transfer Cooper pairs from the reservoir to the island and vice-versa. In the following, we assume that the two superconducting electrodes have an energy gap well above the thermal fluctuations. In addition, we assume that the energy required to add a Cooper pair to the island is much larger than the thermal energy of the surroundings.

The quantum ground state of the electrons on the island exists in a low energy state in which all the electrons form Cooper pairs. Similarly, the ground state of the reservoir consists of all electrons that are fully paired up. The global system can then be described by the state $|n_{\mathrm{R}}, n_{\mathrm{I}}\rangle$ where n_{R} indicates the number of Cooper pairs in the reservoir and n_{I} is the number of pairs in the superconducting island. The total number of pairs in the two electrodes is fixed: $n_{\mathrm{R}} + n_{\mathrm{I}} = \text{const}$. Nevertheless, a single Cooper pair can tunnel through the junction, reducing n_{R} and increasing n_{I} and viceversa. Therefore, we can describe the state of the CPB with a more convenient notation: we identify the state of the system with the number of Cooper pairs $\mathbf{n}$ in excess or deficit on the superconducting island with respect to the equilibrium configuration:

$$|\mathbf{n}\rangle = |n_{\mathrm{R}} - \mathbf{n}, n_{\mathrm{I}} + \mathbf{n}\rangle \qquad \mathbf{n} \in \mathbb{Z}. \tag{2.31}$$

When the gate voltage is set to zero, the system is in its equilibrium state $|\mathbf{0}\rangle = |n_{\mathrm{R}}, n_{\mathrm{I}}\rangle$. If the gate voltage is increased by a small amount V_{g}, a continuous charge $Q_{\mathrm{g}} = C_{\mathrm{g}} V_{\mathrm{g}}$ will be induced on the island. In order for the island to stay neutral, single

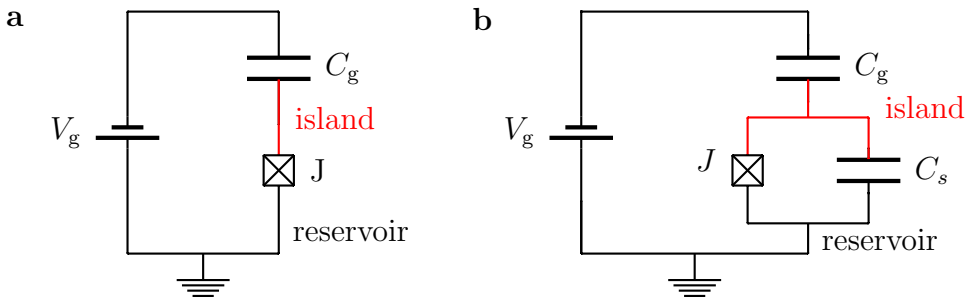

Figure 2.14 | Equivalent circuit of a Cooper Pair Box a, The superconducting island (red) is coupled to a voltage source via a gate capacitance C_g. **b,** The same circuit with a shunt capacitance C_s in parallel to the Josephson junction.

Cooper pairs will tunnel from the reservoir to the island. If the charge induced on the island is exactly $Q_g = 2e$, then the state $|\mathbf{0}\rangle$ becomes less energetically favourable and a Cooper pair hops through the junction bringing the system to the state $|\mathbf{1}\rangle$. However, when the charge induced on the island is half that of a Cooper pair $Q_g = e$, both two states $|\mathbf{0}\rangle$ and $|\mathbf{1}\rangle$ are energetically favourable and the system is found in a superposition state. Therefore, by varying the gate voltage, it is possible to coherently control the number state $|\mathbf{n}\rangle$. With simple arguments, it can be shown that the average number of Cooper pairs on the island $\langle\hat{\mathbf{n}}\rangle$ depends on the gate voltage V_g in the following way [12]:

$$\langle\hat{\mathbf{n}}\rangle = \lfloor n_g \rfloor + \frac{1}{2}\left[\frac{a\tanh\left(b\sqrt{1+a^2}\right)}{\sqrt{1+a^2}}\right], \tag{2.32}$$

where[7] $a = E_C\left(2n_g - 1 - 2\lfloor n_g \rfloor\right)/E_J$, $b = E_J/\left(2k_BT\right)$ and $n_g = C_gV_g/2e$. This function is shown in Fig. 2.15 for $T = 10\,\mathrm{mK}$ and $E_C = 10E_J$ in terms of the offset charge $n_g = C_gV_g/2e$. Here, E_J is the energy required to move one Cooper pair through the junction. Without going into the details of its derivation, we now present

[7]The function $\lfloor x \rfloor$ denotes the floor of x.

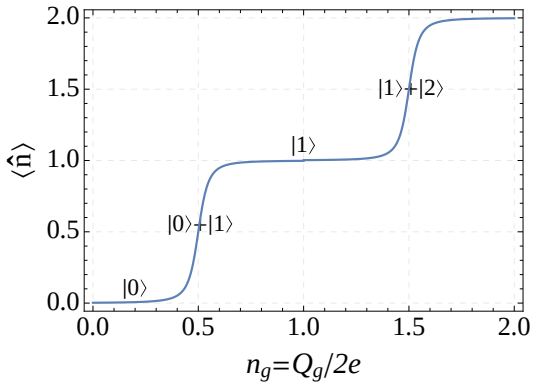

Figure 2.15 | Plot of equation 2.32 with $E_{\mathrm{J}} = 0.1E_{\mathrm{C}}$. The average number of Cooper pairs on the island $\langle \hat{\mathbf{n}} \rangle$ depends on the offset charge n_{g}. When $n_{\mathrm{g}} = 0.5$, the CPB state is in a superposition state $|\mathbf{0}\rangle + |\mathbf{1}\rangle$.

the Hamiltonian of the CPB shunted by a capacitance[8] C_{s} as shown in Fig. 2.14b:

$$\hat{\mathcal{H}}_{\mathrm{CPB}} = 4E_{\mathrm{C}} \left(\hat{\mathbf{n}} - n_{\mathrm{g}}\right)^2 - E_{\mathrm{J}} \cos \hat{\phi}. \tag{2.33}$$

Here, we expressed the charge on the island $\hat{Q}$ in terms of the number of Cooper pairs $\hat{Q} = 2e\hat{\mathbf{n}}$ and introduced the phase difference $\hat{\phi}$ between the two macroscopic wavefunctions on the two sides of the island. We defined the Coulomb charging energy as $E_{\mathrm{C}} = e^2/2C$, where $C = C_{\mathrm{s}} + C_{\mathrm{J}} + C_{\mathrm{g}}$. The quantity E_{C} indicates the amount of energy required to transfer a single electron to the island and it can be engineered by varying the shunt capacitance C_{s}. Note that the CPB operates in the regime $E_{\mathrm{C}} > E_{\mathrm{J}}$, the so called charge regime.

The eigenvalues and eigenstates of the CPB Hamiltonian are defined by:

$$\hat{\mathcal{H}}_{\mathrm{CPB}} |k\rangle = E_k |k\rangle. \tag{2.34}$$

In the phase basis, the number operator can be expressed as $\hat{\mathbf{n}} = -i\partial/\partial\phi$ and the eigenevalue equation (2.34) in the phase basis takes the form:

$$4E_{\mathrm{C}} \left(-i\frac{\partial}{\partial \hat{\phi}} - n_{\mathrm{g}}\right)^2 \psi_k(\phi) - E_J \cos \hat{\phi} \psi_k(\phi) = E_k \psi_k(\phi). \tag{2.35}$$

[8]The presence of a shunt capacitance does not significantly affect the calculations and will become useful when we introduce the transmon later on in this chapter.

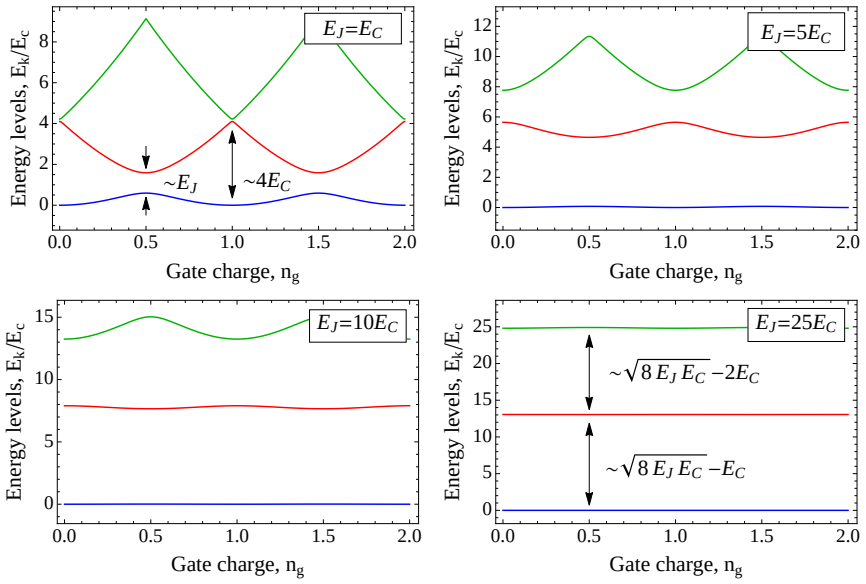

Figure 2.16 | Energy levels of a CPB for four different values of E_J/E_C. For low values of E_J/E_C, the energies are parabolic functions of the offset charge n_g. Avoided crossings are visible when $n_g = \pm l/2$ where l is odd. As the ratio is increased the eigenenergies become exponentially flatter.

The solution of this differential equation can be written in terms of Mathieu functions[9]. The eigenenergies and eigenfunctions are [23]:

$$E_k(n_g) = 4E_C \mathcal{M}_A \left[k+1-(k+1) \mod 2 + 2n_g\,(-1)^k, -\frac{E_J}{2E_C} \right] \tag{2.39}$$

$$\psi_k(\phi) = \frac{e^{in_g\phi}}{2\pi} \left[\mathcal{M}_C \left[\frac{E_k}{E_C}, \frac{-E_j}{2E_C}, \frac{\phi}{2} \right] + i\,(-1)^{k+1}\,\mathcal{M}_S \left[\frac{E_k}{E_C}, \frac{-E_j}{2E_C}, \frac{\phi}{2} \right] \right] \tag{2.40}$$

Equation (2.39) is the analytical form of the eigenenergies of the CPB, where k labels all the different levels. As shown in Fig. 2.16, the dispersion relation $E_k(n_g)$ depends strongly on the ratio E_J/E_C.

We can also write the Hamiltonian of the CPB in the charge representation:

$$\hat{\mathcal{H}}_{CPB} = \sum_{\mathbf{n}\in\mathbb{Z}} 4E_C\,(\mathbf{n}-n_g)^2\,|\mathbf{n}\rangle\langle\mathbf{n}| - \frac{E_J}{2}\sum_{\mathbf{n}\in\mathbb{Z}} \left[|\mathbf{n}+1\rangle\langle\mathbf{n}| + |\mathbf{n}\rangle\langle\mathbf{n}+1|\right] \tag{2.41}$$

[9]The Mathieu functions are implemented in Mathematica in the following way:

$$\mathcal{M}_A(r,q) = \text{MathieuCharacteristicA}[r,q] \tag{2.36}$$

$$\mathcal{M}_C(a,q,z) = \text{MathieuC}[a,q,z] \tag{2.37}$$

$$\mathcal{M}_S(a,q,z) = \text{MathieuS}[a,q,z] \tag{2.38}$$

It is possible to find the eigenstates and eigenvalues of this Hamiltonian by truncating the summation at some large values of $|\mathbf{n}|$ and numerically diagonalising its corresponding matrix. The result will be similar to the exact functional form equation (2.39).

In the charge regime $E_{\mathrm{C}} \gtrsim E_{\mathrm{J}}$ and when $n_{\mathrm{g}} = 1/2$, the ground state $|g\rangle$ and the first excited state $|e\rangle$ are given by a symmetric and antisymmetric superposition of the charge states $|\mathbf{0}\rangle$ and $|\mathbf{1}\rangle$ and the corresponding eigenenergies are separated by an energy E_{J} (see Fig. 2.16). Since the spectrum of the CPB is highly anharmonic, it is possible to individually address the first two eigenstates $|g\rangle$, $|e\rangle$ without exciting higher energy levels. Therefore, the Hamiltonian of the CPB can be reduced to the space spanned by the ground and first excited state and can be effectively used as a qubit.

We now derive the Hamiltonian of the CPB at the degeneracy point[10] $n_{\mathrm{g}} = 1/2$ in the charge regime $E_{\mathrm{C}} \gtrsim E_{\mathrm{J}}$. In this regime, the eigenstates $|k\rangle$ of the CPB Hamiltonian are closely related to the charge states $|\mathbf{n}\rangle$ [91]. Since the system is sufficiently anharmonic, we can restrict ourselves to the two lowest energy states. If we perform a Taylor expansion of the first term in equation (2.41) close to $n_{\mathrm{g}} = 1/2$, we obtain:

$$f\left(n_{\mathrm{g}}\right) = \left(\hat{\mathbf{n}} - n_{\mathrm{g}}\right)^2 \approx f\left(\frac{1}{2}\right) + f'\left(\frac{1}{2}\right)\left(n_{\mathrm{g}} - 1/2\right) = \hat{\mathbf{n}} - \frac{1}{4} + n_{\mathrm{g}} - 2\hat{\mathbf{n}} n_{\mathrm{g}}, \tag{2.42}$$

and the Hamiltonian can be written as:

$$\hat{\mathcal{H}}_{\mathrm{CPB}} = 4E_{\mathrm{C}}\left[\left(-\frac{1}{4} + n_g\right)|\mathbf{0}\rangle\langle\mathbf{0}| + \left(\frac{3}{4} - n_{\mathrm{g}}\right)|\mathbf{1}\rangle\langle\mathbf{1}|\right] - \frac{E_{\mathrm{J}}}{2}\left[|\mathbf{1}\rangle\langle\mathbf{0}| + |\mathbf{0}\rangle\langle\mathbf{1}|\right]. \tag{2.43}$$

[10] This operating point is sometimes called "sweet spot" because it is insensitive to charge noise to first order.

Writing the operators $|\mathbf{0}\rangle\langle\mathbf{0}|$, $|\mathbf{1}\rangle\langle\mathbf{1}|$ in terms of the Pauli matrices, we finally obtain[11]:

$$\begin{aligned}\hat{\mathcal{H}}_{\mathrm{CPB}} &= E_{\mathrm{C}}\, I + 2E_{\mathrm{C}}\,(2n_{\mathrm{g}} - 1)\,\hat{\sigma}_z - \frac{E_{\mathrm{J}}}{2}\hat{\sigma}_x = \\ &= -\frac{1}{2}\left(\epsilon\hat{\sigma}_z + E_{\mathrm{J}}\hat{\sigma}_x\right) = -\frac{1}{2}\begin{pmatrix} \epsilon & E_{\mathrm{J}} \\ E_{\mathrm{J}} & -\epsilon \end{pmatrix},\end{aligned} \tag{2.44}$$

where the constant term $E_{\mathrm{C}}I$ was dropped and $\epsilon = 4E_{\mathrm{C}}\,(1 - 2n_{\mathrm{g}})$. This is the Hamiltonian of the CPB in the laboratory frame at the degeneracy point.

It is possible to diagonalise the Hamiltonian of the CPB and find its eigenstates:

$$|g\rangle = \cos\frac{\theta}{2}|\mathbf{0}\rangle + \sin\frac{\theta}{2}|\mathbf{1}\rangle \tag{2.45}$$

$$|e\rangle = -\sin\frac{\theta}{2}|\mathbf{0}\rangle + \cos\frac{\theta}{2}|\mathbf{1}\rangle, \tag{2.46}$$

and eigenvalues:

$$E_{g,e} = \mp\frac{1}{2}\sqrt{\epsilon^2 + E_{\mathrm{J}}^2}, \tag{2.47}$$

where $\theta = \arctan E_{\mathrm{J}}/\epsilon$ is usually called mixing angle. The basis $\{|g\rangle, |e\rangle\}$ is the actual computational basis used to perform quantum algorithms.

The transmon

The main parameters characterising the energy levels of a CPB are the charge dispersion ϵ_k and the anharmonicity α. The charge dispersion ϵ_k describes the dependence of the energy spectrum with respect to the effective offset charge n_g and it is defined as follows:

$$\epsilon_k = E_k(n_{\mathrm{g}} = 1/2) - E_k(n_{\mathrm{g}} = 0),$$

where E_k is the eigenenergy of the CPB [equation (2.39)]. Note that n_{g} is a continuous variable that is determined by the gate voltage or any other electrode or surface charge randomly coupled to the superconducting island. The value of n_{g} is subject to noise

[11] Recall that $|\mathbf{0}\rangle\langle\mathbf{0}| = (1 + \hat{\sigma}_z)/2$, $|\mathbf{1}\rangle\langle\mathbf{1}| = (1 - \hat{\sigma}_z)/2$ and $|\mathbf{1}\rangle\langle\mathbf{0}| + |\mathbf{0}\rangle\langle\mathbf{1}| = \hat{\sigma}_x$.

fluctuations and this phenomenon significantly limits the dephasing time of the qubit. The second parameter, the anharmonicity, is defined as the difference between the first two adjacent transition energies and its absolute and relative values are given by

$$\alpha = E_{12} - E_{01} \qquad \alpha_{\mathrm{r}} = \frac{E_{12} - E_{01}}{E_{01}}, \tag{2.48}$$

where $E_{kj} = E_j - E_k$. Ideally, it would be desirable to have a charge dispersion that weakly depends on the offset charge n_{g} such that random fluctuations do not significantly change the transition energy of the qubit. In addition, the anharmonicity should be sufficiently high in order to be able to selectively address each energy level. Unfortunately, the charge dispersion of the CPB strongly depends on n_{g}. However, in the phase regime $E_{\mathrm{J}} \gg E_{\mathrm{C}}$, the charge dispersion ϵ_k weakly depends on n_{g} (see Fig. 2.16). In a seminal paper, the Yale group showed that in this regime the charge dispersion exponentially decreases, whereas the relative anharmonicity is only affected by a weak power law [43] leading to a significant improvement of the coherence time of this superconducting qubit. A CPB working in the phase regime $E_{\mathrm{J}} \gg E_{\mathrm{C}}$ is called a transmon. The transmon and the CPB share the same equivalent circuit and the phase regime can be obtained by engineering the value of the shunt capacitance C_{s} in parallel with the Josephson junction.

The Hamiltonian of a transmon is the same as the one of a Cooper pair box equation (2.33). Since $E_{\mathrm{J}} \gg E_{\mathrm{C}}$, the phase ϕ only performs small oscillations around its equilibrium point [43], and the cosine term in equation (2.33) can be Taylor expanded leading to the Hamiltonian of the transmon:

$$\hat{\mathcal{H}}_{\mathrm{tr}} = 4E_{\mathrm{C}}\hat{n}^2 + \frac{1}{2}E_{\mathrm{J}}\hat{\phi}^2 - \frac{E_{\mathrm{J}}}{24}\hat{\phi}^4 - E_{\mathrm{J}}. \tag{2.49}$$

Here, we have kept only quadratic terms in the expansion. This is the Hamiltonian of a quantum harmonic oscillator with a quartic perturbation, also known as Duffing

oscillator. Introducing the usual creation and annihilation operators:

$$\hat{n} = -\frac{i}{\sqrt{2}}\left(\frac{E_\mathrm{J}}{8E_\mathrm{C}}\right)^{1/4}\left(\hat{b}-\hat{b}^\dagger\right) \qquad\qquad \hat{\phi} = \frac{1}{\sqrt{2}}\left(\frac{8E_\mathrm{C}}{E_\mathrm{J}}\right)^{1/4}\left(\hat{b}+\hat{b}^\dagger\right), \tag{2.50}$$

where $\left[\hat{\phi},\hat{n}\right] = i$ and dropping the constant term $-E_\mathrm{J}$, the Hamiltonian of the transmon becomes:

$$\hat{\mathcal{H}}_\mathrm{tr} = \sqrt{8E_\mathrm{C}E_\mathrm{J}}\left(\hat{b}^\dagger\hat{b}+\frac{1}{2}\right) - \frac{E_\mathrm{C}}{12}\left(\hat{b}+\hat{b}^\dagger\right)^4 = \hat{\mathcal{H}}_0 + \hat{\mathcal{H}}_\mathrm{pert}, \tag{2.51}$$

where the first term is the unperturbed Hamiltonian $\hat{\mathcal{H}}_0$ and the second one is the quartic perturbation. The spectrum consists of discrete energy levels and the energy separation between the ground state and the first excited is $E_{01} = \sqrt{8E_\mathrm{C}E_J} - E_\mathrm{C}$. The first two levels identify the two level system used as a qubit. We can now derive the eigenergies of the transmon Hamiltonian. Defining the qubit transition angular frequency as $\omega_\mathrm{q} = \sqrt{8E_\mathrm{C}E_\mathrm{J}}/\hbar$, the unperturbed Hamiltonian becomes $\hat{\mathcal{H}}_0 = \hbar\omega_\mathrm{q}\left(\hat{b}^\dagger\hat{b}+1/2\right)$ and its eigenstates $|j^{(0)}\rangle$ are that of a quantum harmonic oscillator: $\hat{\mathcal{H}}_0|j^{(0)}\rangle = E_j^{(0)}|j^{(0)}\rangle$. When calculating first order perturbative contributions to the energy levels, only diagonal matrix elements need to be considered. After some calculations and considering only the terms of the form $\left(\hat{b}^\dagger\hat{b}\right)^i$ where $i \in \mathbb{N}$, we obtain:

$$\hat{\mathcal{H}}_\mathrm{pert} = -\frac{E_\mathrm{C}}{12}\left(\hat{b}+\hat{b}^\dagger\right)^4 \approx -\frac{E_\mathrm{C}}{12}\left(6\hat{b}^\dagger\hat{b}\hat{b}^\dagger\hat{b}+6\hat{b}^\dagger\hat{b}+3\right). \tag{2.52}$$

Evaluating the expectation value $\langle j|\hat{\mathcal{H}}_\mathrm{pert}|j\rangle$, we conclude that the transmon energy levels are affected by the quartic perturbation in the following way:

$$E_j = \hbar\omega_\mathrm{q}\left(j+\frac{1}{2}\right) - \frac{E_\mathrm{C}}{12}\left(6j^2+6j+3\right). \tag{2.53}$$

Furthermore, the anharmonicity is different from the one of the CPB and its asymptotic value for $E_\mathrm{J} \gg E_\mathrm{C}$ is:

$$\alpha \simeq -E_\mathrm{C} \qquad \alpha_\mathrm{r} \simeq -\left(\frac{8E_\mathrm{J}}{E_\mathrm{C}}\right)^{1/2}. \tag{2.54}$$

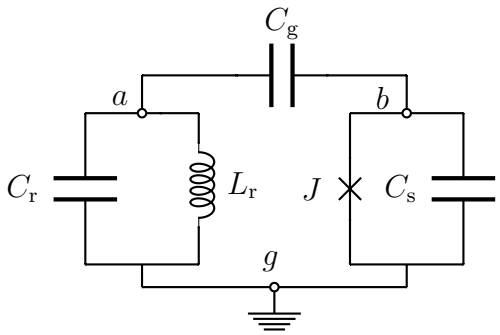

Figure 2.17 | Equivalent circuit of a Cooper pair box capacitively coupled to an LC resonator.

This equation clearly shows that in the phase regime the relative anharmonicity only decreases with a weak power law and approaches zero very slowly for large values of $E_\mathrm{J}/E_\mathrm{C}$. Thus, the potential energy of the transmon is still sufficiently anharmonic and this system can be used as a qubit.

Coupling between a charge qubit and a resonator

In this section we consider the capacitive coupling between a CPB and a resonator. The calculations regarding the coupling between a transmon and a resonator are a bit more complicated, but lead to the same conclusions. Figure 2.17 shows the equivalent circuit of the system under investigation: a CPB is connected to an LC resonator via a coupling capacitance C_g. Experimentally, the CPB is placed in an antinode of a high quality factor resonator such as a coplanar waveguide resonator or a 3D cavity. It can be shown that the Hamiltonian of this coupled system reads:

$$\hat{\mathcal{H}}_\mathrm{r} + \hat{\mathcal{H}}_\mathrm{CPB} = \hbar\omega_\mathrm{r}\left(\hat{a}^\dagger\hat{a} + \frac{1}{2}\right) + 4E_\mathrm{C}\left(\hat{\mathbf{n}} - \frac{C_\mathrm{g}\hat{V}}{2e}\right)^2 - E_\mathrm{J}\cos\hat{\phi}, \tag{2.55}$$

where $\omega_\mathrm{r}/2\pi$ is the frequency of the cavity and $\hat{V}$ is the potential difference across the capacitance of the LC resonator

$$\hat{V} = \frac{\hat{Q}}{C_\mathrm{r}} = \sqrt{\frac{\hbar\omega_\mathrm{r}}{2C_\mathrm{r}}}\left(\hat{a} + \hat{a}^\dagger\right). \tag{2.56}$$

Substituting equation (2.56) into (2.55) and neglecting a quadratic term that does not depend on $\hat{\mathbf{n}}$, we obtain

$$\hat{\mathcal{H}}_{\mathrm{r}} + \hat{\mathcal{H}}_{\mathrm{q}} + \hat{\mathcal{H}}_{\mathrm{g}} = \hbar\omega_{\mathrm{r}} \left(\hat{a}\hat{a}^{\dagger} + \frac{1}{2} \right) + 4E_{\mathrm{C}}\hat{\mathbf{n}}^2 - E_{\mathrm{J}} \cos\hat{\phi} - 2\beta \sqrt{\frac{\hbar\omega_{\mathrm{r}}}{2C_{\mathrm{r}}}} \left(\hat{a} + \hat{a}^{\dagger} \right), \hat{\mathbf{n}} \quad (2.57)$$

where $\beta = C_{\mathrm{g}}/C$. Restricting ourselves to the first two energy levels of the CPB, we find

$$\hat{\mathcal{H}}_{\mathrm{r}} + \hat{\mathcal{H}}_{\mathrm{q}} + \hat{\mathcal{H}}_{\mathrm{g}} = \hbar\omega_{\mathrm{r}} \left(\hat{a}\hat{a}^{\dagger} + \frac{1}{2} \right) - \frac{1}{2} \left(\epsilon\hat{\sigma}_z + E_J\hat{\sigma}_x \right) - 2e\beta \sqrt{\frac{\hbar\omega_{\mathrm{r}}}{2C_{\mathrm{r}}}} \left(\hat{a} + \hat{a}^{\dagger} \right) \hat{\mathbf{n}}. \quad (2.58)$$

Since $\hat{\mathbf{n}} = (1 - \hat{\sigma}_z)/2$, the qubit and coupling Hamiltonian become:

$$\hat{\mathcal{H}}_{\mathrm{q}} + \hat{\mathcal{H}}_{g} = -\frac{1}{2} \left(\epsilon\hat{\sigma}_z + E_J\hat{\sigma}_x \right) + e\beta \sqrt{\frac{\hbar\omega_{\mathrm{r}}}{2C_{\mathrm{r}}}} \left(\hat{a} + \hat{a}^{\dagger} \right) \hat{\sigma}_z,$$

where we have dropped a constant term. If we now go from the lab frame to the qubit frame[12], we obtain:

$$\begin{aligned} \hat{\mathcal{H}}_{\mathrm{q}} + \hat{\mathcal{H}}_{g} &= \frac{\hbar\omega_{\mathrm{q}}}{2}\hat{\sigma}_{z'} + e\beta \sqrt{\frac{\hbar\omega_{\mathrm{r}}}{2C_{\mathrm{r}}}} \left(\hat{a} + \hat{a}^{\dagger} \right) \left(\sin\theta\hat{\sigma}_{x'} + \cos\theta\hat{\sigma}_{z'} \right) = \\ &= \frac{\hbar\omega_{\mathrm{q}}}{2}\hat{\sigma}_{z'} + e\beta \sqrt{\frac{\hbar\omega_{\mathrm{r}}}{2C_{\mathrm{r}}}} \left(\hat{a} + \hat{a}^{\dagger} \right) \hat{\sigma}_{x'}, \end{aligned}$$

where we made the approximation $\sin\theta \sim 1$, $\cos\theta \sim 0$ since we are assuming to be operating close to the degeneracy point $n_{\mathrm{g}} = 1/2$. Finally, we can write the Pauli matrix $\hat{\sigma}_x$ in terms of the lowering and raising operators $\hat{\sigma}^{+} = |e\rangle\langle g|$ and $\hat{\sigma}^{-} = |g\rangle\langle e|$ and obtain:

$$\hat{\mathcal{H}}_{\mathrm{JC}} = \hbar\omega_{\mathrm{r}} \left(\hat{a}^{\dagger}\hat{a} + \frac{1}{2} \right) + \frac{\hbar\omega_{\mathrm{q}}}{2}\hat{\sigma}_z + \hbar g \left(\hat{a} + \hat{a}^{\dagger} \right) \left(\hat{\sigma}^{+} + \hat{\sigma}^{-} \right), \quad (2.60)$$

[12] This transformation can be done by performing the following transformation:

$$\begin{pmatrix} \hat{\sigma}_x \\ \hat{\sigma}_y \\ \hat{\sigma}_z \end{pmatrix} = \begin{pmatrix} \cos\theta & 0 & -\sin\theta \\ 0 & 1 & 0 \\ \sin\theta & 0 & \cos\theta \end{pmatrix} \begin{pmatrix} \hat{\sigma}_{x'} \\ \hat{\sigma}_{y'} \\ \hat{\sigma}_{z'} \end{pmatrix} = \begin{pmatrix} \cos\theta\hat{\sigma}_{x'} - \sin\theta\hat{\sigma}_{z'} \\ \hat{\sigma}_{y'} \\ \sin\theta\hat{\sigma}_{x'} + \cos\theta\hat{\sigma}_{z'} \end{pmatrix}. \quad (2.59)$$

where we have defined the coupling strength g as $\hbar g = e\beta\sqrt{\hbar\omega_{\mathrm{r}}/2C_{\mathrm{r}}}$ and have dropped the primes on the Pauli matrices for convenience. The coupling strength g has unit of an angular frequency and its value indicates the rate at which the cavity and the qubit exchange a quantum of energy. Typical values of g are in the range $g/2\pi = 10 - 100\,\mathrm{MHz}$. The Hamiltonian equation (2.60) is called the Jaynes-Cummings Hamiltonian. It is divided into two parts: the first one ($\hat{\mathcal{H}}_0 = \hat{\mathcal{H}}_{\mathrm{r}} + \hat{\mathcal{H}}_{\mathrm{q}}$) is related to the cavity and qubit energy. The second term ($\hat{\mathcal{H}}_g$) is the coupling Hamiltonian, which is responsible for the dynamics of the coupled system. Performing the rotating wave approximation (i.e. neglecting contributions oscillating at high frequency), the terms $\hat{a}\hat{\sigma}$, $\hat{a}^\dagger\hat{\sigma}^+$ can be dropped[13] and the Jaynes-Cummings Hamiltonian finally becomes:

$$\hat{\mathcal{H}}_{\mathrm{JC}} = \hbar\omega_{\mathrm{r}}\left(\hat{a}^\dagger\hat{a} + \frac{1}{2}\right) + \frac{\hbar\omega_{\mathrm{q}}}{2}\hat{\sigma}_z + \hbar g\left(\hat{a}\hat{\sigma}^+ + \hat{a}^\dagger\hat{\sigma}^-\right). \tag{2.62}$$

The energy conserving term $\hat{a}\hat{\sigma}^+$ describes the process where a photon is annihilated and the artificial atom is excited from the ground state $|0\rangle$ to the first excited state $|1\rangle$. The other term $\hat{a}^\dagger\hat{\sigma}^-$ describes the opposite phenomenon (de-excitation of the artificial atom and creation of a photon inside the cavity). We can now derive the eigenstates and eigenenergies of this Hamiltonian. The two terms $\hat{a}\hat{\sigma}^+$, $\hat{a}^\dagger\hat{\sigma}^-$ only couple states that differ by one quantum of energy, $|e,n\rangle \leftrightarrow |g,n+1\rangle$ and they form a subspace Λ_n. In this subspace, the JC Hamiltonian can be written in the following

[13]The RWA can be better appreciated in the interaction picture. The Jaynes-Cummings Hamiltonian in this picture is obtained by performing the following transformation:

$$\hat{\mathcal{H}}_g^{\mathrm{int}} = S_0^{-1}\hat{\mathcal{H}}_g S_0 = \hbar g\left[\hat{\sigma}^+\hat{a}e^{i(\omega_{\mathrm{q}}-\omega_{\mathrm{r}})t} + \hat{\sigma}^+\hat{a}^\dagger e^{i(\omega_{\mathrm{q}}+\omega_{\mathrm{r}})t} + \hat{\sigma}^-\hat{a}e^{-i(\omega_{\mathrm{q}}+\omega_{\mathrm{r}})t} + \hat{\sigma}^-\hat{a}^\dagger e^{-i(\omega_{\mathrm{q}}-\omega_{\mathrm{r}})t}\right], \tag{2.61}$$

where $S_0(t) = \exp\frac{1}{i\hbar}\left[\frac{\hbar\omega_{\mathrm{q}}}{2}\hat{\sigma}_z + \hbar\omega_{\mathrm{r}}\left(\hat{a}^\dagger\hat{a} + \frac{1}{2}\right)\right]t$. When the frequency of the resonator is similar to the qubit transition frequency $\omega_{\mathrm{r}} \sim \omega_{\mathrm{q}}$, the terms $\hat{\sigma}a$, $\hat{\sigma}^+\hat{a}^\dagger$ rotate with angular frequency $\omega_{\mathrm{q}} + \omega_{\mathrm{r}}$, which is much higher than $\omega_{\mathrm{q}} - \omega_{\mathrm{r}}$. When calculating the transition amplitudes between two different energy states, these two terms will give small contributions and hence they can be neglected.

matrix form:

$$\begin{aligned}\hat{\mathcal{H}}_{\mathrm{JC}}^{\Lambda_n} &= \begin{pmatrix} \langle e,n|\hat{\mathcal{H}}_{\mathrm{JC}}|e,n\rangle & \langle e,n|\hat{\mathcal{H}}_{\mathrm{JC}}|g,n+1\rangle \\ \langle g,n+1|\hat{\mathcal{H}}_{\mathrm{JC}}|e,n\rangle & \langle g,n+1|\hat{\mathcal{H}}_{\mathrm{JC}}|g,n+1\rangle \end{pmatrix} = \\ &= \begin{pmatrix} \hbar\omega_{\mathrm{r}}\left(n+1\right)+\frac{\hbar\Delta}{2} & \hbar\frac{\Omega_n}{2} \\ \hbar\frac{\Omega_n}{2} & \hbar\omega_{\mathrm{r}}\left(n+1\right)+\frac{\hbar\Delta}{2} \end{pmatrix}, \end{aligned} \tag{2.63}$$

where we have defined the Rabi frequency $\Omega_n = 2g\sqrt{n+1}$ and the detuning $\Delta = \omega_{\mathrm{q}} - \omega_{\mathrm{r}}$. The diagonalisation of this symmetric matrix leads to the eigenenergies and eigenstates of the coupled system:

$$E_{\pm,n} = \hbar\omega_{\mathrm{r}}\left(n+1\right) \pm \hbar\frac{R}{2} \tag{2.64}$$

$$|+,n\rangle = \sin\theta_n|g,n+1\rangle + \cos\theta_n|e,n\rangle \tag{2.65}$$

$$|-,n\rangle = \cos\theta_n|g,n+1\rangle - \sin\theta_n|e,n\rangle, \tag{2.66}$$

where we have defined the generalised Rabi frequency $R\left(\Delta,\Omega_n\right) = \sqrt{\Delta^2+\Omega_n^2}$ and introduced the trigonometric functions:

$$\sin\theta_n = \frac{\Omega_n}{\sqrt{\left(R-\Delta\right)^2+\Omega_n^2}} \qquad \cos\theta_n = \frac{\left(R-\Delta\right)}{\sqrt{\left(R-\Delta\right)^2+\Omega_n^2}}. \tag{2.67}$$

The eigenstates $|+,n\rangle$ and $|-,n\rangle$ are called dressed states and they are maximally entangled states when $\cos\theta_n = \sin\theta_n$.

Dispersive regime and readout

When a superconducting qubit is dispersively coupled to an electromagnetic (or acoustic) cavity, the cavity frequency is dependent on the state of the qubit. This dispersive interaction gives the possibility to readout the state of the qubit by monitoring the frequency of the resonator. This is the most common readout scheme employed nowadays in the field of superconducting devices. Typically, the detuning $\Delta = |f_{01} - f_{\mathrm{r}}|$ between the qubit and the resonator is significantly bigger than the

coupling strength $\Delta \gg g$; this is the so-called dispersive limit. In this limit, the coupling term in the JC Hamiltonian can be treated as a small perturbation. In the interaction picture, $\hat{\mathcal{H}}_g$ takes the form:

$$\hat{\tilde{\mathcal{H}}}_g = \hat{S}_0^{-1} \hat{\mathcal{H}}_g \hat{S}_0, \tag{2.68}$$

where $\hat{S}_0 = \exp \frac{1}{i\hbar} \hat{\mathcal{H}}_0 t$ and $\hat{\mathcal{H}}_0 = h f_{01} \hat{\sigma}_z/2 + h f_\mathrm{r} \hat{a}^\dagger \hat{a}$. The analytical expression of the coupling term in the dispersive limit can be found with perturbation theory, though the calculations are a bit lengthy (see for example appendix A of reference [30]). The same result can be obtained by applying the Schrieffer-Wolff unitary transformation:

$$\hat{\mathcal{H}}_\mathrm{JC,disp} = \hat{U} \hat{\mathcal{H}}_\mathrm{JC} \hat{U}^{-1} = \frac{h\left(f_{01} + \chi\right)}{2} \hat{\sigma}_z + h\left(f_\mathrm{r} + \chi \hat{\sigma}_z\right) \hat{a}^\dagger \hat{a} \tag{2.69}$$

where $\hat{U} = \exp[g(\hat{a}\hat{\sigma}^+ - \hat{a}^\dagger \hat{\sigma}^-)/\Delta]$ and $\chi = -\frac{g^2}{\Delta}$ is the effective dispersive shift. The second term in equation (2.69) suggests that in the dispersive limit the cavity frequency depends on the qubit state. This feature provides the possibility to read out the qubit state by measuring the cavity frequency. This readout scheme was implemented for the first time in 2004 [92] and it is now ubiquitous in the field of superconducting devices.

Equation (2.69) can also be rearranged in the following form:

$$\hat{\mathcal{H}}_\mathrm{JC,disp} = h f_\mathrm{r} \hat{a}^\dagger \hat{a} + \frac{h}{2}\left(f_{01} + \chi + 2\chi \hat{a}^\dagger \hat{a}\right) \hat{\sigma}_z. \tag{2.70}$$

The second term in equation (2.70) expresses the AC Stark shift, i.e. a linear dependence of the qubit frequency from the number of photons populating the cavity. If the qubit linewidth γ is smaller than the effective dispersive shift χ, then it is possible to resolve the number of photons populating the cavity from qubit spectroscopy (see section 5.3 for an experimental evidence of this phenomenon).

In this project, we have dispersively coupled transmon qubits to electrical and mechanical cavities. The anharmonicity of the transmon is significantly small compared to other superconducting qubits and cannot be approximated as a simple two-level system. An accurate description of this qubit must take into account its higher energy levels. The generalised JC Hamiltonian of a transmon coupled to a microwave cavity is given by:

$$\hat{\mathcal{H}} = \sum_j hf_j|j\rangle\langle j| + hf_{\mathrm{r}}\hat{a}^\dagger\hat{a} + \sum_{ij} hg_{ij}|i\rangle\langle j|(\hat{a}^\dagger + \hat{a}), \tag{2.71}$$

where f_j ($|j\rangle$) are the transition frequencies (states) of the transmon and g_{ij} are the coupling rates. In the dispersive limit, the generalised JC hamiltonian can still be written in a similar form to equation (2.70) [43] with the only caveat that the effective dispersive shift now takes the form:

$$\chi = -g^2 \frac{E_{\mathrm{C}}}{\Delta(\Delta - E_{\mathrm{C}})}, \tag{2.72}$$

where E_{C} is the charging energy of the transmon.

2.4 Mechanical systems in the quantum regime

The quantum behaviour of macroscopic objects has been a prominent research topic in the last decade. The experimental effort primarily focused on the preparation of a mechanical system close to its motional ground state by using electromechanical and optomechanical techniques. The first implementations included a mechanical membrane parametrically coupled to a superconducting lumped-element resonator [88] as well as a patterned silicon nanobeam supporting a localised acoustic mode coupled to an optical resonance via radiation pressure [19]. Both these two techniques exploited active sideband cooling in the resolved limit in order to reach an average phonon occupancy of the mechanical system of $\bar{n} = 0.34$ and $\bar{n} = 0.85$, respectively.

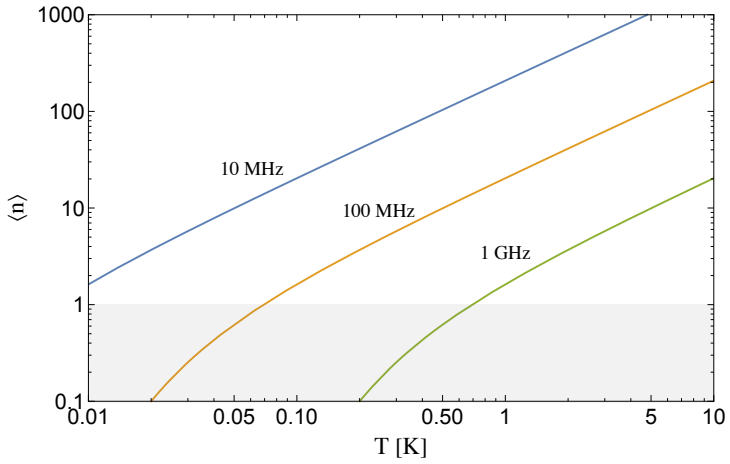

Figure 2.18 | Phonon mode occupancy. Thermal phonon mode occupancy of a mechanical resonator as a function of temperature. The shaded region indicates the quantum regime $hf < k_B T$.

A different approach to reaching the quantum limit of a macroscopic object consists of probing a mechanical resonator with working frequency of $3-10$ GHz inside a dilution refrigerator operating at ≈ 10 mK. At these temperatures, the thermal fluctations are strongly suppressed and the mechanical cavity is naturally found in its motional ground state [66] without the need for active cooling (see Fig. 2.18).

These pioneering works inspired new lines of research, including the production of squeezed states of mechanical motion [95], the observation of vacuum fluctuations of a macroscopic oscillator's motion [47], the implementation of bidirectional microwave-to-optical converters [4] and microwave amplifiers based on nanomechanical resonators [56]. During the same period, hybrid quantum devices comprising artificial atoms and mechanical systems were investigated. Dispersive coupling between a 60 MHz suspended nanostructure and a tuneable Cooper pair box was achieved in 2009 [45]. In this experiment, a frequency shift of a mechanical cavity as a function of the flux threading a superconducting qubit was observed[14]. However, the mechanical system

[14] A similar phenomenon has been observed with our acoustic platform and it will be presented in section 6.5.

was not in its quantum ground state and the phonon mode occupancy was of the order of $\bar{n} = 10^5$. One year later, direct coupling between a 6 GHz bulk resonator and a flux qubit was observed by the UCSB group [66]. When the superconducting qubit was brought into resonance with the mechanical system, qubit spectroscopy revealed an anti-crossing of the order of $g/2\pi = 60$ MHz. The direct coupling between these two quantum systems gave the possibility to prepare the mechanical resonator into a macroscopic quantum superposition of motion. Since then, the coupling between superconducting qubits and mechanical resonators has been observed in several quantum devices, including a low frequency mechanical membrane coupled to a CPB [71], a high frequency nanoresonator capacitively coupled to a transmon [78] and a bulk resonator coupled to a 3D transmon [21]. All of these experiments employed an electromagnetic resonator to readout the state of the qubit by means of a circuit-QED type of interaction.

The study of SAWs at low temperatures dates back to 1960s, when the acoustic attenuation of these propagating modes was investigated between 4 K and 300 K [81]. These experiments validated theories describing the scattering between surface waves and thermal phonons [53]. At the end of 1990s, the performance of SAW based devices was characterised at low temperatures [36, 96] and it was established that acoustic cavities in the GHz range can reach quality factors of the order of 10^4 at low temperatures. The interaction between a surface acoustic wave and a coherent electrical device was explored a decade later when the propagation of surface waves was probed by means of a single electron transistor [35]. This result was confirmed few years later when a transmon was coupled to propagating SAWs in an open transmission line configuration [35]. This experiment clearly showed that acoustic waves are predominantly reflected by an interdigitated transmon when its transition

frequency is in resonance with the acoustic perturbations. These studies have contributed to the birth of quantum acoustics, an emerging field in which acoustic waves are probed in the quantum regime and employed in hybrid systems [5]. New experiments included the interaction between classical surface waves and an electron spin in diamond [31], the study of the performance of SAW delay lines and resonators on bulk ZnO [50], the investigation of unidirectional transducers for the potential detection of phonon-phonon correlations [27] and optomechanical coupling between a circular SAW resonator and an optical cavity [67]. On the theory side, SAWs have been proposed as a viable means for the transfer of quantum information between delocalised qubits along acoustic waveguides [83]. In this work, it has been speculated that SAW resonators can in principle be coupled to spin qubits, NV centers and trapped ions with coupling strengths of the order of $g_{\mathrm{QD}} \approx 15\,\mathrm{MHz}$, $g_{\mathrm{NV}} \approx 75\,\mathrm{kHz}$, and $g_{\mathrm{TI}} \approx 3\,\mathrm{kHz}$. Furthermore, the relatively long wavelength of SAWs compared to the dimensions of superconducting qubits makes them a good candidate for studying the unusual interaction between a coherent wave and a giant artificial atom [44, 33]. Finally, SAWs have been proposed for potential phonon-photon converters based on stimulated Brillouin scattering [84].

Based on these discoveries, this thesis aims to explore the coherent interaction between a Fabri-Perot cavity based on SAWs and a superconducting qubit. The interaction between these two systems is investigated in different ways, such as measuring the acoustic Stark shift of the qubit and observing the frequency of the mechanical cavity as a function of the flux threading the tuneable qubit. We also present spectroscopic measurements of the qubit performed using an *acoustic cavity* as readout component, a type of measurement that has not yet been reported to our knowledge. Finally, we present evidence of direct coupling between a tuneable transmon and an

acoustic cavity on diamond.

Chapter 3

Experimental methods

Device reproducibility and high resolution can only be obtained with a precise and systematic fabrication methodology.

In this chapter, we present the experimental techniques adopted to fabricate and investigate SAW devices in the quantum regime. The technology required for these GHz experiments is well established due to its applications in telecommunication and microwave electronics. However, since most of our measurements are performed with an average of a single quantum of energy in the SAW cavity, signals with powers of the order of 1 fW must be efficiently controlled and analysed. Furthermore, the chip itself must be cooled down at temperatures of the order of 10 mK, where the quantum regime $hf \ll k_{\mathrm{B}}T$ can be established. Finally, tuneable charge qubits are very sensitive to external magnetic fluxes induced by microwave components and ferromagnetic materials in the surroundings. These stringent requirements imply the use of appropriate magnetic shielding, wiring, filtering and amplification of the microwave signals used to interrogate our samples.

This chapter is divided into several sections. The first sections deal with the fabrication procedure of our devices. We then move on to present the 3D cavities used for the characterisation of our superconducting qubits. The last sections are

dedicated to present our cryogenic setup and the electronic apparatus employed to measure our samples.

3.1 Design and fabrication

Four fabrication procedures were adopted in this thesis:

1. photolithography for 500 MHz SAW devices with wavelength of 6 μm,
2. photolithography and electron beam lithography for 2 - 4 GHz SAW devices with wavelength in the range 300 - 1000 nm,
3. photolithography and electron beam lithography with double-angle evaporation techniques for circuit-QAD experiments,
4. electron beam lithography and double-angle evaporation techniques for the fabrication of Josephson junction tests.

We briefly describe these fabrication procedures:

1. For 500 MHz SAW devices, the entire chip (including the waveguides, the ground planes and the SAW resonator itself) was fabricated with standard photolithographic techniques. This gave us the possibility to create approximately 50 different designs in a single lithographic step (an example of a 500 MHz CAD design is shown in Fig. 3.1a). The photolithography consists of a negative lift-off recipe developed in the course of this project (see Section 3.2 for more details). The patterned structure was made of a metallic bilayer: a 5 nm Ti film was deposited between the crystal and a 95 nm Al layer. The titanium was used as sticking layer with the substrate. Furthermore, aluminium wire bonds attach well to titanium and make the bonding process easier. Aluminium was chosen because of its specific properties: it is easy to evaporate, it becomes superconducting below 1.2 K and it has a low mass loading.

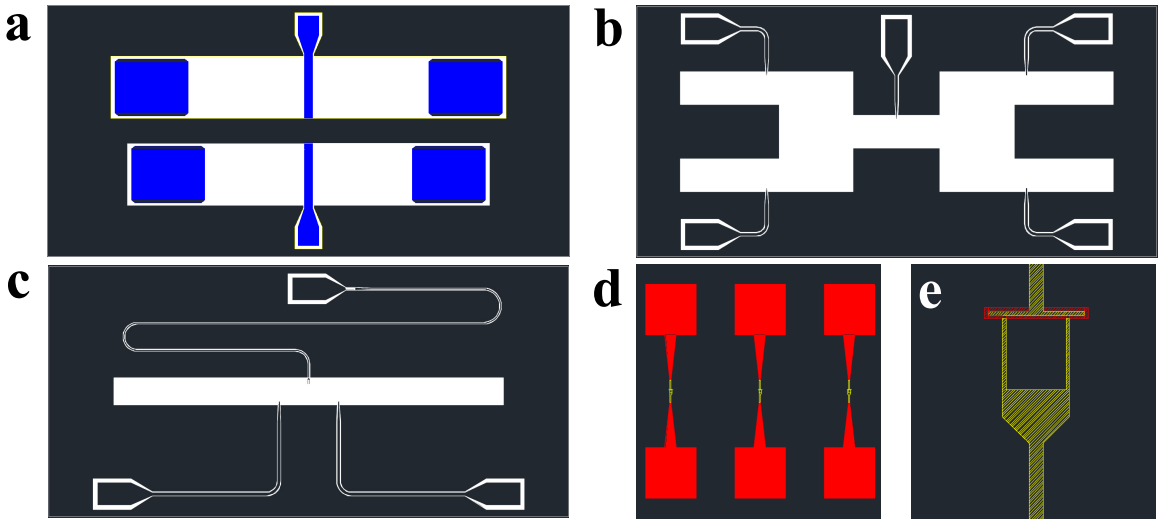

Figure 3.1| Templates and exposure patterns. **a**, Autocad template of a 500 MHz SAW device fabricated with photolithography techniques. The ground planes are depicted in slate, and the SAW resonator in light blue. On this $10 \times 5\,\mathrm{mm}^2$ chip, two 1-port SAW resonators are measured in reflection. **b**, Autocad template of a $10 \times 5\,\mathrm{mm}^2$ chip for measuring 2 - 4 GHz SAW devices. The SAW resonators were patterned in a second electron beam lithography step in the white areas of the template. This template offers the possibility to measure five 1-port SAW resonators in reflection. **c**, Template for circuit-QAD experiments with one CPWR and two measurement ports. The SAW device was patterned in a second electron beam lithography step in the middle of this $10 \times 5\,\mathrm{mm}^2$ chip. **d**, Template for room-temperature junction testing with six $100 \times 100\,\mu\mathrm{m}^2$ pads (red) connected in pairs by a SQUID loop (yellow). **e**, Close-up of the $4 \times 4.57\,\mu\mathrm{m}^2$ SQUID loop (yellow) and under cut boxes (red) for electron beam exposure.

2. For 2 - 4 GHz SAW devices, a two-step fabrication procedure was employed. The waveguides, ground planes and alignment marks were patterned with photolithography. Figure 3.1b shows a $10 \times 5\,\mathrm{mm}^2$ photolithography template used to fabricate these devices. The metallic structures consisted of a 5 nm Ti - 55 nm Au bilayer. Gold was used for two main reasons: it has a high conductivity (hence, the alignment marks are easy to detect with an electron beam) and it does not oxidise. This implies that metallic structures deposited on top of it have a good metallic contact. The SAW resonator itself was patterned in a second electron beam lithography (EBL) step and it consisted of a 30 nm Al layer.

3. Circuit-QAD chips were fabricated in two steps. CPWRs, ground planes and alignment marks were patterned with photolithographic procedures. Figure 3.1c shows an

example of a photolithography template used to fabricate these devices. The metallic structures deposited after the photolithography consisted of a 3 nm Ti - 97 nm Al bilayer. The SAW resonator and tuneable transmon were fabricated in a second EBL step. In this case, a double-angle evaporation technique was adopted to fabricate these 30 nm Al - 60 nm Al structures including an intermediate in-situ oxidation (see Section 3.3 for more details). When designing these devices, several parameters must be considered: the Coulomb energy E_C (set by the geometry of the qubit capacitance), the Josephson energy E_J (set by the oxidation pressure and time), the coupling strength g (λ) between the transmon and the CPWR (SAWR) and the coupling between the external measurement ports and the microwave cavities. The desired combination of these parameters can be obtained with an appropriate choice of geometry and fabrication.

4. The Josephson junction tests for room-temperature resistance measurements were fabricated in one step of electron beam lithography. Figure 3.1d shows the CAD design of three junction tests in which six $100 \times 100\,\mu m^2$ pads are connected in pairs by a SQUID loop. Details of the SQUID loop are shown in Fig. 3.1e. The fabrication of these Josehson junctions was conducted with standard techniques which will be presented in Section 3.3.

Sample holder and mounting

After fabrication, the devices were mounted and glued to a home-made oxygen-free copper sample holder. This material was chosen as it does not contain ferromagnetic elements that might induce undesired fluxes through the qubit SQUID loop. In addition, it has a superb thermal conduction that guarantees good thermalisation at cryogenic temperatures. The two sample holders used in this thesis are shown in

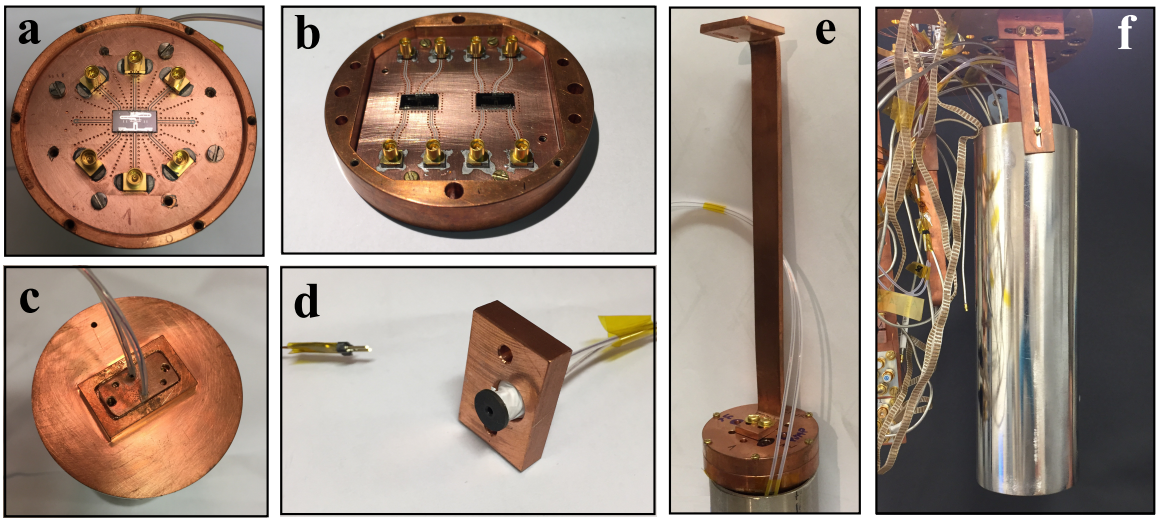

Figure 3.2| Sample holders and shielding. **a**, Small home-made oxygen-free copper sample holder for SAW device characterisation. It comprises one centre slot that can accommodate a $10 \times 5\,\mathrm{mm}^2$ chip. A maximum of six lines can be connected to the chip. A superconducting coil can be placed on the back of the sample holder. **b**, Big home-made oxygen-free copper sample holder for SAW device characterisation. In this picture, it accommodates two $10 \times 5\,\mathrm{mm}^2$ SAW devices. A copper lid was placed on top of the devices to shield them from electromagnetic noise. **c**, Back of the small sample holder showing the two DC lines that feed the superconducting coil. **d**, Home-made superconducting coil positioned inside a dedicated copper holder. **e**, Copper slab used to attach the sample holder to the bottom plate of the dilution refrigerator. **f**, Magnetic shield surrounding the small sample holder.

Fig. 3.2a-b. Both of them have a circular shape so that they can be easily placed inside dedicated cylindrical magnetic shields. In addition, they have milled blind holes on their back that can accommodate small coils with total diameter of 7 mm for magnetic field biasing of the qubits (see Fig. 3.2c-d). In order to minimise the volume of parasitic electromagnetic modes, a copper lid was placed on top of the chip. This lid filled the empty volume between the printed circuit board and the sample holder improving the electromagnetic environment surrounding the device.

The sample holders are mechanically anchored to the bottom plate of our dilution refrigerator. This is done with a copper slab screwed into the sample holder shown in Fig. 3.2e. When two solid surfaces are pressed together, the heat flows across their interface and the thermal conductance increases approximately linearly with

the applied force. In order to have a good thermalisation, it is recommended to apply a strong force when tightening the copper slab to the sample holder. For this reason, we have opted for screws of size M3 or greater (threads with smaller size can easily be damaged when subject to large torques since copper is a soft material). Finally, the sample holders and the copper slab are connected to the bottom plate and surrounded by a magnetic shield as shown in Fig. 3.2f. This shield prevents external magnetic fields interfering with our flux tuneable qubit.

Superconducting coils

The body of the coils is made of Torlon 4301 with inner diameter of 2.5 mm. A superconducting wire[1] SC-T48B-M from Supercon Inc. was wound around the solid body of the coil with a manual winder. The total number of turns was 4000, for a total length of about 40 m. Taking into account that the area of the qubit SQUID loop was $4 \times 4.57\,\mu\text{m}^2$ and that the distance between the chip and the edge of the coil was approximately 2 mm, this led to a qubit-flux periodicity of about $700\,\mu$A. Bias lines with common twisted pairs were used to connect the superconducting coils to an external power supply. These bias lines were also connected to intermediate RF filters placed at the 50 K plate of our dilution refrigerator in order to suppress high-frequency noise.

The coils were mounted on little metal supports and screwed into the sample holders. The end of the superconducting wire was soldered to a copper wire 30 cm long and inserted into thin plastic tubes as shown in Fig. 3.2d-e. Finally, these copper wires were soldered to metal crimps and connected to the bias lines fed by an external power supply.

[1] It consists of a single filament NbTi alloy clad with high conductivity cryogenic grade copper. The bare diameter is 0.025 mm, the insulated diameter is 0.036 mm.

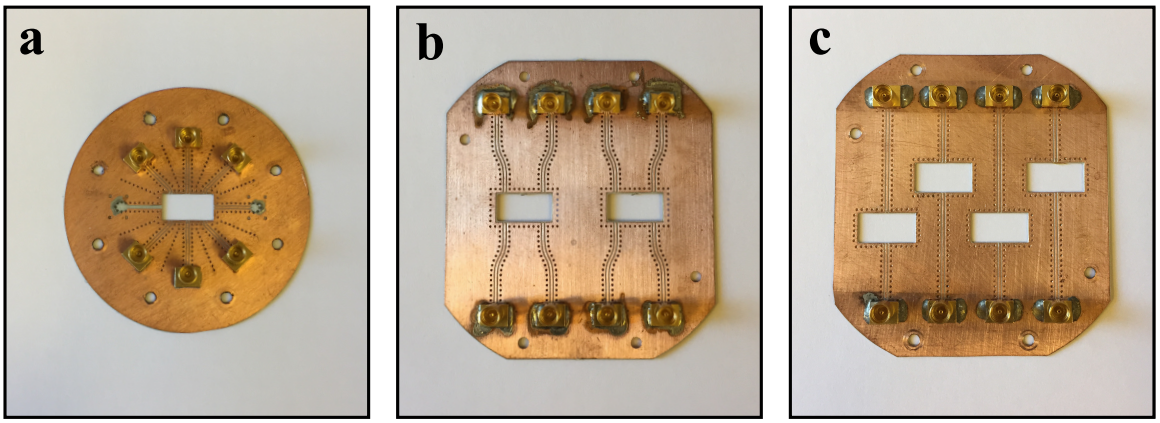

Figure 3.3 | Printed circuit boards. **a**, Printed circuit board for the small sample holder. It includes six SMA connectors and six waveguides for reflection and transmission measurements of $10 \times 5\,\mathrm{mm}^2$ chips. **b-c**, Circuit board designs for the big sample holder.

Printed circuit board and wire bonding

Printed circuit boards (PCBs) provided a good way to connect microwave cables to our superconducting devices. They were designed with a CAD software and made of a 0.25 mm thick Roger's dielectric with permittivity of 3.47 and with 17.5 μm thick electrodeposited copper[2] on both sides. A good PCB design aims to minimise the mismatch between the 50 Ω microwave cables and the PCB waveguides with nominal impedance of 50 Ω. The parameters characterising PCB waveguides are: the width W of the central conductor, the gap G between the central conductor and the ground planes, and through-hole vias connecting the two circuit board faces, for the suppression of stray resonances. We have tested the transmission coefficients $S_{12}(f)$ of several PCB waveguides with different W/G ratios and via geometries in order to find the best experimental configuration. These tests led us to adopt $W = 404\,\mu$m, $G = 163\,\mu$m and vias with diameter 500 μm separated by 900 μm. Finally, each circuit board had $10.2 \times 5.2\,\mathrm{mm}^2$ cutouts to accommodate our superconducting devices. Three different PCB designs are shown in Fig. 3.3a-c.

[2]The circuit board material was purchased from Rogers Corporation.

SMA connectors were soldered to the PCB using leaded solder paste. The circuit board was then cleaned in an ultrasonic bath with 1:10 citric acid - H_2O solution at 40 °C. The devices were glued to the sample holder with GE varnish (suitably diluted in a 1:1 Toluene:Methylated Ethil Alcohol solution) which typically dries in few minutes[3]. The devices were bonded to the circuit board with aluminium wires of thickness $\approx 30\,\mu$m using a Kulicke&Soffa series 4500 model 4523 manual wire bonder. At least three bonds were used to contact the PCB waveguides to on-chip measurement ports. As regards the ground planes, they were connected to the circuit board with approximately 8 bonds per millimetre. Shorter wire bonds have smaller self inductance and hence are preferable to longer ones. Some on-chip wire bonds were employed to connect ground planes of the device separated by waveguides. These on-chip bonds tend to suppress spurious modes of electromagnetic waveguides. It must be noted, however, that wire bonding can be substituted with more robust and less invasive connections coming directly from the top of the device [8, 75].

3.2 Photolithography

Fabrication is a crucial part of circuit QAD experiments due to the small and complex features of the chip components. Device reproducibility and high resolution can only be obtained with a precise and systematic fabrication methodology. The main fabrication steps presented in the following subsections are substrate cleaning, exposure, development, evaporation and lift-off (see Fig. 3.4 for a schematic of the photolithographic steps). All of these steps were conducted in the Clarendon and Denys Wilkinson cleanrooms in Oxford.

[3]Silver paste can be used in place of GE vernish. However, it is recommended not to use it with GaAs because this substrate expands during the cool down in the range of 40 - 50 K, whereas silver paste contracts. These different coefficients of thermal expansion potentially induce cracks in the substrate.

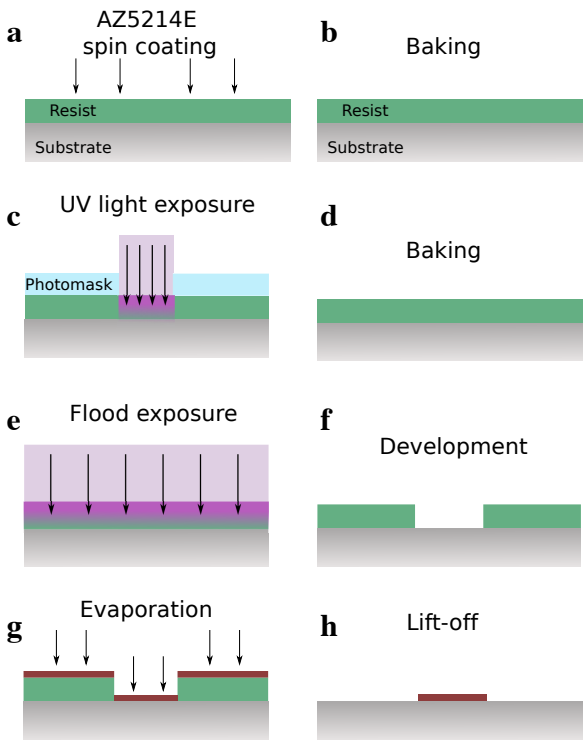

Figure 3.4 | Photolithography. Schematic of the photolithographic steps.

Substrate cleaning

The starting point of a good fabrication procedure is obviously the substrate cleaning. The wafers were initially cleaned in an acetone beaker followed by a rinse in isopropanol. If the wafer had some resist on top (due to prior fabrication steps), this first cleaning was followed by a more aggressive cleaning in an ultrasound bath of DMSO at a temperature of 80 °C followed by a rinse in hot DI water[4]. The wafers were finally cleaned with oxygen plasma ashing at 100 W for one minute. The photomask was left soaking in a home-made PTFE holder filled with hot DMSO for at least 20 min, especially if it had been used with a hard contact in previous photolithographic exposures. These steps were followed by a thorough rinse with DI water. Alternatively, the photomask can also be cleaned with a cotton bud and

[4]This aggressive cleaning step revealed to be crucial especially when the wafer was still covered by some resist from previous fabrication steps.

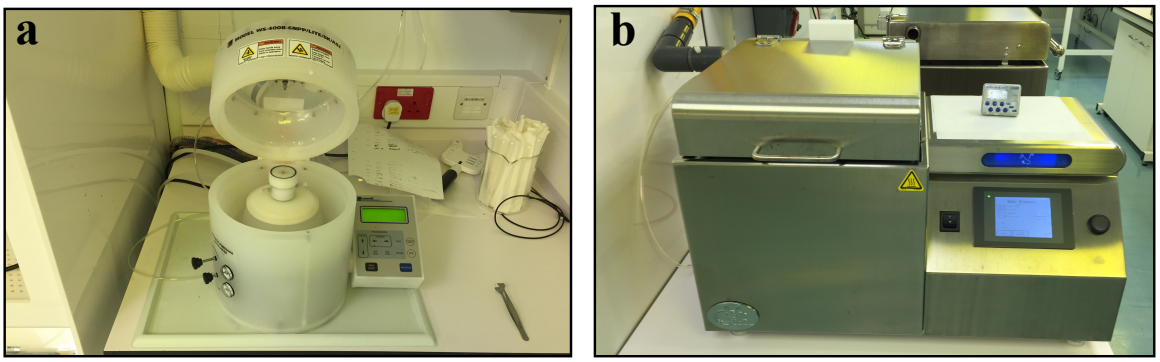

Figure 3.5 | Cleanroom tools. a, Spin coater used for resist deposition. The spin coating included an initial ramp at 500 rpm for 10 sec. **b**, Digital hot plate.

appropriate surfactants.

Spin coating and baking

The adhesion between the resist and the wafer is a crucial part of a lithographic recipe[5]. In this project, several substrates have been used including silicon, GaAs, quartz, ZnO, sapphire and diamond. To improve the adhesion between the resist and quartz, ZnO, sapphire, diamond substrates, a layer of adhesion promoter Ti-Prime was spin coated before the resist. This was done with a spin coater (shown in Fig. 3.5a) that spun the wafer at 3000 rpm for 30 sec. The wafer was then baked on a hot plate (shown in Fig. 3.5b) at 120 °C for 120 sec. Baking can be regarded as a time integral of the heat transferred to the resist. In order to keep this step as consistent as possible, the wafer was systematically cooled down on a metallic surface.

A small bottle of photolithography resist AZ5214E with opaque walls was kept in a closed cabinet at all times to prevent undesired exposure from UV light. When dealing with resist sensitive to UV light, it is good practice to eliminate UV components from cleanroom lights and use a yellow ambient lighting. The resist was distributed

[5]Before spinning the resist on the substrate, it should be checked that the crystal surface is hydrophobic. This can be tested by placing few water droplets on the crystal. Ideally, the water droplets should form well defined semi-spheres. If this is not the case, oxygen plasma cleaning might improve the surface chemistry and thus the resist adhesion.

uniformly on the wafer with a pipette until its surface was entirely covered. The rpm was set at 5000 for 45 sec leading to an overall resist thickness of 500 nm. The wafer was then baked at 110 °C for 50 sec. Before the spin coating, a nitrogen gun was used to remove dust particles from the substrate.

Particular care was taken to remove a 1 mm line of resist from the edges of the wafer with a cotton bud immersed in IPA. This step improved the contact between the wafer and the photomask during exposure. Finally, the wafer was always handled with tweezers from the same edge to reduce the contact area of these metallic tools with the substrate.

First exposure

The photomask was mounted on a EVG620 mask aligner (shown in Fig. 3.6a) and aligned using two optics. The wafer was then mounted on a 3" inch chuck with a central glass porthole surrounded by a plastic border (see Fig. 3.6b). The glass had several carved grooves on the back connected to a vacuum line. Suction on the reverse side ensured that the wafer was kept still during the entire process.

The wafer was placed under the photomask with a separation distance of 30 μm. By adjusting the optical focus and the stage, the substrate was manually aligned to the photomask. The contact between the substrate and the wafer is of paramount importance for obtaining micron features (recall that 500 MHz SAW devices on quartz have a gap between adjacent fingers of 1.5 μm). In order to obtain the desired resolution, the contact between the wafer and the photomask was set to "hard + vacuum", meaning that the photomask was strongly pressed onto the wafer and that an external vacuum line was pumping out the air between the wafer and the photomask. The vacuum option can be exploited only if the chuck supporting the wafer has the afore-

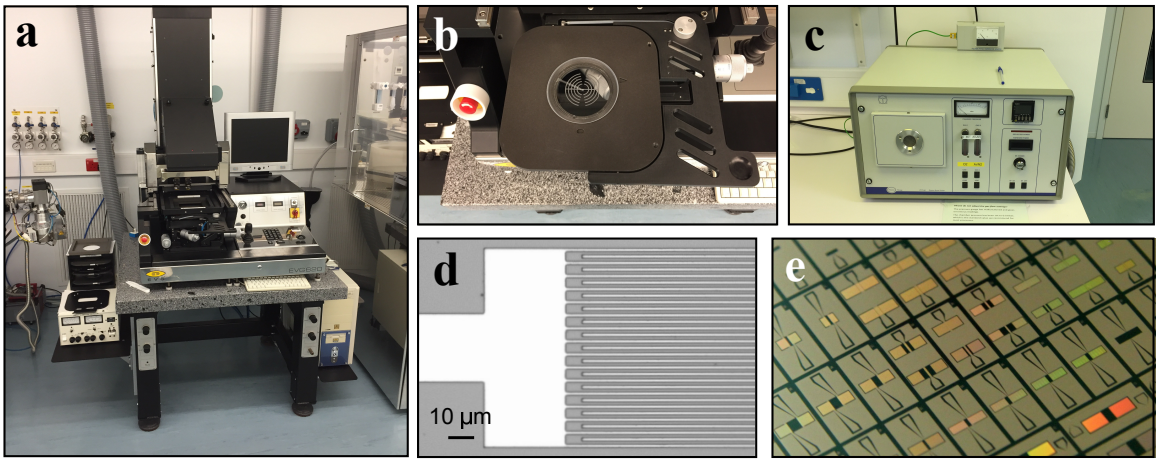

Figure 3.6 | Photolithography. **a**, EVG-620 mask aligner. **b**, Chuck for 3" wafers with a plastic hem used for the vacuum contact. **c**, Oxygen plasma asher. **d**, Optical image of an interdigitated transducer after development. **e**, Detail of a quartz wafer after lift-off, showing several $10 \times 5\,\mathrm{mm}^2$ chips. Each rectangular rainbow corresponds to a grating.

mentioned plastic border surrounding the glass stage. It has been noted that both the "vacuum" contact and the "hard" contact alone were not sufficient to achieve micron resolution and the "vacuum + hard" contact had to be used. This type of contact was the only one that did not lead to diffraction issues that considerably degrade pattern resolution.

Several dose tests are usually necessary to determine the right exposure energy for each substrate. In this project, the doses were: $15\,\mathrm{mJ/cm}^2$ for sapphire and ZnO, $35\,\mathrm{mJ/cm}^2$ for quartz, and $45\,\mathrm{mJ/cm}^2$ for GaAs and silicon. After development, the experimentalist might opt to increase or decrease the exposure dose to achieve the desired resist undercut. If, after development, the resist has not been removed from areas that were not exposed to UV light, then the exposure energy must be reduced.

Using a "vacuum + hard" contact implies that the photomask and the wafer get firmly pressed together and some resist residues might stick to the photomask. Hence, it is good practice to clean the photomask before starting a new exposure.

Intermediate baking and flood exposure

The wafer is baked on a hot plate at 120 °C for 120 sec and placed on a metallic surface to cool down. As the substrate reaches room temperature, it is possible to note a change in the resist colour and the exposed pattern becomes visible. The wafer is mounted again on the mask aligner for a flood exposure with exposure energy of 200 mJ/cm^2. This exposure is performed without any photomask mounted on the mask aligner.

Development

The wafer is immersed in a AZ726MIF developer at room temperature in order to remove the resist that was not exposed by UV light. The development time varies from one substrate to another: for ZnO, sapphire and quartz this was set to 120 sec, whereas for silicon and GaAs a shorter development time was used. During the development, it is possible to note some resist lifting from the substrate[6]. This usually takes place 20 sec after the immersion. From that time onwards, the wafer can be left inside the developer to increase the resist undercut. Note that the development time is not a crucial parameter of this lift-off recipe as long as the exposure dose is properly chosen. The wafer is then immersed in DI water and blow dried. Finally, the substrate is cleaned with a gentle oxygen plasma set at 20 W for 15 sec (shown in Fig. 3.6c) in order to remove fine residues from its surface. Alternatively, the wafer can be baked at 80 °C for 50 sec. Figure 3.6d shows an optical image of a transducer after development.

[6]During the development, the wafer should be shaken up and down. In principle, this can be done with a wafer dipper, but it has been noted that this tool might introduce some contamination into the beaker. For this reason, we have preferred to use a pair of clean tweezers for this operation.

Evaporation

The wafer is placed inside a home-made electron beam evaporator[7] for metal deposition. This evaporator has two main chambers separated by a gate valve: the upper chamber accommodates the devices on a 360 ° rotating stage, while the lower chamber contains four crucibles each containing pellets[8] of 99.995% pure titanium, 99.95% pure palladium, 99.999% pure gold and 99.999% pure aluminium. When the devices were loaded into the evaporator, the upper chamber was brought to room pressure by injecting some nitrogen into it (this allowed for shorter pump-down times). The upper chamber was provided with two pressure sensors working in the range of 0.1 - 1000 mbar and 10^{-8} - 10 mbar, respectively. The lower chamber instead was provided with a pressure sensor working in the range 10^{-8} - 10 mbar.

The substrate was usually left overnight inside the evaporator so that the lower chamber could reach a base pressure of $\approx 1 \times 10^{-7}$ mbar. To decrease the base pressure even more, few nanometers of titanium are evaporated before the actual deposition. Titanium strongly interacts with H_2O particles largely reducing the water content and the overall pressure[9]. The evaporation rate was set at 0.25 nm/s for Ti and Au, 0.5 nm/s for Al and it was performed at a right angle. The typical pressure inside the chamber during aluminium deposition was 1×10^{-6} mbar which is significantly higher than that of other evaporators on the market. A quartz crystal placed inside the lower chamber constantly monitored the thickness of the metal deposited on the substrate with a precision of ± 0.5 nm. Before taking the wafer out of the evaporator, the upper chamber was filled with 100 mbar of oxygen - nitrogen mixture for 100 sec.

[7] This evaporator was designed by Dr. Peter Leek and programmed by Andrew Patterson.

[8] These pellets were purchased from Kurt J. Lesker. They have a diameter of 1/8" and and they are 1/8" long.

[9] This process was directly monitored with a mass spectrometer connected to the upper chamber.

This operation contributed to the creation of a uniform oxide layer on top of the metallic structure before coming in contact with air.

Lift-off

Once the thin-film deposition is done, the resist has to be removed from the substrate. We performed this step by immersing the wafer in a hot bath of DMSO (or NMP) for at least 30 min at 65 °C. Higher temperatures can produce little bubbles under the thin metal, probably due to the fact that small bits of resist (that have not been removed during the development) try to escape through the metal. In order to facilitate lift-off, a clean pipette was used to carefully blow off the metallic layer from the wafer. For 2 - 4 GHz SAW devices, instead of using a pipette, the device was sonicated in a DMSO bath for 30 sec with 80 kHz ultrasound waves at relatively low power. This turned out to be a good method for lifting off the fine metallic structures of SAW resonators.

Before the wafer is taken out from DMSO, it is necessary to inspect the device to make sure that all of the features stripped off correctly. To facilitate this, the wafer is left inside the beaker and checked with an appropriate optical microscope. If the structures did not lift-off completely, the lift-off process was continued using the pipette (or sonication). The wafer is then placed in hot DI water[10] and then blow-dried. Figure 3.6e shows details of a quartz wafer after lift-off. The wafers were kept inside a vacuum box until they were ready to be diced.

Dicing

Some photoresist was spun on the wafer at 5000 rpm for 50 sec and then baked on a hot plate at 110 °C for 50 sec. This resist layer protected the wafer during the dicing

[10]DMSO becomes solid at $\approx 16\,^{\circ}$C. This implies that if the wafer is moved from a hot DMSO beaker to a cold water beaker, DMSO might instantly solidify on the surface of the wafer.

procedure. Dicing is an invasive process that might seriously damage the substrate. In fact, if the spindle speed and feed rate are not properly selected, the blade might cause cracks to the substrate. It is good practice to perform some cut tests until the right parameters have been found. In addition, the wafer must be firmly attached to a tape, otherwise the chips can tear away during the dicing. The parameters that we used in our dicing step were as follows:

- For quartz and silicon, we used a 150 μm thick diamond blade P1A851 from Disco. For these materials, the spindle speed and feed rate were set at 20000 rpm and 5 mm/sec, respectively.

- For sapphire, we used a 250 μm thick diamond blade B1A801 from Disco. The spindle rate and feed rate were set at 15000 rpm and 1 mm/sec, respectively.

- GaAs is a very brittle material. In this case, we opted for a 'scribe and break' technique; a partial scribe cut is made with a scribe tool to initiate the crack for the break along a desired cleavage plane. The wafer was then broken by exerting a force along that line.

When dicing a wafer into $10 \times 5\,\mathrm{mm}^2$ chips, it is convenient to start with cuts separated by 10 mm and then proceed with cuts with 5 mm periodicity; this reduces the chances that the chips separate from the tape.

During the dicing process, water constantly flows on the blade to cool it down. This also implies that water constantly runs over the wafer potentially spreading small bits of debris. After dicing, the layer of resist protecting the pattern can be removed with acetone and IPA followed by a more aggressive cleaning in DMSO at 65 °C.

3.3 Electron beam lithography

An electron beam lithography resist is spun onto the chip directly after the cleaning procedure. For the fabrication of 2 - 4 GHz SAW devices, we have used a polymethyl methacrylate resist with a large molecular weight of 950000 diluted in anisole (in short, PMMA 950k A3). When dealing with $10 \times 5\,\mathrm{mm}^2$ chips, it is important to deposit the right amount of resist on the chip[11]. Hence, we used a calibrated dispenser pipette (Pipetman Classic P100 from Gilson). By placing a sterile plastic tip (Pipetman tips Diamond D200 from Gilson) on this pipette, a single droplet of resist is deposited on the chip in a very controlled way. Before spinning, we waited 20 sec to give the resist time to adhere to the substrate. The spin coating was performed at 4000 rpm for 45 sec leading to an overall thickness of ≈ 130 nm. This resist thickness was ideal[12] for devices with finger spacing of 200 - 500 nm and with metal thickness of 30 nm. After spinning, the resist is quite uniform in the centre of the device and it forms edge beads approximately 500 μm wide close to the perimeter. The chip is then baked on a hot plate at 180 °C for 5 min.

For the fabrication of circuit QAD devices, a bilayer of EBL resist was spun onto the chip. The first layer consisted in a pure copolymer of methyl methacrylate and methacrylic acid [P(MMA-MAA) in short]. Spinning this fluid at 4000 rpm for 45 sec led to a resist thickness of ≈ 570 nm. This layer of copolymer is very sensitive to direct, secondary and backscattered electron exposure and it serves as a spacer between the substrate and a second resist layer allowing for a pronounced undercut. After baking on a hot plate at 180 °C for 5 min, the same spin coating and baking was repeated

[11] If too much fluid is used, some of it might eventually reach the back of the chip and this will prevent the device from laying flat in the e-beam lithography system later on.

[12] As a rule of thumb, the resist should be three times higher than the thickness of the evaporated metal in a lift-off recipe.

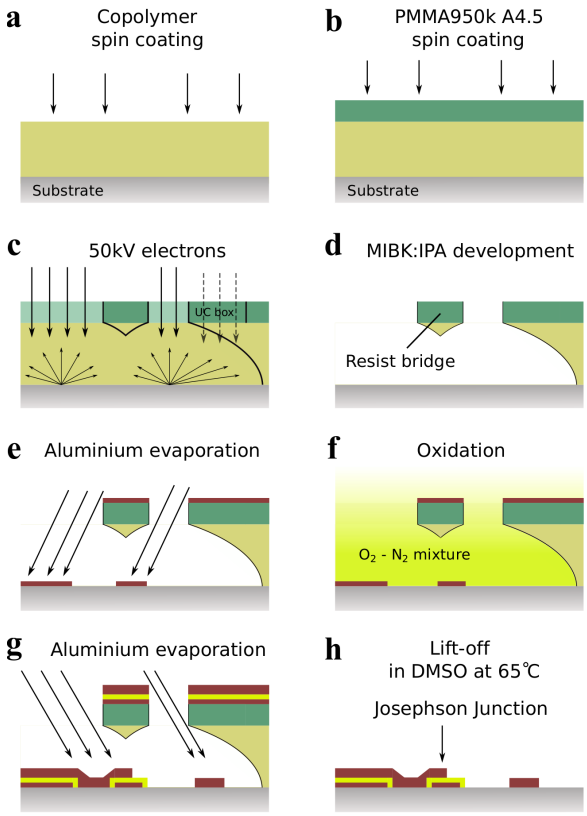

Figure 3.7 | Double-angle evaporation. Schematic of the fabrication of a device comprising Josephson junctions.

with PMMA A4.5. These two resist layers are widely used in the superconducting device community to fabricate $\approx 200 \times 200\,\mathrm{nm}^2$ Josephson junctions with the Dolan bridge technique. Particular care must be taken when exposing insulating substrates, such as quartz, ZnO, sapphire and diamond. For these materials, backscattering and charging phenomena can significantly compromise the exposure. For this reason, it is advisable to spin a discharging layer on top of the EBL resist, such as Electra92 (AR-PC 5090) from AllResist. This discharging layer can be spun at 3000 rpm for 30 sec and it does not need to be baked.

The chip was exposed with a JEOL 5500 series Electron Beam Lithography System. A 50 kV acceleration voltage with aperture 2 and a 1 nA current was used to expose fine features. For the fabrication of Josephson junctions, some undercut

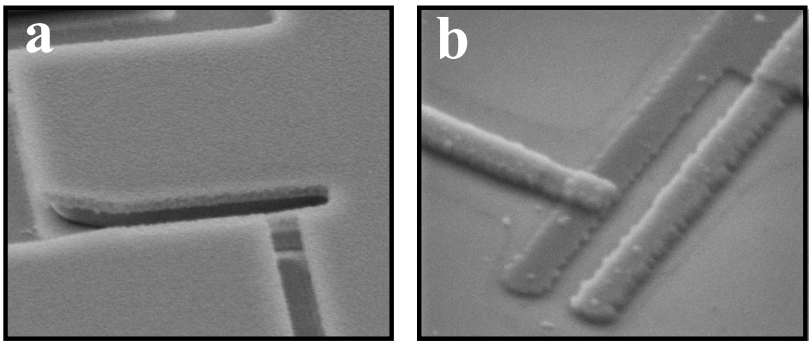

Figure 3.8 | SEM of Josephson junctions. **a**, SEM image of a Josephson junction test after development showing a Dolan bridge 200 nm wide. **b**, SEM image of a $200 \times 200\,\mathrm{nm}^2$ Josephson junction after lift-off.

boxes were used to create the desired undercuts in the resist. The main steps of electron beam lithography and double angle evaporation are illustrated schematically in Fig. 3.7.

Development

After the EBL exposure, the Electra92 discharging layer is removed by rinsing the chip in a water beaker for 1 min. The device is carefully blow-dried with a nitrogen line. The EBL resist is developed in a 1:3 MIBK:IPA solution which provides a low selectivity for the PMMA and a high sensitivity for the copolymer layer. After 50 sec of careful moving, the chip is immersed for other 15 sec in IPA and then blow dried with a nitrogen gun. The device is inspected with an optical microscope and kept inside a vacuum box until the final evaporation. Figure 3.8a shows a Josephson junction test after development.

Double angle evaporation and oxidation

Shadow evaporation is the most common established technique to produce Josephson junctions[13]. This process consists of depositing two layers of metal in two different

[13]More robust bridge-free techniques have been recently developed that permit a more aggressive cleaning of the substrate before the evaporation step. These techniques, however, require an evap-

steps at two different angles with an evaporation rate in the range of $0.2 - 1\,\mathrm{nm/s}$. Between the two depositions, an oxidation step is performed with a mixture of 85% nitrogen - 15% oxygen. This mixture is kept under high pressure in a bottle attached to the upper chamber of the evaporator (shown in Fig. 3.9a) with a double stage pressure regulator and a needle valve that allows for controlling a constant low flow rate down to 0.1 mbar/sec. The oxygen oxidises the first aluminium film resulting in a thin aluminium oxide layer with a thickness of the order of a nanometer depending on the oxidation time and pressure.

The first 30 nm layer of aluminium is deposited at an angle of $27\,^\circ$. It is followed by an in-situ oxidation step. The main parameters here are the oxidation time and pressure. The pressure of the N_2 - O_2 mixture is set at 4 mbar, whereas the oxidation time is varied in order to obtain the desired junction resistance. Typical oxidation times in the range of 1 - 10 min create junction resistances in the range of 3 - 25 kΩ. It can be challenging to achieve a consistent junction resistance since its value depends on many variables including oxidation time, oxidation pressure, junction area, and the water content within the chamber[14]. It is important to perform some tests and check the junction resistance before the evaporation of the final device. After the oxidation step, the gas is pumped out and a second 60 nm layer of aluminium is evaporated at angle of $-27\,^\circ$. The upper aluminium layer overlaps with the bottom one and it forms the top electrode of the Josephson junction. The final result is a sub-micron Josephson junction comprising a bottom and top aluminium electrodes separated by a nanometer insulating layer as shown in Fig. 3.8b. The final step of

orator equipped with a stage that can rotate around both the azimuthal and the polar axis. Our evaporator does not have this facility and it could be a point to consider in the context of improving our fabrication process.

[14]The water can act as a catalyst for the formation of the junction dielectric layer largely reducing the oxidation time needed to obtain a specific junction resistance.

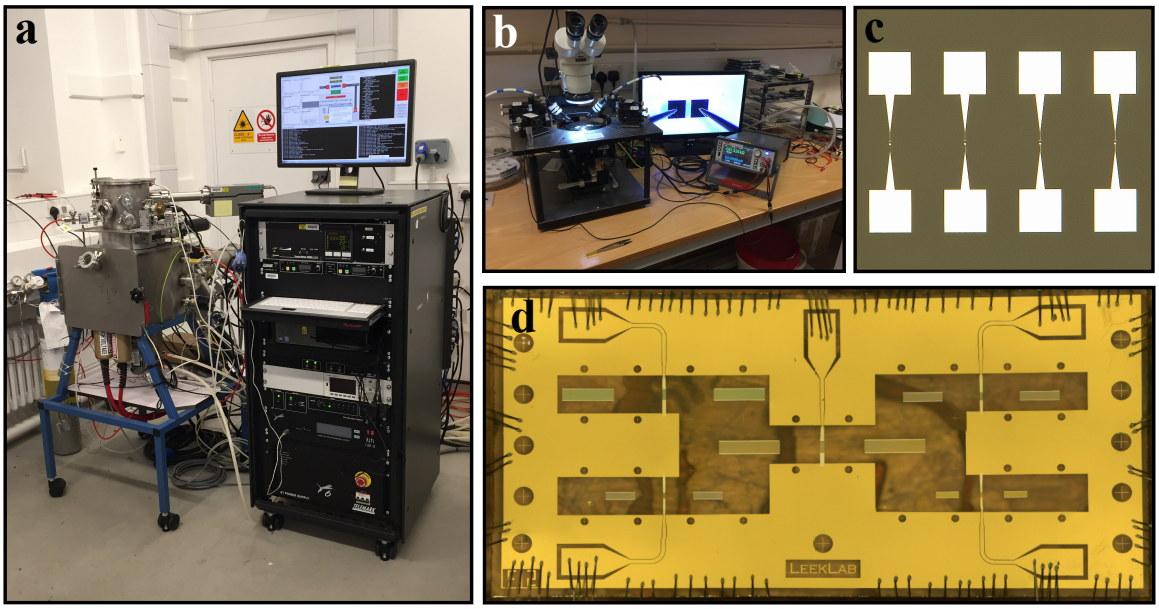

Figure 3.9 | Evaporator, probe-station and bonding. **a**, Home-made electron beam evaporator. **b**, Probe station for room-temperature resistance measurements of the Josephson junctions. **c**, GaAs wafer after lift-off comprising several 500 MHz SAW devices. The rainbow colours are due to the diffraction of the ambient light on the periodic structures of the chip. **d**, Five 2 - 4 GHz SAW devices after bonding.

the procedure consists in post-oxidation with the N_2 - O_2 mixture at 100 mbar for 100 sec (the pressure and oxidation time are irrelevant in this case as long as these parameters are high enough to saturate the oxidation).

The chip was taken out from the evaporator ready for the lift-off. When performing the lift-off of superconducting qubits, sonication of the chip is not recommended, because this can damage the Josephson junctions. It is preferable to use a clean pipette to gently blow off the aluminium layer covering the resist.

Testing Josephson junctions and SAW devices

We measured the room-temperature resistance of the junctions with a DC probe station from Semiprobe (Lab Assistant model) and a Keithley 2450 Sourcemeter shown in Fig. 3.9b. The probe station can be used to carefully contact very fine probe needles to the $100 \times 100\,\mu m^2$ aluminium contact pads. The Sourcemeter is an

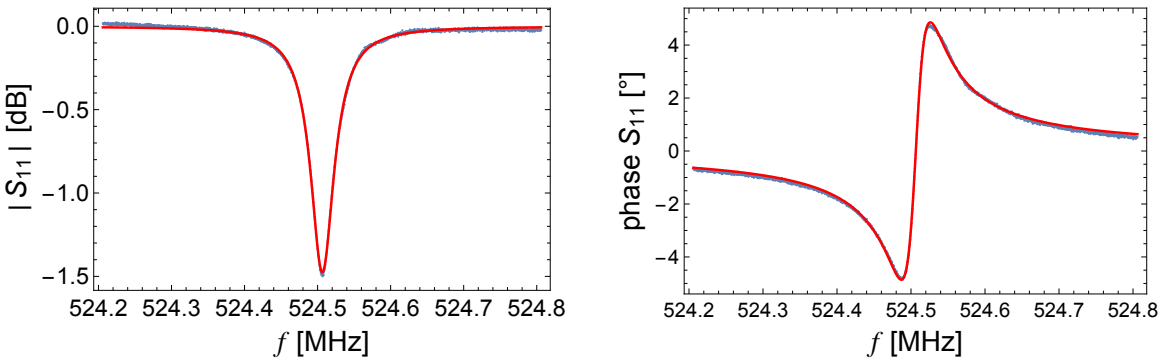

Figure 3.10 | Reflection coefficient. Measured reflection coefficient $S_{11}(f)$ at room temperature for device $p1$ (see Table 4.1). **a**, Magnitude response. **b**, Phase response. The solid red curve is a fit to equation 6.2 with parameters $Q_\mathrm{i} = 13300$, $Q_\mathrm{e} = 157100$, $f_0 = 524.51$.

electronic instrument that can apply small voltages and it is designed in such a way as to prevent any electrical discharge. When testing Josephson junction resistance, we usually fabricated 10 junctions on a single $10 \times 5\,\mathrm{mm}^2$ chip. An optical image of such a chip is shown in Fig. 3.9c. The junction resistance is measured by applying a voltage of 0.1 mV with the Sourcemeter across the junction. Our fabricated junctions usually had a resistance in the range of 5 - 20 kΩ with values fluctuating by 1 kΩ.

SAW devices were bonded to the circuit board (as shown in Fig. 3.9d) and measured with a VNA. SAW resonators with working frequencies in the range 0.5 - 2 GHz show well defined resonances at room temperature[15] (see Fig. 3.10). The performance of SAW devices significantly increases at low temperatures especially when the thin aluminium layer becomes superconducting. In addition, during the cool down, the SAW resonance shifts in frequency due to the fact that the device contracts and the speed of sound changes slightly.

[15]This is not the case for SAW devices in the 4 - 5 GHz range, since the material quality factor Q_m at room temperature significantly limits the resonator performance and the mechanical resonances are strongly suppressed.

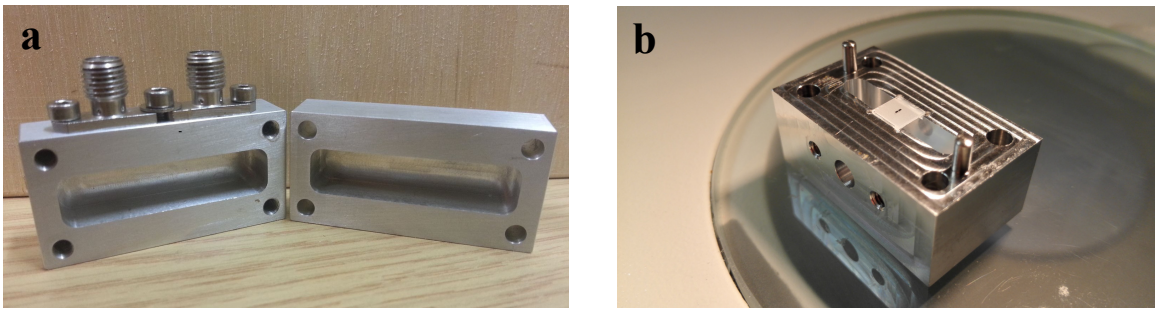

Figure 3.11 | 3D cavities. **a**, Example of 3D aluminium cavity with two SMA measurement ports. **b**, $5 \times 5\,\mathrm{mm}^2$ quartz chip positioned in the dedicated slot of the cavity.

3.4 3D cavities

A first characterisation of superconducting qubits on quartz and diamond has been performed by dispersively coupling these artificial atoms to a 3D aluminium cavity. The cavity is constructed by drilling a blind rectangular hole in two aluminium (T6061) parallelepipeds and screwing them together (see Fig. 3.11a). The cavity also has a dedicated $0.55 \times 5 \times 5\,\mathrm{mm}^3$ slot to accommodate the chip as shown in Fig. 3.11b. One of the two parallelepipeds has two small holes in which SMA pins can be inserted in order to drive an electric field inside the cavity and measure the $S_{ij}(f)$ coefficients.

The electromagnetic modes sustained by a metallic cavity can be calculated by studying Maxwell's equations with specific boundary conditions. Assuming that the cavity is perfectly rectangular with dimensions a, b, d and that the walls are highly conductive, the modes sustained by the cavity are found to be:

$$\omega_{\mathrm{r}}(n,m,l) = 2\pi f_{\mathrm{r}}(n,m,l) = \frac{c}{\sqrt{\mu_{\mathrm{r}}\varepsilon_{\mathrm{r}}}}\sqrt{\left(\frac{n\pi}{a}\right)^2 + \left(\frac{m\pi}{b}\right)^2 + \left(\frac{l\pi}{d}\right)^2},$$

where μ_{r}, ε_{r} are the permeability and permittivity constants of the material filling the cavity and n, m, $l \in \mathbb{N}$, where $n + m + l > 0$. In our case, the side b is smaller than a and d. Therefore, the lowest frequency resonant mode is:

$$f_{\mathrm{r}}(1,0,1) = \frac{c}{2\pi\sqrt{\mu_{\mathrm{r}}\varepsilon_{\mathrm{r}}}}\sqrt{\left(\frac{\pi}{a}\right)^2 + \left(\frac{\pi}{d}\right)^2}, \tag{3.1}$$

usually called TE_{101} mode. Equation (3.1) indicates that the resonance frequency of the cavity is defined by its spatial dimensions. Since the frequency of superconducting qubits usually lies between 5 - 10 GHz, the cavity frequency can be engineered to be in the same range so that the detuning between the two systems is in the order of 0.1 - 5 GHz. Note, however, that the coherence time of superconducting qubits is enhanced when they are embedded in electromagnetic cavities with resonant frequency higher than the first transition frequency of the qubit. This phenomenon is a consequence of the Purcell effect and has been studied elsewhere [43]. For these reasons, our cavity has dimensions $a = 17\,\text{mm}$, $b = 3.5\,\text{mm}$, $d = 20\,\text{mm}$ such that its resonance frequency is $f_\text{r}(1,0,1) \approx 11.5\,\text{GHz}$, a few GHz higher than the typical frequency of our superconducting qubits. As mentioned earlier, the cavity frequency depends on the material filling the cavity; therefore, depending on the material of the chip, the cavity resonance can decrease by 0.1 - 0.5 GHz.

The performance of a 3D cavity is captured by two quantities[16]: the internal quality factor Q_i and the external quality factor Q_e. The former quantifies intrinsic energy losses of the cavity and for 3D cavities can reach values of $Q_\text{i} = 10^7$; the latter takes into account energy losses due to the coupling with external measurement ports and it can be controlled by adjusting the SMA pin length. For instance, for a fast qubit readout, the SMA pin can be placed well inside the cavity so that the external quality factor is quite low $Q_\text{e} \approx 10^3$ and the electric signal quickly leaks out from the cavity.

A 3D cavity can be modelled with a parallel RLC circuit. The impedance of this circuit is given by:

$$Z(\omega) = \left(\frac{1}{R} + i\omega C + \frac{1}{i\omega L}\right)^{-1}.$$

[16]The internal and external quality factors will be discussed in more detail in Chapter 4.

The circuit is connected to a measurement circuit with load impedance Z_0 (typically $Z_0 = 50\,\Omega$). Following Pozar [74], the internal/external quality factors and the resonance frequency of this circuit can be expressed as:

$$Q_\mathrm{i} = \omega_\mathrm{r} RC \qquad Q_\mathrm{e} = \frac{Z_0}{\omega_\mathrm{r} L} \qquad \omega_\mathrm{r} = \frac{1}{\sqrt{LC}}. \tag{3.2}$$

Exploiting expressions (3.2), the impedance of the circuit close to resonance can be written in the form:

$$\begin{aligned} Z(\omega) &= \left[\frac{1}{R} + i\omega C\left(1 - \frac{1}{\omega^2 LC}\right)\right]^{-1} = \left[\frac{1}{R} + i\omega C\left(\frac{\omega^2 - \omega_\mathrm{r}^2}{\omega^2}\right)\right]^{-1} \approx \\ &\approx \left[\frac{1}{R} + 2iC\Delta\omega\right]^{-1} = \frac{R}{1 + 2iRC\Delta\omega} = \frac{R}{1 + 2iQ_\mathrm{i}\Delta\omega/\omega_\mathrm{r}}, \end{aligned}$$

where we have defined the detuning angular frequency $\Delta\omega = \omega - \omega_\mathrm{r}$. The reflection coefficient of a 3D cavity is given by:

$$\begin{aligned} S_{11}(f) &= \frac{Z(f) - Z_0}{Z(f) - Z_0} = \frac{R - Z_0\,(1 + 2iQ_\mathrm{i}\Delta f/f_\mathrm{r})}{R + Z_0\,(1 + 2iQ_\mathrm{i}\Delta f/f_\mathrm{r})} \\ &= \frac{Q_\mathrm{i} - Q_\mathrm{e}\,(1 + 2iQ_\mathrm{i}\Delta f/f_\mathrm{r})}{Q_\mathrm{i} + Q_\mathrm{e}\,(1 + 2iQ_\mathrm{i}\Delta f/f_\mathrm{r})}, \end{aligned}$$

where we have introduced the frequency detuning $\Delta f = f - f_\mathrm{r}$. This expression clearly shows that the reflection coefficient of a 3D cavity close to resonance is entirely determined by three parameters, namely Q_i, Q_e and f_r. The magnitude of the frequency response in reflection is a symmetric dip centered at f_r. The internal and external quality factor can be directly obtained by fitting the $S_{11}(f)$ response of the cavity. A 3D cavity can also be measured in transmission and the network parameter $S_{21}(f)$ is given by:

$$\begin{aligned} S_{21}(f) &= \frac{Z(f)}{Z(f) + Z_0} = \frac{R}{R + Z_0 + 2iZ_0 Q_\mathrm{i}\Delta\omega/\omega_\mathrm{r}} \\ &= \frac{Q_\mathrm{i}/(Q_\mathrm{i} + Q_\mathrm{e})}{1 + 2iQ\Delta f/f_\mathrm{r}}. \end{aligned}$$

The magnitude of the transmission coefficient has the form of a Lorentzian peak:

$$|S_{21}(f)|^2 = \frac{Q_\mathrm{i}^2/(Q_\mathrm{i}+Q_\mathrm{e})^2}{1+(2Q\Delta f/f_\mathrm{r})^2},$$

where the loaded quality factor is strictly related to the FWHM of the peak $Q = \omega/\mathrm{FWHM}$.

In the course of this project, several superconducting qubits have been fabricated and characterised inside 3D cavities. In Chapter 5, we shall present dispersive measurements of 3D transmons on quartz and diamond. These qubits consist of two $\approx 250 \times 500\,\mu\mathrm{m}^2$ aluminium pads connected by a Josephson junction. The cavity has a bare frequency of 11.23 GHz and it is measured in transmission. Before placing the chip inside the cavity, the latter is cleaned in an ultrasound bath of acetone for several minutes and rinsed with IPA. The chip is fixed into the slot with four little pieces of indium placed at the four corners of the chip (indium is a very soft and sticky material suitable for this procedure [13]). During this operation, the chip is handled with plastic tweezers and particular care is taken to make sure that the cavity surfaces are not accidently scratched. Once the chip has been inserted inside the cavity, its transmission coefficient is measured and the internal quality factor usually drops from 10^6 to 10^5. These values are high enough for our characterisation purposes.

3.5 Cryogenic microwave setup

In circuit-QAD experiments, the qubit frequency f_{01} and the SAWR frequency can be engineered to be in the range 1 - 7 GHz. In order to initialise the qubit and the cavity in their quantum mechanical ground state and to prevent spontaneous thermal excitations, it is necessary to cool the device down to temperatures satisfying the relation $T \ll hf_{01}/k_\mathrm{B} \approx 100\,\mathrm{mK}$. Furthermore, the readout of the qubit is

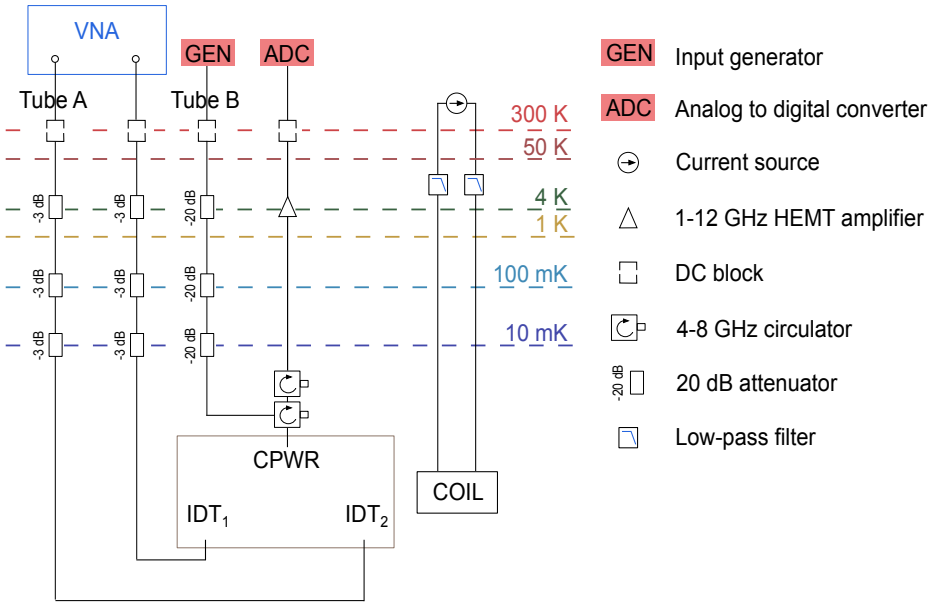

Figure 3.12 | Dilution refrigerator. Schematic of the cryogenic setup for measuring circuit QAD devices.

performed with a CPWR made of aluminium. The quality factor of this resonator becomes significant only when the aluminium becomes superconducting (microwave signals rapidly dissipate in electromagnetic cavities with finite resistance). For these reasons, we have performed our experiments inside a dilution refrigerator with base temperature of $T_{\mathrm{bt}} \approx 10\,\mathrm{mK}$. This temperature is well below the critical temperature of aluminium $T_{\mathrm{c}} \approx 1.2\,\mathrm{K}$ bringing our device in a superconducting state in which resistive dissipations are completely absent.

Dilution refrigerator

The dilution refrigerator used in our laboratory is a Cryofree Triton 200 from Oxford Instruments. The fridge has several circular plates - one on top of the other - mechanically but not thermally connected together. The nominal temperature reached by the bottom plate is $T_{\mathrm{bp}} \approx 10\,\mathrm{mK}$. The cool-down takes place in two steps. A Pulse-Tube cooler cools the stages of the fridge down to 4 K. Exploiting the sponta-

neous phase separation of a He^3 - He^4 mixture in a dilution unit, the bottom plate of the fridge reaches the base temperature T_{bp}. These two steps usually take 36 hours in total. When fully cooled, each stage of the fridge reaches a stable temperature as depicted in Fig. 3.11.

The sample holders containing the superconducting devices are mechanically connected to the bottom plate of the fridge. The devices are measured by sending microwave signals via coaxial cables from room-temperature instrumentation down all the temperature stages of the fridge. The power needed to populate a 2-port SAW resonator with a single phonon is given by (see appendix of reference [14])

$$P_{\mathrm{in}} = \frac{Q_{\mathrm{e}}}{Q^2}\frac{hf_{\mathrm{r}}^2}{2},$$

where $Q = (1/Q_{\mathrm{i}} + 1/Q_{\mathrm{e}})^{-1}$ is the loaded quality factor. Assuming that the external quality factor is $Q_{\mathrm{e}} = 10^4$, the internal one is $Q_{\mathrm{i}} = 10^3$ and the frequency of the resonator is $f_{\mathrm{r}} = 3\,\mathrm{GHz}$, this equation predicts $P_{\mathrm{in}} = 0.03\,\mathrm{fW} \approx -135\,\mathrm{dBm}$. This simple calculation shows that in order to populate the cavity with a single phonon, the input power must be very small. Furthermore, it is necessary to reduce the room temperature noise propagating along the lines. To this end, the microwave cables are connected to a series of attenuators leading to an overall attenuation of $\approx -70\,\mathrm{dB}$. By adjusting the power on the generator, it is possible to populate the cavity with the desired average number of photons.

Microwave lines

Depending on the experiment conducted, the microwave drives are generated at room temperature either with a vector network analyser (VNA) or with a SMF100A signal generator from Rohde & Schwarz. These instruments can send sinusoidal mi-

crowave drives at powers up to[17] 20 dBm and as low as −120 dBm. This wide flexibility permits to set the right source power in order to obtain the desired cavity population. UT85 microwave cables with a 50 Ω impedance are used to carry the microwave signals. These coaxial lines are soldered to SMA connectors from Huber&Suhner. This is a delicate task in which particular care must be taken to ensure that the centre pin is not scratched, residues of solder flux are completely removed, and the dielectric is smoothly cut. After soldering, each cable is tested by measuring its network parameters $S_{ij}(f)$. With a bit of practice, it is possible to fabricate cables with a reflection coefficient from the SMA connectors lower than −20 dB up to 20 GHz. Finally, instruments connected to the fridge via microwave lines can have slightly different grounds and this can lead to undesired 'ground loops'. Hence, DC blocks 8039 from Aeroflex Inmet are installed on top of fridge such as to isolate the cryostat earth from that of the instruments.

Our fridge is equipped with two sets of microwave lines: 8 lines are connected to tube A, whereas 6 lines are connected to tube B. Tube A (tube B) has three 3 dB (20 dBm) attenuators. The overall attenuation of these lines depends slightly on frequency. In the 1 - 5 GHz range where most of our experiments are performed, the overall attenuation of the lines connected to tube B ranges between −64 and −70 dBm. Note that the attenuation also depends on the temperature of the fridge, since the resistance of the coaxial cables varies with temperature.

Tube A lines are not highly attenuated and they allow us to measure devices in reflection without any amplification. However, cavities measured using tube A lines do not reach the ground state due to excessive room-temperature thermal noise propagating down to the base. Lines connected to tube B can be used to probe the SAW

[17] When signals with drive power greater than 0 dBm are used to measure a superconducting device, the base temperature can increase by several millikelvin.

resonators in the quantum regime. In this case however, an appropriate amplification mechanism must be employed to make the the output signal sufficiently large to detect. In the next section, we describe the amplification chain in our experimental setup.

Amplification chain

The weak signal reflected (or transmitted) by the cavity must be filtered and amplified in order to reach a potential difference of $V \approx 0.5\,\mathrm{mV}$ that can be detected by an Analog-to-Digital Converter (ADC). The amplification is performed with several amplifiers in series along the output line. The first one is an HEMT (High Electron Mobility Transistor) amplifier LNF-LNC1-12A from Low Noise Factory suitable for cryogenic environments. The HEMT has a gain of +39 dB in the 1 - 12 GHz and it is placed on the 4 K stage of the fridge (it is not possible to connect it at the bottom plate, since it dissipates too much energy). To further decrease the dissipation of the output line, a special type of superconducting cable with inner and outer conductor made of NbTi carries the signal from the base plate to the 2.7 K stage of the fridge. The HEMT reflects part of the incoming signal. To prevent this reflected signal from reaching the device, a pair of circulators from Raditek Cryo are connected before the HEMT. The circulators are chosen with a specific working frequency range according to the requirements of the measurements. Once the output signal reaches the room temperature cables, it is filtered and amplified by 26 dB with two low-noise amplifiers ZVA-183+ from Mini-Circuits. Down-conversion to 62.5 MHz is performed with an IQ mixer (IQ-0618 from Marki-Microwave) that receives as its input two microwave signals (one coming from the device and another from a local oscillator) and outputs two quadrature signals. Each channel is filtered and amplified by 24 dB with a

low noise amplifier (ZFL-500LN+ from Mini-Circuits) before being detected by an analog to digital converter which is connected to a field-programmable gate array (FPGA, Xilinx Virtex-6 FPGA) board, designed to rapidly read the digitised signal and average it locally.

3.6 Conclusions and possible improvements

In this chapter, we have presented the experimental techniques adopted to fabricate and measure our SAW devices. A significant part of this project was devoted to developing a consistent and reproducible fabrication procedure for SAW devices in the GHz range. There are still some improvements that can be made, the main ones being:

1. In this thesis, we have focused on SAW resonators with shorted aluminium gratings. It would be interesting to compare the performance of these devices with SAW resonators with gratings formed from grooves. In this case, the reflection of the wave does not have an electrical contribution: it is purely mechanical. Groove gratings should lead to an improved frequency stability since the only metal in the active acoustic area comes from the transducer [48, 69].

2. In principle, it would be possible to deposit piezoelectric films on substrates (such as sapphire or diamond) only on specific areas of the chip. In this way, electrical components not used for transduction (such as CPWRs and qubits) can be fabricated on the non-piezoelectric parts of the device, potentially enabling better quality factors of the electromagnetic cavity, and coherence times of qubits.

3. In circuit-QAD devices, SAW resonators and Josephson junctions were fabricated in a single evaporation step. This meant that the fingers in the IDTs could not be less than 700 nm wide (with a 600 nm copolymer + PMMA layer, it is almost im-

possible to fabricate smaller features). Another way to fabricate these devices would be to pattern the SAW resonators and qubit capacitance first. In a second evaporation step, ion milling could, in principle, remove the oxide layer on top of the qubit interdigitated structure. The Josephson junction could then be built with the usual double angle evaporation technique with the aluminium making a good electrical contact with the interdigitated capacitance of the qubit. In this way, it would be possible to fabricate the qubit and the SAW resonator with features smaller than 700 nm and resonance frequencies of 4 GHz.

4. Fabricating Josephson junctions with reproducible resistances can be a challenging problem. In this project, we adjusted the resistance of the junctions by varying the oxidation time. Ideally, it would be better to saturate the oxidation time and pressure and adjust the junction resistance by varying its area. This can be done with bridge-free techniques [46] and would probably lead to more controllable resistance values.

Chapter 4

SAW resonators in the quantum regime

Fortunately, the acoustic propagation loss strongly decreases at low temperatures.

In this chapter, we present systematic measurements of SAW resonators at or close to the quantum regime, paying particular attention to the various loss contributions that limit their performance. We demonstrate that 0.5 GHz SAW resonators can reach internal quality factors of the order of 0.5 million. We also present measurements of SAW resonators with working frequencies in the range 2 - 4 GHz, that suggest a polynomial dependence of propagation loss on frequency. Finally, we measure the frequency response of a high-frequency device as a function of input power, showing evidence of a weak power dependence of its internal quality factor consistent with coupling to a bath of two level systems. We conclude this chapter with time-domain measurements of SAW resonators.

4.1 SAW resonator loss mechanisms

This chapter is devoted to the investigation of the main loss mechanisms of SAW resonators at low temperatures. A thorough investigation of their performance at

room temperature has already been addressed elsewhere [9, 69] (the terminology used in the following is mainly taken from these references). The performance of a SAW resonator can be quantified in terms of a figure of merit called quality factor defined as:

$$Q = 2\pi f_{\mathrm{m}} \frac{U}{P}, \tag{4.1}$$

where f_{m} is the cavity frequency, U is the stored energy and P is the power lost per cycle, which is affected by several loss mechanisms such as the finite grating reflectivity P_{g}, diffraction losses P_{d}, conversion of surface acoustic waves into bulk modes P_{b}, material losses P_{m}, the resistivity of the electrodes P_{r}, coupling to two-level fluctuators P_{TL}, and coupling to external measurement ports P_{e}. Taking into account these contributions and assuming that they are independent from one another, the quality factor can be written in the following form:

$$Q = 2\pi f_{\mathrm{m}} \frac{U}{(P_{\mathrm{g}} + P_{\mathrm{d}} + P_{\mathrm{b}} + P_{\mathrm{m}} + P_{\mathrm{r}} + P_{\mathrm{TL}}) + P_{\mathrm{e}}}. \tag{4.2}$$

This parameter can be split into two parts, one concerning the intrinsic losses Q_{i} and one due to the external circuitry coupled to the cavity Q_{e}:

$$\frac{1}{Q} = \frac{1}{Q_{\mathrm{i}}} + \frac{1}{Q_{\mathrm{e}}},$$

where the internal and external quality factors are defined as:

$$\begin{aligned} \frac{1}{Q_{\mathrm{i}}} &= \frac{P_{\mathrm{g}} + P_{\mathrm{d}} + P_{\mathrm{b}} + P_{\mathrm{m}} + P_{\mathrm{r}} + P_{\mathrm{TL}}}{2\pi f_{\mathrm{m}} U} = \frac{1}{Q_{\mathrm{g}}} + \frac{1}{Q_{\mathrm{b}}} + \frac{1}{Q_{\mathrm{b}}} + \frac{1}{Q_{\mathrm{m}}} + \frac{1}{Q_{\mathrm{r}}} + \frac{1}{Q_{\mathrm{TL}}} \\ \frac{1}{Q_{\mathrm{e}}} &= \frac{P_{\mathrm{e}}}{2\pi f_{\mathrm{m}} U}. \end{aligned}$$

The inverse of the quality factor can be thought of as a sum of loss rates. When a loss rate is much larger than the others, this loss mechanism will prevail and limit the overall device performance.

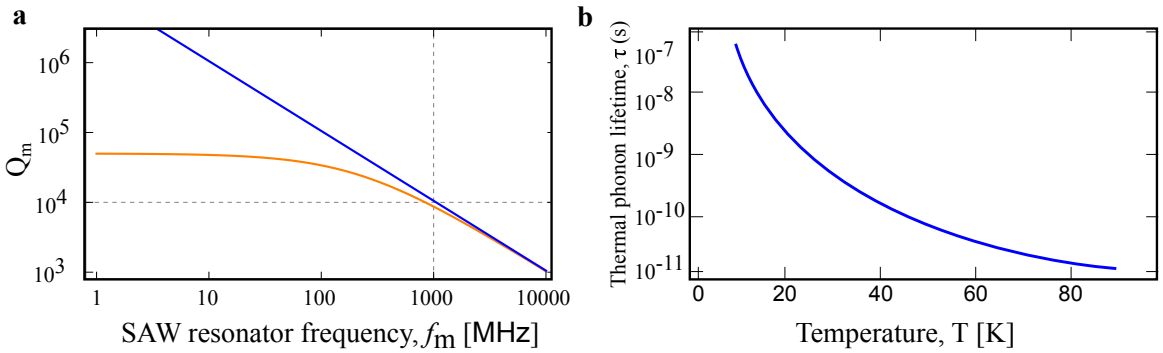

Figure 4.1 | Material quality factor and phonon lifetime a, Room temperature material quality factor Q_m as a function of cavity frequency (orange curve) based on equation (4.5). The blue curve corresponds to the vacuum condition. The gray dashed lines highlight the fact that the internal quality factor of a SAWR is approximately 10 000 at 1 GHz (figure readapted from [9]). **b**, Thermal phonon lifetime as a function of temperature for quartz (readapted from [54]).

Material quality factor Q_m

At room temperature, the internal quality factor of a SAW resonator is strongly limited by the material quality factor Q_m:

$$Q_\mathrm{m} = \frac{\pi f_\mathrm{m}}{v\alpha} \tag{4.3}$$

where v is the speed of the Rayleigh wave and α is the acoustic attenuation given by:

$$\alpha(p,T) = \alpha_\mathrm{air}(p) f_\mathrm{m} + \alpha_\mathrm{prop}(T) f_\mathrm{m}^2 \ , \tag{4.4}$$

where $\alpha_\mathrm{air}(p)$ is a pressure dependent acoustic attenuation due to air loading, and $\alpha_\mathrm{prop}(T)$ is a temperature dependent acoustic damping mainly due to scattering with thermal phonons. For ST-X quartz, equation (4.3) takes the numerical form [9]:

$$Q_\mathrm{m} \approx \frac{1}{2\times 10^{-5} + 9.5\times 10^{-5} f_\mathrm{m}}. \tag{4.5}$$

Note that under vacuum conditions, the product between the internal quality factor and the device frequency is a constant usually referred to as the Qf product. A graph of equation (4.5) for ST-X quartz is shown in Fig. 4.1a. From this plot, we can conclude that at room temperature the material quality factor of a 1 GHz

SAW resonator is approximately 10 000 and it can hardly exceed this value even with optimised engineering of the device.

Fortunately, the acoustic propagation loss $\alpha_{\text{prop}}(T)$, which originates from the interaction between surface acoustic waves and thermal phonons, strongly decreases at low temperatures. Assuming that the temperature satisfies $T \gg hf_{\text{m}}/k_{\text{B}}$ and that the thermal phonon lifetime τ satisfies $2\pi f_{\text{m}}\tau \gg 1$, according to the Landau-Rumer theory the acoustic loss is proportional to [55]:

$$\alpha_{\text{prop}}(T) \propto fT^4. \tag{4.6}$$

Figure 4.1b shows the thermal phonon lifetime as a function of temperature for quartz [54]. From this graph, we can conclude that for 150 MHz surface acoustic waves, the condition $2\pi f_{\text{m}}\tau \gg 1$ is established below 40 K. At these temperatures, it has been observed that the propagation loss decreases in agreement with equation (4.6) [81, 36].

If the temperature decreases even more, the quantum limit $T \ll hf_{\text{m}}/k_{\text{B}}$ can be reached. In this regime, the frequency of the surface wave is higher than the average phonon frequency $f_{\text{ph}} = k_{\text{B}}T/h$ and scattering processes are highly suppressed. The main decay channel of surface waves becomes spontaneous emission into vacuum. This process has been studied by Sakuma and Nakayama [80] and their calculations indicate that in this regime the propagation loss is proportional to:

$$\alpha_{\text{prop}}(T) \propto f^3T^2. \tag{4.7}$$

In the following sections, we will show that our devices exhibit this dependence on frequency. Equation (4.7) also predicts a polynomial temperature dependence. This dependence might be over-shadowed by other loss contributions with a similar polynomial behaviour (such as coupling to a bath of TLS, see section 4.1). These arguments

indicate that at low temperatures the propagation loss is strongly suppressed and other loss mechanisms come into play.

Diffraction losses

An interdigitated transducer emits surface acoustic waves in opposite directions and the wave packets are well collimated when the aperture of the transducer W is much greater than the wavelength of the Rayleigh wave, $W \gg \lambda$. On the other hand, when the transducer aperture is quite small such that $W \approx \lambda$, the IDT behaves like a point-like source emitting surface waves in all directions. Part of these waves will not impinge against the gratings and will leave the cavity. The quality factor Q_{d} takes into account this diffraction phenomenon. Its analytical expression is given by [48]:

$$Q_{\mathrm{d}} = \frac{5\pi}{|1+\gamma|}\left(\frac{W}{\lambda}\right)^2, \tag{4.8}$$

where γ is a material parameter. For ST-X quartz, $\gamma = 0.378$ [85] at room temperature. Assuming that $W = 100\lambda$, we find $Q_{\mathrm{d}} \approx 110\,000$. The diffraction quality factor can be increased by widening the aperture of the cavity W.

Finite grating reflectivity

SAW resonators can be regarded as the acoustic equivalent of Fabry-Perot optical cavities. The two mirrors reflect most of the incident waves, but part of these oscillations escapes through these imperfect reflectors. The quality factor Q_{g} takes into account the finite grating reflectivity and its analytical expression is given by:

$$Q_{\mathrm{g}} = \frac{\pi L_{\mathrm{c}}}{\lambda_0\left[1-\tanh\left(|r_s|N_{\mathrm{g}}\right)\right]}, \tag{4.9}$$

where L_{c} is the longitudinal cavity length, r_s is the reflectivity of each finger in the grating and N_{g} is the number of fingers in the grating. For typical values $\lambda_0 = 1\,\mu$m, $L_{\mathrm{c}} = 100\,\lambda_0$, $|r_s| = 0.002$ and $N_{\mathrm{g}} = 1000$, we have $Q_{\mathrm{g}} \approx 9\,000$.

There are three main approaches to reducing the internal losses due to the gratings. Increasing the cavity length is a good strategy that linearly improves Q_{g}. It must be noted, however, that as the cavity length increases, the device might show several longitudinal resonances and turn into a multimode device. Depending on the application, sometimes it is necessary to work with single-mode resonators. In such a case, the cavity length must be kept contained and therefore increasing the distance between the two mirrors is not a viable option. The second main approach is to increase the reflectivity $|r_s|$ of each finger in the grating. This can be done by increasing the height of the deposited metal. Finally, the number of fingers in the gratings N_{g} must be kept high. We have measured the internal quality factor of 500 MHz SAW resonators as a function of N_{g}. We have observed a saturation of the internal quality factor when N_{g} was approaching the value of ≈ 800 fingers. For this reason, all of the devices characterised in the following sections have $N_{\mathrm{g}} = 1000$ fingers in each grating.

Two-level systems

In the 1950's, measurements of the heat capacity, thermal conductivity and variation of sound velocity in glasses at low temperatures showed a very different behaviour from crystals [70]. For example, almost without exception the specific heat of an arbitrary insulating amorphous solid well below 1K is approximately linear in T and the thermal conductivity is approximately quadratic in T. This result was unexpected since it was believed that low temperature properties of solids were mainly governed by thermal phonons with average frequency much higher than than the acoustic wave frequency. In this picture, acoustic waves propagate through an elastic continuum and they are not sensitive to the microscopic structure of the medium; this would imply that the acoustic propagation should not significantly differ between glasses

and crystals.

Several models have been proposed to account for this unexpected behaviour in amorphous materials [39]. The most successful model is the one proposed by Anderson [3] and Phillips [70], which predicts the thermal and acoustic anomalies of glasses at low temperatures and is based on the existence of two-level systems (TLSs) in the medium. These two-level fluctuators consist in atoms tunnelling between two configurational states giving rise to very small energy splittings in the order of $10^{-5}\,\mathrm{eV} \approx h \times 10\,\mathrm{GHz}$. They are generally visualised as an ion or electron that can tunnel between two spatial quantum states and their density is much lower in crystals than in glasses. These fluctuators occur due to either defects in the crystal structure or the presence of polar impurities such as OH^-.

TLSs have a strong influence on the propagation of sound waves. At low temperatures, the most probable interaction between a phonon and a TLS is an absorption followed by an emission of another phonon due to the TLS relaxation. This mechanism for the absorption of sound also explains the power dependence of the acoustic attenuation: with increasing acoustic power, the upper level becomes more and more populated; therefore, the number of effective TLSs decreases an, with it, the overall absorption. Finally, the absorption also depends on the number of TLSs taking part in the resonant absorption process at a given frequency.

The theory underlying the interaction between the acoustic wave and TLSs can be found in references [70] and [39]. Here, we limit ourselves to report the analytical expression of the loss rate caused by a TLS bath interacting with an acoustic wave:

$$\alpha_{\mathrm{TLS}}(P,T) = F(\vec{x})\,\frac{2\pi^2 f_{\mathrm{m}} n_0 \gamma^2}{\rho v^2}\tanh\left(\frac{h f_{\mathrm{m}}}{2k_{\mathrm{B}}T}\right)\left(1+\frac{P}{P_{\mathrm{c}}}\right)^{-0.5}, \tag{4.10}$$

where n_0 is the density of states of the TLS, ρ is the density of the crystal, P_{c} is a critical power, γ describes the strength of the coupling between the TLS and

the phonons and $F(\vec{x})$ is a filling factor. Equation (4.10) has a pronounced power dependence and a linear temperature dependence when $hf_{\mathrm{m}} \approx k_{\mathrm{B}}T$. The internal quality factor Q_{TLS} is related to α_{TLS} by:

$$Q_{\mathrm{TLS}}(P,T) = \frac{\pi f_{\mathrm{m}}}{v\alpha_{\mathrm{TLS}}(P,T)}. \tag{4.11}$$

In Section 4.3 we present measurements that support the hypothesis of a coupling between surface acoustic waves and TLSs in the low power and temperature regimes.

Bulk mode conversion

Another mechanism that affects the performance of SAW resonators is bulk mode conversion. This process consists of the conversion of surface waves into bulk modes either during transduction or when SAWs impinge against the gratings. Bulk mode conversion can be observed from time-domain measurements of SAW delay lines. The electrical signal is converted by the first IDT into SAWs and bulk waves. The latter might then bounce against the back of the chip and reach the second IDT. Since bulk waves travel a longer distance between the two IDTS, they reach the second IDT after a longer time. In the time domain, the detection of bulk waves results in a transmission peak captured a bit later than the SAW transit signal. In order to suppress this spurious response, it is recommended to roughen the back of the chip. In this way, the reflected bulk waves are randomly scattered.

4.2 Characterisation of SAW resonators

Introduction

In this section, we investigate the quality factors of SAW resonators measured inside a dilution refrigerator in high vacuum and at temperature of $T \approx 10\,\mathrm{mK}$ (see Fig. 4.2), under which conditions the dissipation of the SAW is very low. We work

with the common SAW substrate ST-X quartz due to its known good performance in resonators at room temperature and weak piezoelectric coupling [62], which results in SAWs with little electrical character and hence good prospects for being weakly electrically coupled to environmental sources of dissipation. The reflectors and IDTs are in all cases made from superconducting aluminium such that at 10 mK ohmic losses can be neglected. The resonators were characterized by measuring the complex reflection coefficient $S_{11}(f)$ at the IDT using a vector network analyzer (VNA) (see Fig. 4.2a). Using an RLC equivalent circuit model, one can derive the following expression for the reflection coefficient close to a single resonance

$$S_{11}(f) = \frac{(Q_e - Q_i)/Q_e + 2iQ_i(f - f_m)/f}{(Q_e + Q_i)/Q_e + 2iQ_i(f - f_m)/f}. \tag{4.12}$$

Here Q_i is the internal Q-factor of the mode and Q_e is the external Q-factor due to the presence of the IDT and measurement port.

The measured single-port SAW resonators can be characterized by a set of geometric parameters illustrated in Fig. 4.2a and listed in Table 4.1. The devices have a frequency response centered at $f_m = v/\lambda_0$, where $v \approx 3100\,\mathrm{m/s}$ is the SAW velocity and $a = \lambda_0/4$ is the electrode and space width in the lithographically defined mirrors and IDT. The mirrors are separated by an integer number of half wavelengths $d = m\lambda_0/2$ and their reflectivity is given by $R = \tanh(N_g|r_s|) \approx 1$ in the limit $N_g|r_s| \gg 1$, where N_g is the number of electrodes in the mirror and r_s is the reflectivity of each electrode.

Preliminary measurements of 500 MHz devices

We have initially performed a comprehensive study of SAW resonators at a wavelength of $\lambda_0 = 6\,\mu\mathrm{m}$ ($f_m \approx 523\,\mathrm{MHz}$) to determine how Q_e and Q_i depend on transducer and grating geometry. This frequency was chosen for compatibility with stan-

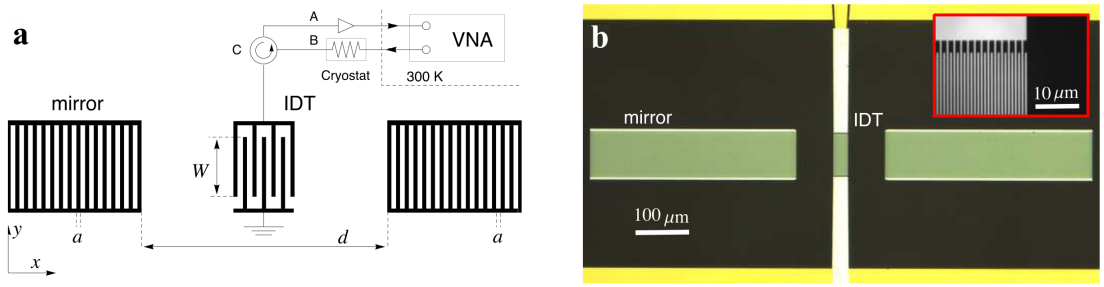

Figure 4.2 | Equivalent circuit and device optical image. **a**, Schematic of a 1-port SAW resonator connected to the measurement setup (A: cryogenic amplifier, B: cold attenuators, C: circulator, and VNA: Vector Network Analyzer). **b**, Optical microscope image of a SAW resonator (device r_3, see Table 4.1). Inset: magnification of the IDT electrodes of a similar device (q_1).

dard photolithography for which the feature sizes of $a = 1.5\,\mu$m are achievable and a large number of devices could be fabricated on a single wafer. In this initial investigation we determined that, in accordance with SAW theory [5], the external quality factor follows[1] $Q_\mathrm{e} \propto L_\mathrm{c}/N_\mathrm{t}^2$ and the internal quality factors were limited by grating reflectivity, following

$$Q_\mathrm{g} = \frac{\pi\,(d + 2L_\mathrm{p})}{\lambda_0\,[1 - \tanh\,(|r_\mathrm{s}|N_\mathrm{g})]}. \tag{4.13}$$

Based on these observations, we designed a device to realise a high Q_i (within the confines of our chip geometry) with widely spaced long gratings (device p_1 see Table 4.1). For this device, $Q_\mathrm{e} = 1.16 \times 10^5$, $Q_\mathrm{i} = 4.53 \times 10^5$ and the frequency response is shown in Fig. 4.3a. Note that this measurement is not in the quantum regime since $k_\mathrm{B}T \approx hf_\mathrm{m}$.

In order to investigate individual loss contributions, we have fabricated several SAW resonators with a fixed design and only one geometrical parameter was varied at a time. In the following sections, we describe how the internal quality factor of SAWRs depend on their geometry.

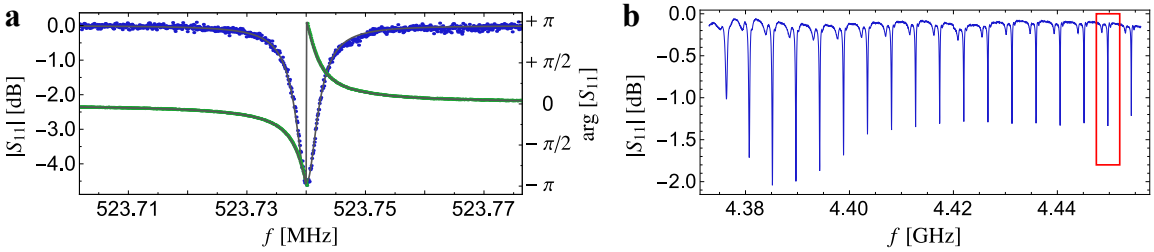

Figure 4.3 | Measured reflection coefficient. **a**, Magnitude (blue) and phase (green) of the measured reflection coefficient $S_{11}(f)$ of the SAW resonator p_1. Solid lines are a fit to equation (6.2). **b**, Frequency response of device q_7 showing 18 supported high Q modes. The solid red box indicates the resonant mode measured in Fig. 4.5. A background due to the measurement setup has been subtracted in both **a** and **b**.

High frequency SAW resonators

In this section, we present measurements of SAW resonators at higher frequencies, fabricated using electron beam lithography. In Fig. 4.4a we plot Q_i for a series of resonators with $\lambda_0 = 1.0\ \mu\mathrm{m}$ ($f_\mathrm{m} \approx 3.1\,\mathrm{GHz}$), for which the distance between the two gratings d was varied over the range $0.05-1.8\,\mathrm{mm}$ with all other geometric parameters fixed (see Table 4.1). The number of modes seen increases from 1 for device r_1 to 65 for device r_{10}. For devices with more than 5 modes ($r_5 - r_{10}$), we took the average Q_i for the 5 modes at the center of the grating stopband where the reflectivity is highest. We expect Q_i to be dominated by the grating reflectivity at low d and saturate at high d due to propagation losses. The data follow this trend and can be fitted with the following relation

$$Q_\mathrm{i} = \left(\frac{1}{Q_\mathrm{g}} + \frac{v\,\alpha_\mathrm{p}}{\pi f_\mathrm{m}} \right)^{-1}. \tag{4.14}$$

From a fit to equation (4.14), we determine the electrode reflectivity to be $|r_\mathrm{s}| = 0.002$, and we can place an upper limit on the propagation loss at 3.1 GHz of $\alpha_\mathrm{p}|_{10\,\mathrm{mK}} < 0.015\,\mathrm{mm}^{-1}$ corresponding to a phonon mean free path of $l = 1/\alpha_\mathrm{p} \approx 6\,\mathrm{cm}$.

We then moved on to investigate the frequency dependence of Q_i, using a device geometry with large $d = 1929\lambda_0/2$, over the range $2.0 - 4.4\,\mathrm{GHz}$ (devices $q_1 - q_7$,

[1]Here, N_t is the number of fingers in the transducer.

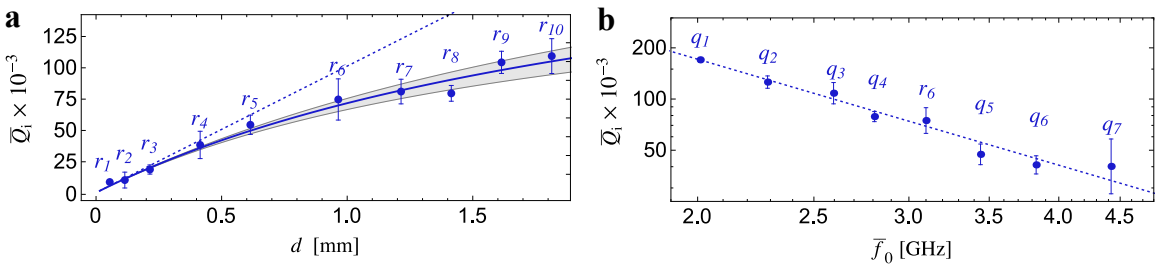

Figure 4.4 | Quality factor vs distance and resonance frequency. **a**, $\overline{Q}_\mathrm{i}$ versus d for devices $r_1 - r_{10}$. Solid line is a fit to equation (5.3). Shaded area indicates one standard deviation of α_p and the dashed line is the linear part of this fit ($\alpha_p = 0$). **b**, $\overline{Q}_\mathrm{i}$ versus $\overline{f}_\mathrm{m}$ for devices $q_1 - q_7$ and r_6. Dashed line is a fit to $\overline{Q}_\mathrm{i} = c_1 f^{-c_2}$.

see Table 4.1). These long devices all display around 20 resonant modes within the stopband of the reflectors (see Fig. 4.3b for the frequency response of device q_7). In Fig. 4.4b we plot the dependence of the average internal quality factor $\overline{Q}_\mathrm{i}$ of all modes of each device against average mode frequency $\bar{f}_\mathrm{m}$. Error bars represent the standard deviation of Q_i from the set of resonant modes. The quality factor is seen to decrease with frequency, and the linear trend observed on a log-log scale indicates a polynomial dependence. We fit the data to $\bar{Q}_\mathrm{i} = \pi f / v\alpha_\mathrm{p} = c_1 f^{-c_2}$ and find $c_1 = 719 \pm 85$, $c_2 = 2.07 \pm 0.13$. This strongly suggests $\alpha_\mathrm{prop} \propto f^3$, agreeing with a model developed for SAW propagation loss in the high-frequency and low-temperature limits [80].

4.3 Low power measurements

In this section, we present measurements of the internal quality factor of one of the modes of device q_7 ($f_\mathrm{m} = 4.449\,\mathrm{GHz}$) at low drive powers such that the average resonator phonon population reaches the regime $\overline{n} \ll 1$. Figure 4.5 shows the dependence of Q_i on drive power P. In this case, the VNA was connected to device q_7 through highly attenuated microwave lines with an overall attenuation from the instrument to the sample of $-67 \pm 1\,\mathrm{dB}$. This allows us to calculate the average phonon population $\overline{n}$ resulting from the coherent drive, shown in the upper scale of Fig. 4.5. This is an

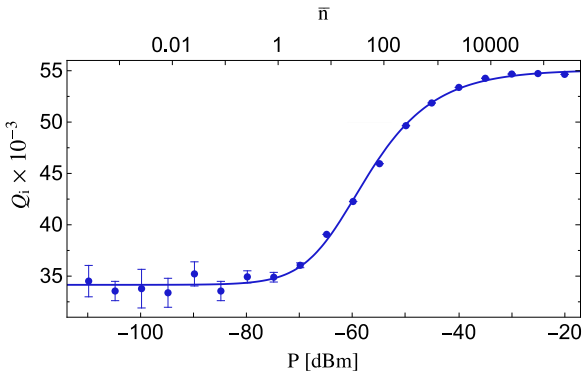

Figure 4.5 | Quality factor vs drive power. Q_i versus drive power P for the resonant mode $f_\mathrm{m} = 4.449\,\mathrm{GHz}$ of device q_7. Solid line: fit to $Q_\mathrm{i} = \left(v\,\alpha_\mathrm{TLS}/\left(\pi f_\mathrm{m}\right) + 1/Q_\mathrm{rl}\right)^{-1}$; $\overline{n}$ is the mean number of phonons occupying the resonator due to the coherent drive P.

accurate estimate of the average coherent (non-thermal) phonon occupation due to the continuous drive. A clear reduction in Q_i is observed as P is reduced, saturating at low power at a value of $Q_\mathrm{i0} = 34500$. A similar dependence has been observed in bulk mechanical resonators [32, 28] and electromagnetic coplanar waveguide resonators (CPWR) [49] at low temperature, and has been attributed to coupling to a bath of two level systems (TLS). The analytical expression of the loss rate caused by a TLS bath is given by equation (4.10). The internal quality factor is related to α_TLS by $Q_\mathrm{i} = \left(v\,\alpha_\mathrm{TLS}/\pi f_\mathrm{m} + 1/Q_\mathrm{rl}\right)^{-1}$, where Q_rl takes into account remaining losses. We find that our data fits to this expression well with $P_\mathrm{c} = -65.7\,\mathrm{dBm}$ and $Fn_0\gamma^2 = 4.5 \times 10^4\,\mathrm{J/m^3}$. In order to completely validate this model and to estimate the value of the filling factor $F(\vec{x})$, a temperature dependent measurement is required [49, 29]. The ratio $Q_\mathrm{i0}/Q_\mathrm{rl} \approx 0.6$ is much higher than typically seen in CPWRs [59], indicating that any TLS contribution to the loss is considerably less in the SAW case. Such a difference is qualitatively in agreement with an electric field coupling to the TLS bath, since in a weak piezoelectric such as quartz, only a small fraction of the SAW energy is electrical.

4.4 Time domain measurements

We conclude this chapter by presenting time-domain measurements of 1-port SAW resonators. These acoustic devices can be probed with pulses of variable length between a few nanoseconds up to the cavity round trip $\Delta = L_c/v$. The electric pulse is converted by the IDT into wave packets that bounce against the gratings and are eventually collected by the IDT.

The time response of a 1-port SAWR can be described with an heuristic model which takes into account the shape of the applied pulse and the IDT response. In our case, the applied electrical signal has a square modulation of the form

$$s(t) \approx \frac{1}{1 + [a(t - t_0)]^b}, \tag{4.15}$$

where t_0 takes into account a possible time offset and the parameters a, b describe the length and the rise time of the pulse, respectively. The time-domain response is a sum of square pulses delayed by $\Delta = L_c/v$ and modulated by an exponential decay:

$$S_{11}(t) = A \sum_{n=1}^{\infty} s(t - n\Delta) e^{-c\left\lceil \frac{t - t_0 - \Delta/2}{\Delta} \right\rceil} = A \sum_{n=1}^{\infty} \frac{e^{-c\left\lceil \frac{t - t_0 - \Delta/2}{\Delta} \right\rceil}}{1 + [a(t - t_0 - n\Delta)]^b}, \tag{4.16}$$

where A is a scaling factor and c is a decay constant. Figures 4.6a-c show the time-domain response of a 2.8 GHz SAW resonator when probed with pulses of variable length. A decaying train of pulses is clearly observed, consistent with the applied pulse reflecting back and forth between the mirrors of the cavity. As the length of the applied pulse increases, the peaks become broader and they eventually merge with each other when the pulse length is comparable to the cavity round trip $\Delta \approx 330$ ns.

SAWRs can be probed with arbitrary train of pulses. Figure 4.6d shows the time-domain response of a SAWR when probed with two 10 ns pulses separated by 150 ns $\approx \Delta/2$. In this case, the number of peaks per time interval is doubled with respect to

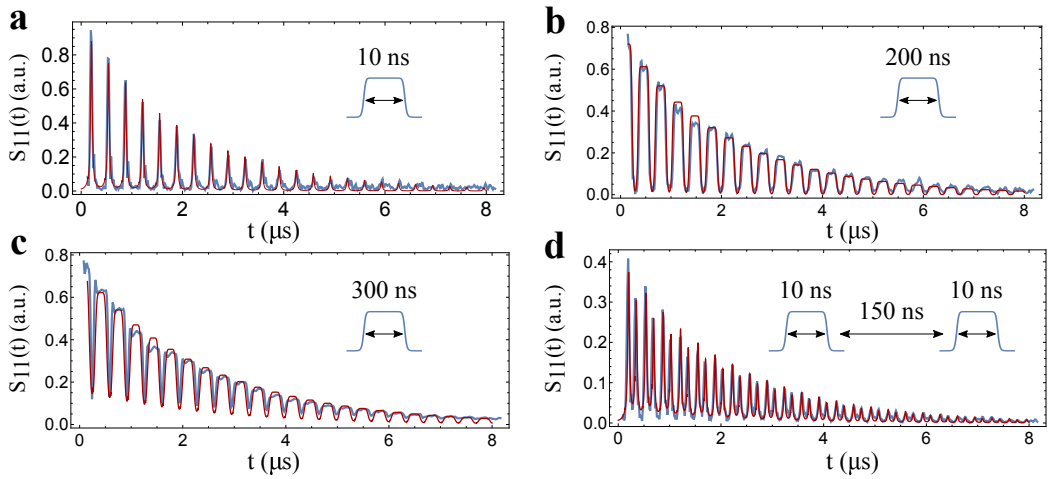

Figure 4.6 | Time-domain measurements. **a**, Time-domain response of a 1-port SAW resonator close to resonance probed with a 10 ns electric square pulse (blue points). The red curve is a fit to equation (4.16). **b**, **c**, Same measurement with pulses of 200 ns and 300 ns, respectively. **d** Time-response of a SAW resonator when probed with two 10 ns pulses separated by $L_c/2v \approx 150$ ns. The insets in these four panels schematically show the envelope of the applied pulses.

the other time-domain measurements. Unlike CPWRs, these acoustic cavities offer the possibility to manipulate the cavity population in the time-domain due to the slow speed of the sound waves. For instance, it would be possible to fabricate a device with several SAW resonators each containing a qubit. The information related to the qubit state can in principle be transferred from one qubit to another by means of surface waves. While the wave is still travelling between the two qubits, it would possible to change the state of the receiving qubit. This and more advanced schemes could be implemented by exploiting the slow speed of sound in these piezoelectric substrates.

4.5 Conclusions and further improvements

In this chapter we have presented low temperature measurements of Fabri-Perot acoustic cavities based on surface acoustic waves. The focus has been the investigation of the main loss mechanisms and the performance of these devices as a function of

geometric parameters. We measured a SAW resonator with internal quality factor approaching 0.5 million at 500 MHz. We have observed that the internal quality factor of SAW resonators increases as the cavity length increases. Furthermore, the internal Q of these devices decreases polynomially as a function of the resonance frequency in accordance with theory. Finally, we have measured the internal Q factor of a 4 GHz resonator as a function of input power and the observed dependence is consistent with a model based on coupling to a bath of two level systems. This characterisation of SAW resonators at low temperature strongly suggests that these acoustic devices can be exploited in circuit quantum acoustodynamic architectures.

Some improvements can still be implemented:

1. The SAW resonators investigated in this thesis are 1-port resonators measured in reflection. It would be interesting to fully characterise 2-port SAW resonators with input/output IDTs placed outside the SAW cavity (in analogy with optical cavities). Placing the IDTs outside the cavity would probably increase the internal quality factor of the device (the transducer in the middle of 1-port SAWRs partly contributes to energy losses and undesired reflections). However, this configuration would inevitably lead to a strong correlation between the external and internal quality factor of the resonator (they would both depend on the number of fingers in the gratings).

2. It would be interesting to measure several SAW resonators fabricated with other materials, such as gold, niobium or titanium nitride, and compare these results with resonators made of aluminium. For example, gold is expected to introduce more losses due to its finite resistivity at base temperature. On the other hand, niobium and titanium nitride have a higher critical temperature with respect to aluminium and with these materials it would be possible to distinguish several temperature dependent loss mechanisms, such as coupling to two-level systems and the creation

of quasi particles in the superconductor.

3. The circuit-QAD experiment presented in Chapter 6 has been performed with a qubit embedded in a two-port SAW resonator. As discussed in Chapter 6, we believe that the response of a 2-port resonator is partially affected by the presence of the qubit in the middle of the cavity. This hypothesis could be validated by fabricating and measuring a two-port resonator with the same geometry but without the qubit.

Table 4.1 | Device parameters. Parameters of the measured SAW resonators. For device p_1, the thickness of the aluminum layer is $h = 100\,\mathrm{nm}$ and the geometric parameters are $W = 600a$, $N_t = 51$ and $N_g = 1500$; for all other devices $h = 30\,\mathrm{nm}$, $W = 400a$, $N_t = 71$ and $N_g = 1000$.

Device	a [nm]	$\overline{f}_\mathrm{m}$ [GHz]	$d/2a$	$\overline{Q}_\mathrm{e}/10^3$	$\overline{Q}_\mathrm{i}/10^3$	$\overline{Q}_\mathrm{i}\overline{f}_\mathrm{m}/10^{14}$
p_1	1500	0.52	1051	116	453	2.36
r_1	250	3.11	109	24	8.8	0.27
r_2	250	3.12	229	18	10.4	0.32
r_3	250	3.11	429	98	18.8	0.62
r_4	250	3.11	829	167	38.4	1.19
r_5	250	3.10	1229	363	54.5	1.74
r_6	250	3.09	1929	657	74.7	2.32
r_7	250	3.09	2429	473	81.0	2.52
r_8	250	3.10	2829	843	79.6	2.45
r_9	250	3.11	3229	1230	103	3.18
r_{10}	250	3.08	3629	927	109	3.23
q_1	390	2.01	1929	242	171	3.43
q_2	340	2.29	1929	499	126	2.88
q_3	300	2.60	1929	174	108	2.81
q_4	275	2.81	1929	232	78.8	2.21
q_5	225	3.44	1929	445	47.3	1.63
q_6	200	3.83	1929	358	41.0	1.57
q_7	175	4.42	1929	528	40.2	1.78

Chapter 5

Superconducting qubits on quartz and diamond

Circuit quantum electrodynamics deals with the interaction between light and matter on a chip.

This chapter presents the characterisation of superconducting qubits on quartz and diamond, two key materials in the field of circuit QAD. This investigation has been performed by embedding a transmon in a 3D aluminium cavity employed to excite and read out the state of the qubit. We first show how the dispersive interaction between the transmon and the cavity can be used to perform qubit spectroscopy. We then present Rabi and Ramsey experiments to extract the coherence time of our qubits.

5.1 Resonator spectroscopy

A systematic characterisation of a superconducting qubit dispersively coupled to an electromagnetic resonator starts with a measurement of the transmission coefficient of the cavity. Figure 5.1a shows the transmission coefficient of our 3D aluminium cavity at base temperature measured at low powers. From this measurement we can directly extract the qubit population. The qubit-state dependent transmission

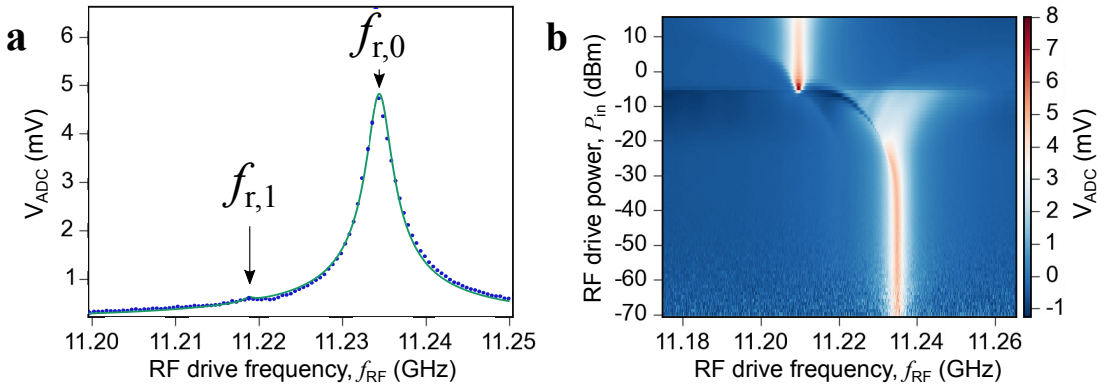

Figure 5.1 | 3D cavity transmission coefficient. **a**, Measured transmission coefficient $|S_{21}(f)|$ of a 3D cavity at base temperature (blue points). The green curve is a fit to equation (5.1) with fit parameters $f_{r,0} = 11.234$, $Q = 3660$ and $p_e/p_g = 0.019$. **b**, Same measurement as a function of RF drive power.

coefficient of the 3D cavity can be written in the form:

$$S_{21}^{j}(f) = \frac{p_j}{1 + 2iQ_j(f - f_{r,j})/f_{r,j}},$$

where j labels the qubit states $j = 0, 1, 2, \ldots$ and the variable p_j is related to the population of state j. If the qubit is found in several states in average, the transmission coefficient can be written as a sum of terms:

$$S_{21}(f) = \sum_j S_{21}^{j}(f). \tag{5.1}$$

This behaviour can be easily recognised in Fig. 5.1a, where one main resonance is visible at $f_{r,0} = 11.234\,\text{GHz}$ and another one is present at $f_{r,1} = 11.219\,\text{GHz}$. By fitting this frequency response with equation (5.1), we extract the ratio between the excited and ground state populations $p_e/p_g \approx 0.019$. This ratio can be exploited to find the effective temperature T_q of our superconducting qubit by using the formula:

$$\frac{p_e}{p_g} \approx \exp\left(-\frac{\hbar\omega_{01}}{k_B T_q}\right).$$

From this calculation, we find $T_q \approx 110\,\text{mK}$. This value is higher than the base temperature of our dilution refrigerator $T_{bt} \approx 10\,\text{mK}$. This is probably due to the

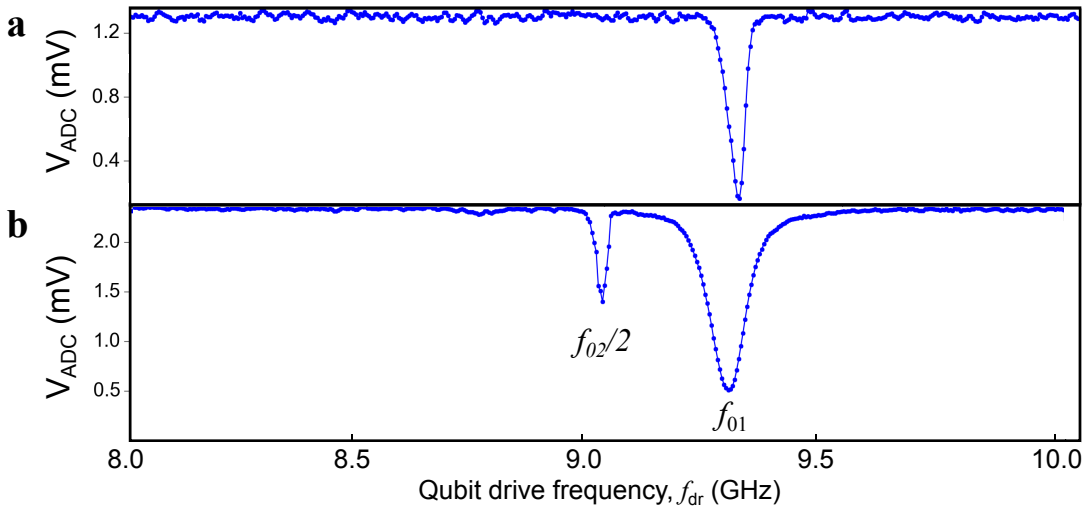

Figure 5.2 | Qubit spectroscopy. **a**, Qubit spectroscopy of a 3D quartz transmon. The graph shows the voltage difference detected by the acquisition card as a function of qubit drive frequency. The dip at 9.29 GHz corresponds to the first qubit transition f_{01}. **b**, Qubit spectroscopy at high qubit drive power. Two dips are clearly visible at 9.29 GHz and 9.05 GHz. They correspond to the transitions f_{01} and $f_{02}/2$, respectively. Note that the linewidth of the $f_{02}/2$ transition is narrower than the linewidth of the f_{01} transition because it originates from a two photon process.

fact that the sample is not perfectly thermalised. In addition, thermal noise coming from the coaxial cables might increase the effective temperature of our qubit.

Figure 5.1b illustrates the power dependence of the cavity response. This measurement clearly shows that at relatively high powers, the bare cavity resonance stands at 11.21 GHz. In the high-power regime, the cavity is filled with so much energy that the dispersive limit $g\sqrt{\bar{n}} \ll |f_{\mathrm{g}} - f_{\mathrm{r}}|$ is no longer valid. As the power decreases, the cavity resonance starts becoming highly non-linear and bistable [57]. When the power is low enough such that the cavity is filled with an average of few photons $\langle \hat{n} \rangle \approx 1$, its frequency response becomes linear and symmetric around 11.23 GHz. This linear behaviour establishes at $P_{\mathrm{in}} = -32\,\mathrm{dBm}$. We set the cavity drive power to this value in order to perform qubit spectrosopy.

5.2 Qubit spectroscopy

In circuit-QED, qubit spectroscopy consists of the measurement of the qubit energy levels using a cavity as a readout component. The energy levels can be inferred by measuring the change in the cavity transmission coefficient at resonance $|S_{21}(f_\mathrm{r})|$ as a second drive f_d is swept across a defined frequency range. To perform this measurement, two generators are connected to a common combiner, whose output is connected to the input port of the 3D cavity. One generator produces a continuous drive at f_r so that the magnitude of the transmission coefficient at resonance $|S_{21}(f_\mathrm{r})|$ is constantly monitored (hereafter, this drive will referred to as the RF drive). At the same time, the second generator produces a continuous drive with frequency f_d, which is swept across a wide range in steps of 1 MHz (from now on, this signal will be called the qubit drive). When f_d is far away from the qubit transition frequency f_{01}, the value of $|S_{21}(f_\mathrm{r})|$ remains unchanged. However, when $f_\mathrm{d} \approx f_{01}$, the transmission coefficient $|S_{21}(f_\mathrm{r})|$ significantly changes; this behaviour arises from the fact that the cavity resonance shifts in frequency when the qubit gets excited as predicted by the generalised Jaynes-Cummings hamiltonian in the dispersive regime[1]. Figure 5.2a shows $|S_{21}(f_\mathrm{r})|$ as a function of qubit drive: a dip, corresponding to the first qubit energy level, is clearly visible at $f_{01} = 9.29\,\mathrm{GHz}$. This dip has the the form of a Lorentzian with a finite linewidth γ, which is related to the qubit relaxation times T_1, T_2 by the relation $\gamma = \sqrt{1/T_2^2 + 4\Omega^2 T_1/T_2}$, where Ω is the Rabi rate. At low drive powers $\Omega \ll 1$, the linewidth of the qubit gives a rough estimate of its dephasing time $\gamma \approx 1/T_2$. This parameter will be measured in a more accurate way with Ramsey fringe experiments in Section 5.7.

[1]Note that depending on the external quality factor of the cavity, the signal-to-noise ratio of qubit spectroscopy can be increased by measuring a change in phase of the transmission coefficient $\arg[S_{21}(f_\mathrm{r})]$. Ideally, an optimal quadrature should be calibrated and measured.

Once the qubit transition frequency f_{01} has been located, we can perform qubit spectroscopy at a higher qubit drive power as shown in Fig. 5.2b. In this figure, two features are clearly visible, one corresponding to f_{01} and the other one to $f_{02}/2$. The second dip at $f_{02}/2$ originates from two photon processes exciting the second energy level of the transmon. This results in a narrow dip located at a lower frequency with respect to f_{01} (recall that the anharmonicity of the transmon is negative). From this measurement, we can extract the charging energy of the qubit[2] $E_{\mathrm{C}} = h(2f_{01} - f_{02}) = h \times 480\,\mathrm{MHz}$. Once E_{C} has been determined, the Josephson energy E_{J} can be derived from the equation $E_{\mathrm{J}} = (hf_{01} + E_{\mathrm{C}})^2 / 8E_{\mathrm{C}} = h \times 24.8\,\mathrm{GHz}$ from which we can compute the ratio $E_{\mathrm{J}}/E_{\mathrm{C}} = 51$, indicating that our charge qubit is in the transmon regime. Note that for an accurate measurement of f_{01} and f_{12}, this characterisation should be performed with drive powers that populate the cavity with less than a photon on average so that the transition frequencies of the qubit are not Stark shifted to lower values.

Qubit spectroscopy can also be performed using a pulsed scheme in which a pulsed qubit drive is applied to the system followed by a long measurement pulse at the cavity frequency. This scheme, however, is not strictly required for a first characterisation of the qubit spectrum and continuous drives can equally be employed.

5.3 Number splitting

In the dispersive limit of circuit QED, the transition frequency f_{01} depends on the number of photons populating the cavity in the following way:

$$f_{01}(\bar{n}) = \tilde{f}_{01} + 2\chi\bar{n},$$

[2]Strictly speaking, this equation is only valid in the limit $E_{\mathrm{J}}/E_{\mathrm{C}} \gg 1$.

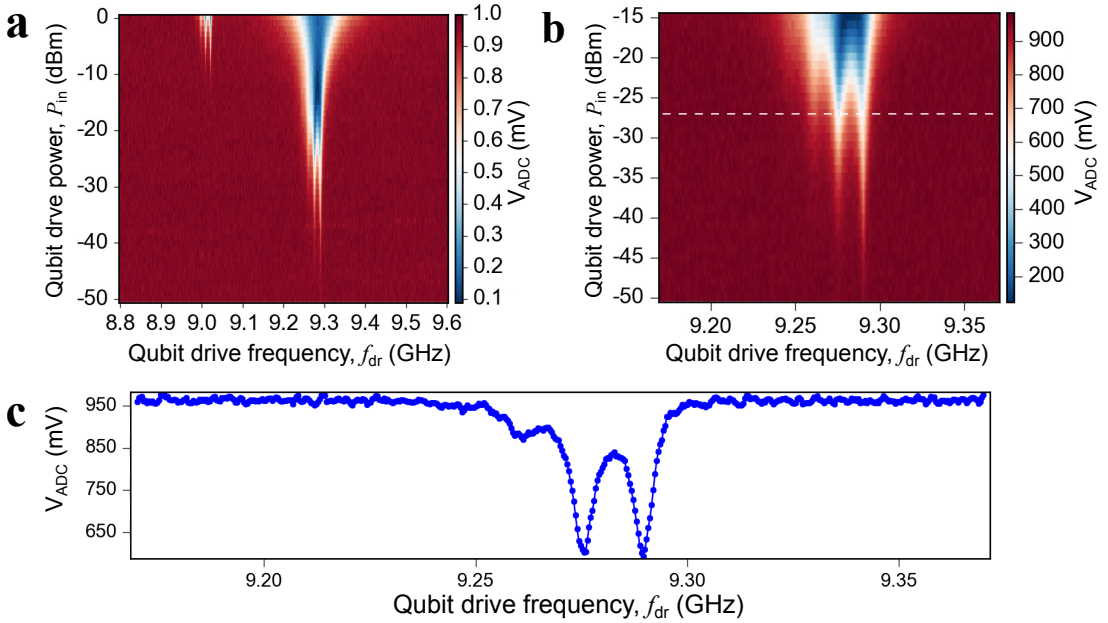

Figure 5.3 | Number splitting. **a**, Qubit spectroscopy as a function of qubit drive power. **b**, Same measurement performed around the f_{01} transition. Number splitting phenomena are recognisable. **c**, Cut through data along the dashed line of panel **b**. The three dips at 9.29 GHz, 9.275 GHz and 9.26 GHz correspond to a cavity population of 1, 2 and 3 photons respectively.

where $\tilde{f}_{01}$ is a normalised qubit frequency, χ is an effective dispersive shift and $\bar{n} = \langle \hat{a}^\dagger \hat{a} \rangle$ is the average number of photons populating the cavity. This equation indicates that the qubit frequency is shifted by 2χ when the cavity contains one photon in average (i.e. when $\langle \hat{a}^\dagger \hat{a} \rangle = 1$).

Figure 5.3a shows a qubit spectroscopy experiment at different qubit drive powers. The spectroscopy is performed by measuring the cavity transmission coefficient $|S_{21}(f_r)|$ with a continuous RF drive that populates the cavity with a coherent electric field. The expectation value of the number of photons inside the cavity $\langle \hat{a}^\dagger \hat{a} \rangle$ is given by a Poissonian distribution with a mean value fixed by the RF drive power. Each spectral line seen in Fig. 5.3b-c corresponds to a different number of photons inside the cavity; this behaviour is known as number splitting. By measuring the frequency spacing of adjacent lines, we can estimate the effective dispersive shift $\chi = 7.6\,\text{MHz}$,

from which we can derive the coupling strength:

$$g = \sqrt{\left|\frac{\chi\Delta(\Delta - E_{\rm C}/h)}{E_{\rm C}/h}\right|} = 195\,\text{MHz},$$

where $\Delta = |f_{01} - f_{\rm r}|$ is the frequency detuning.

5.4 Single qubit gates and coherence

At temperatures $T \ll hf_{01}/k_{\rm B}$, thermal excitations are highly suppressed and the qubit is in its quantum mechanical ground state. When an external drive $f_{\rm d}$ is applied to the qubit such that $f_{\rm d} \approx f_{01}$, the qubit state starts oscillating between the ground and excited state. This behaviour can be appreciated by looking at the Hamiltonian of the driven system. Let us assume that the drive is capacitively coupled to the qubit through a gate capacitance $C_{\rm g}$ and it has the form $V_{\rm d} = A(t)\cos(\omega_{\rm d}t + \varphi)$ where $A(t)$ can be either a square or gaussian modulation envelope of few nanoseconds duration. We are now going to show that the external drive will induce rotations around the x, y and z axis of the Bloch sphere depending on the values of $\omega_{\rm d}$ and φ. The Hamiltonian of our system (transmon + RF drive) is given by:

$$\begin{aligned}\hat{\mathcal{H}}_{\rm tr} + \hat{\mathcal{H}}_{\rm d} &= 4E_{\rm C}\left(\hat{n} - \frac{C_{\rm g}V_{\rm d}}{2e}\right)^2 + \frac{1}{2}E_{\rm J}\hat{\phi}^2 - \frac{E_{\rm J}}{24}\hat{\phi}^4 = \\ &= \underbrace{\hbar\omega_{\rm q}\left(\hat{b}^\dagger\hat{b} + \frac{1}{2}\right) - \frac{E_{\rm C}}{12}\left(6\hat{b}^\dagger\hat{b}\hat{b}^\dagger\hat{b} + 6\hat{b}^\dagger\hat{b} + 3\right)}_{\hat{\mathcal{H}}_{\rm tr}} \underbrace{-2e\beta V_{\rm d}\hat{n}}_{\hat{\mathcal{H}}_{\rm d}},\end{aligned}$$

where we have dropped a constant term proportional to $(C_g V_g/2e)^2$, we have defined $\beta = C_g/C$ and we have introduced the annihilation and creation operators:

$$\hat{n} = -\frac{i}{\sqrt{2}}\left(\frac{E_J}{8E_C}\right)^{1/4}\left(\hat{b} - \hat{b}^\dagger\right) \qquad \hat{\phi} = \frac{1}{\sqrt{2}}\left(\frac{8E_C}{E_J}\right)^{1/4}\left(\hat{b} + \hat{b}^\dagger\right).$$

Substituting the expression of $V_{\rm d}$ and $\hat{n}$ into the drive Hamiltonian $\hat{\mathcal{H}}_{\rm d}$, we obtain:

$$\hat{\mathcal{H}}_{\rm d} = i\hbar\Omega(t)\cos(\omega_{\rm d}t + \phi)\left(\hat{b} - \hat{b}^\dagger\right),$$

where $\Omega(t) = \sqrt{2}e\beta A(t)\left(E_J/8E_C\right)^{1/4}/\hbar$ is called the Rabi rate. Note that the Rabi rate is proportional to the amplitude of the microwave drive $\Omega(t) \propto A(t)$. We can express the system Hamiltonian in the rotating frame by performing the transformation $\hat{R} = e^{i\omega_{\rm d} t \hat{b}^\dagger \hat{b}}$. In the rotating frame, the system Hamiltonian reads[3]:

$$\begin{aligned}
\hat{\mathcal{H}'}_{\rm tr} + \hat{\mathcal{H}'}_{\rm d} &= \hat{R}\hat{\mathcal{H}}\hat{R}^{-1} - i\hbar\dot{\hat{R}}\hat{R}^{-1} = \\
&= \hbar\left(\omega_{\rm q} - \omega_d\right)\hat{b}^\dagger\hat{b} + \frac{\hbar\alpha}{2}\left(\hat{b}^\dagger\hat{b}\hat{b}^\dagger\hat{b} + \hat{b}^\dagger\hat{b}\right) + \\
&\quad + i\hbar\Omega(t)\cos\left(\omega_{\rm d}t + \varphi\right)\left(be^{-i\omega_{\rm d}t} - \hat{b}^\dagger e^{i\omega_{\rm d}t}\right),
\end{aligned}$$

where $\alpha = -E_{\rm C}/\hbar$ is the transmon anharmonicity. If we now calculate the product between the cosine and the exponentials inside the brackets, we finally find:

$$\begin{aligned}
\hat{\mathcal{H}}'_{\rm tr} + \hat{\mathcal{H}}'_{\rm d} &= \hbar\left(\omega_{\rm q} - \omega_{\rm d}\right)\hat{b}^\dagger\hat{b} + \frac{\hbar\alpha}{2}\left(\hat{b}^\dagger\hat{b}\hat{b}^\dagger\hat{b} + \hat{b}^\dagger\hat{b}\right) + \\
&\quad + \frac{\hbar\Omega(t)}{2}\left[\cos\varphi\left(-i\hat{b}^\dagger + i\hat{b}\right) - \sin\varphi\left(\hat{b} + \hat{b}^\dagger\right)\right]
\end{aligned}$$

where we have dropped terms rotating at $2\omega_{\rm d}$ (this is the so-called rotating wave approximation). It is possible to map the fermionic operators $\hat{b}$, $\hat{b}^\dagger$ onto the Pauli matrices:

$$\hat{b}^\dagger\hat{b} \longleftrightarrow \frac{I + \hat{\sigma}_z}{2} \qquad \left(-i\hat{b}^\dagger + i\hat{b}\right) \longleftrightarrow \hat{\sigma}_y \qquad \left(\hat{b} + \hat{b}^\dagger\right) \longleftrightarrow \hat{\sigma}_x.$$

Making these substitutions, we have:

$$\begin{aligned}
\hat{\mathcal{H}}'_{\rm tr} + \hat{\mathcal{H}}'_{\rm d} &= \frac{\hbar(\omega_{\rm q} - \omega_{\rm d} + \alpha)}{2}\hat{\sigma}_z + \frac{\hbar\Omega(t)\cos\varphi}{2}\hat{\sigma}_y - \frac{\hbar\Omega(t)\sin\varphi}{2}\hat{\sigma}_x = \\
&= \frac{\hbar\Omega_z(t)}{2}\hat{\sigma}_z + \frac{\hbar\Omega_y(t)}{2}\hat{\sigma}_y + \frac{\hbar\Omega_x(t)}{2}\hat{\sigma}_x, \qquad (5.2)
\end{aligned}$$

where in the last step we defined $\Omega_z(t) = \omega_{\rm q} - \omega_{\rm d} + \alpha$, $\Omega_y(t) = \Omega(t)\cos\varphi$, $\Omega_x(t) = -\Omega(t)\sin\varphi$. By tuning the values of φ and $\omega_{\rm d}$, it is possible to implement the desired

[3] Use the Baker-Campbell-Hausdorff formula $e^{\alpha\hat{A}}\hat{B}e^{-\alpha\hat{A}} = \hat{B} + \alpha\left[\hat{A},\hat{B}\right] + \frac{\alpha^2}{2!}\left[\hat{A},\left[\hat{A},\hat{B}\right]\right] + ...$ to perform this rotation.

single qubit gate. In particular, equation (5.2) indicates that a detuning between the drive and the qubit frequency generates rotations around the z axis. The quadratures of the drive, instead, induce rotations around the x and y axis, making the qubit state oscillate between the ground and excited state. This phenomenon is called Rabi oscillation.

The most important single qubit gates are the NOT gate and the Hadamard gate. These gates are implemented by applying a pulse to the qubit for a specific amount of time. This follows from the fact that the total rotation angle of the qubit state is determined by the area under the microwave pulse $\int_0^{t_0} \Omega(t)dt$. By adjusting the amplitude and length of the pulse, we can implement a $\pi/2$ rotation around the x axis (similar to an Hadamard gate) or a π rotation (NOT gate):

$$\begin{aligned} \text{Hadamard gate:} \quad |g\rangle \quad &\rightarrow \quad \frac{|g\rangle + |e\rangle}{\sqrt{2}} \qquad \pi/2\,\text{pulse} \qquad \left(t_0 = \frac{\pi}{2\Omega}\right) \\ X \text{ gate:} \quad |g\rangle \quad &\rightarrow \quad |e\rangle \qquad\qquad\quad \pi\,\text{pulse} \qquad\quad \left(t_0 = \frac{\pi}{\Omega}\right). \end{aligned}$$

These single qubit gates are a crucial part of any quantum computation.

5.5 Rabi oscillations

When a transmon is subject to a microwave pulse in resonance with the qubit frequency, its state starts rotating around the x axis of the Bloch sphere with Rabi frequency $\Omega/2\pi$ and it keeps on rotating as long as the qubit drive is on. Immediately after the pulse ends, the probability p_g of finding the qubit in the ground state is related to the pulse duration t_0 by the following relation [2]:

$$p_g(t_0) = \frac{1}{2} + \frac{1}{2}\cos\left(\frac{\Omega t_0}{2}\right)\exp\left[-t_0(3\Gamma_1 + 2\Gamma_\phi)/4\right], \tag{5.3}$$

where Γ_1, Γ_ϕ are the longitudinal and dephasing rates respectively and will be discussed later. Equation (5.3) indicates that the qubit state oscillates between the

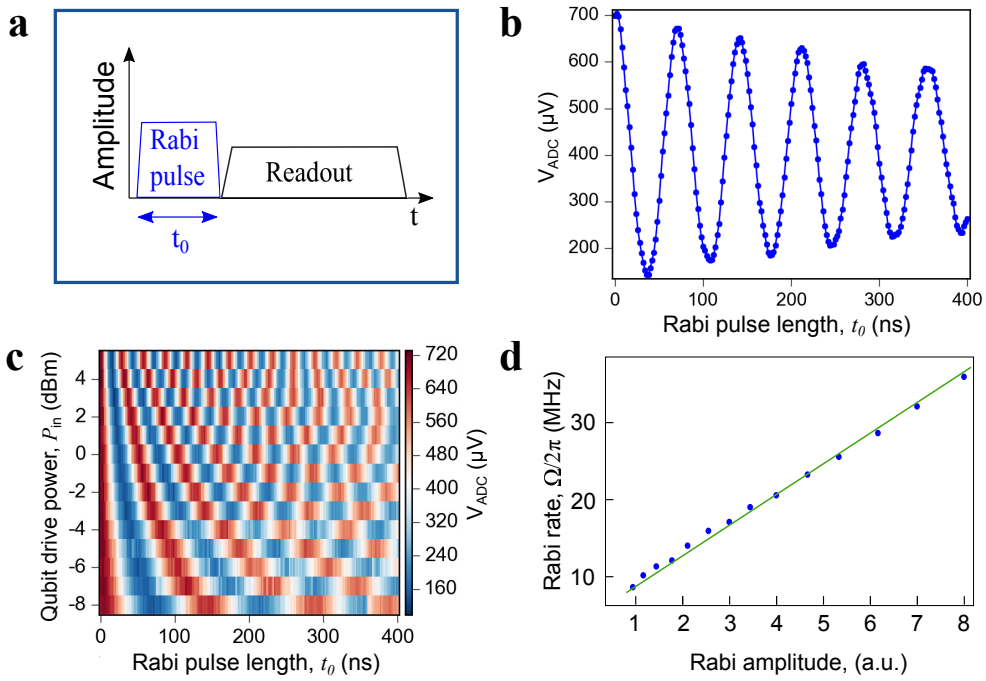

Figure 5.4 | Rabi oscillations. **a**, Pulse scheme implemented to measure Rabi oscillations. A Rabi pulse at the qubit frequency is followed by a long readout pulse at the cavity frequency. Both of the two pulses have a square modulation. The duration of the Rabi pulse is t_0. **b**, Rabi oscillations (blue points) and fit function (green curve) based on equation (5.3). **c**, Rabi oscillations as a function of qubit drive power. The frequency of the Rabi oscillations clearly increases as the power increases. **d**, Rate of the Rabi oscillations as a function of the qubit drive amplitude (blue points) and linear fit (green line).

ground and excited state and it eventually decays to an equilibrium value.

The measurement of Rabi oscillations is performed by applying a pulse to the qubit with varying length t_0, followed by a long readout pulse in resonance with the cavity, as depicted in Fig. 5.4a. This readout pulse is employed to determine the cavity frequency and thus infer the state of the qubit after the pulse. The experiment is averaged thousands of times until the graph shown in Fig. 5.4b is obtained. Figure 5.4c shows the same measurement at different qubit drive powers; we can clearly see that the Rabi oscillation rate increases as the power of the pulse increases. From this measurement we can extract the rate of the Rabi oscillations and plot it as a function of the drive amplitude (see Fig. 5.4d). As expected, there is a linear dependence between these two variables. Once Rabi oscillations have been observed, the

power and length of the drive pulse can be finely adjusted in order to implement π and $\pi/2$ pulses.

5.6 Longitudinal and transverse relaxation rates

In this section, we introduce the concept of qubit relaxation rate. For simplicity, we are going to approximate the transmon as a two-level system and we shall study its dynamics in the Bloch sphere when subject to a periodic drive. The Hamiltonian of the system can be written as:

$$\hat{\mathcal{H}}_{\mathrm{q}} + \hat{\mathcal{H}}_{\mathrm{d}} = \frac{\hbar\omega_{\mathrm{q}}}{2}\hat{\sigma}_z + \frac{\hbar\Omega}{2}\cos(\omega_{\mathrm{d}}t)\hat{\sigma}_x,$$

where ω_{q} is the qubit angular frequency and ω_{d} is the angular frequency of the external continuous drive. In the following, we consider a drive in resonance with the qubit $\omega_{\mathrm{d}} = \omega_{\mathrm{q}}$. In the interaction picture, the dynamics of the qubit is given by the Von Neumann equation:

$$\dot{\rho} = \frac{1}{i\hbar}\left[\hat{\mathcal{H}}_{\mathrm{d}}, \rho\right] = -i\Omega(t)\left(\hat{\sigma}_x\rho - \rho\hat{\sigma}_x\right),$$

where $\Omega(t) = \Omega\cos(\omega_{\mathrm{d}}t)$. The expectation values of the derivative of the Pauli matrices are given by:

$$\begin{aligned}
\left\langle\dot{\hat{\sigma}}_x\right\rangle &= \mathrm{Tr}[\dot{\rho}\hat{\sigma}_x] = -i\Omega(t)\mathrm{Tr}\left[\hat{\sigma}_x\rho\hat{\sigma}_x - \rho\hat{\sigma}_x\hat{\sigma}_x\right] = 0 \\
\left\langle\dot{\hat{\sigma}}_y\right\rangle &= \mathrm{Tr}[\dot{\rho}\hat{\sigma}_y] = -i\Omega(t)\mathrm{Tr}\left[\hat{\sigma}_x\rho\hat{\sigma}_y - \rho\hat{\sigma}_x\hat{\sigma}_y\right] = -\Omega\left\langle\hat{\sigma}_z\right\rangle \\
\left\langle\dot{\hat{\sigma}}_z\right\rangle &= \mathrm{Tr}[\dot{\rho}\hat{\sigma}_z] = -i\Omega(t)\mathrm{Tr}\left[\hat{\sigma}_x\rho\hat{\sigma}_z - \rho\hat{\sigma}_x\hat{\sigma}_z\right] = +\Omega\left\langle\hat{\sigma}_y\right\rangle
\end{aligned}$$

If we introduce the Bloch vector $\mathbf{R} = \left(\left\langle\hat{\sigma}_x\right\rangle, \left\langle\hat{\sigma}_y\right\rangle, \left\langle\hat{\sigma}_z\right\rangle\right)^T$, these relations can be written in a more compact form as:

$$\dot{\mathbf{R}}(t) = \begin{pmatrix} \dot{R}_1 \\ \dot{R}_2 \\ \dot{R}_3 \end{pmatrix} = \mathbf{\Omega}(t) \times \mathbf{R}(t) = \begin{pmatrix} 0 \\ -\Omega(t)R_3 \\ +\Omega(t)R_2 \end{pmatrix},$$

where $\mathbf{\Omega}(t) = (\Omega(t), 0, 0)^T$. These are called Bloch equations.

Within the Bloch-Redfield picture, we can consider an environment weakly coupled to the two-level system. Due to the interaction with the environment, the dynamics of the qubit is affected in the following way:

$$\begin{aligned} \dot{R}_1 &= -\Gamma_2 R_1 \\ \dot{R}_2 &= -\Omega(t) R_3 - \Gamma_2 R_2 \\ \dot{R}_3 &= +\Omega(t) R_2 - \Gamma_1 (R_3 - R_{\mathrm{eq}}), \end{aligned}$$

where we have introduced the longitudinal and transverse relaxation rates Γ_1, Γ_2 and R_{eq} is the thermal equilibrium value of the qubit population. The longitudinal relaxation rate Γ_1 describes a depolarisation mechanism along the qubit quantisation axis and can be written as the sum of two terms:

$$\Gamma_1 = \frac{1}{T_1} = \Gamma_{1\uparrow} + \Gamma_{1\downarrow}, \tag{5.4}$$

where $\Gamma_{1\uparrow}$ ($\Gamma_{1\downarrow}$) indicates the rate at which the qubit goes from the ground to excited state (and viceversa) due to the environment and T_1 is usually called longitudinal relaxation time. Since superconducting qubits are measured in the regime $T \ll \hbar\omega_{\mathrm{q}}/k_{\mathrm{B}}$, the up rate $\Gamma_{1\uparrow}$ is exponentially suppressed. An estimate of the down rate $\Gamma_{1\downarrow}$ can be obtained by modelling the qubit as an electric dipole and studying the energy irradiated per unit time [43]. On the other hand, the transverse rate Γ_2 is the sum of two terms:

$$\Gamma_2 = \frac{1}{T_2} = \frac{\Gamma_1}{2} + \Gamma_\phi, \tag{5.5}$$

where Γ_ϕ is the dephasing rate, i.e. a blurring of the relative phase in a quantum superposition state. The origin of qubit dephasing can be related to fluctuations of the qubit transition frequency due to its coupling with the environment. In the

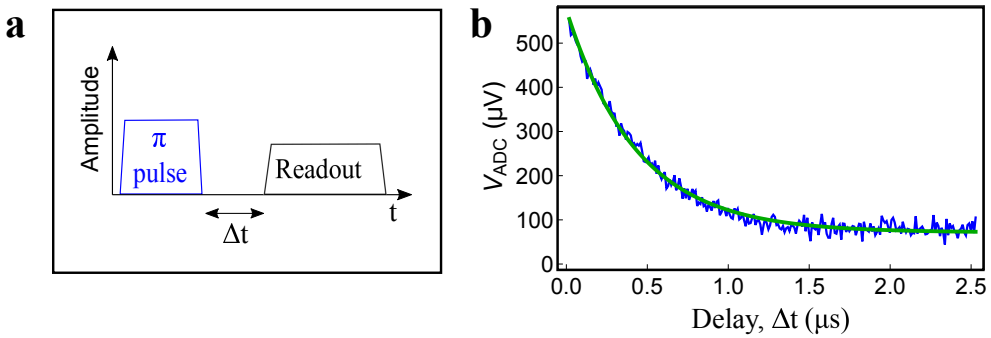

Figure 5.5 | Inversion recovery. **a**, Pulse scheme for inversion recovery. A π pulse is applied to the qubit followed by a long readout pulse delayed by Δt. **b**, Population of the excited state as a function of delay time Δt (blue points). The green curve is a fit to Eq. 5.6.

transmon regime, the dominant contribution to changes in the qubit frequency are fluctuations of the critical current [43].

5.7 Measurements of T_1 and T_2

The longitudinal relaxation time T_1 is measured by promoting the qubit to the excited state and measuring its relaxation to the ground state. The pulse scheme (see Fig. 5.5a) comprises a π pulse followed by a long readout pulse delayed by Δt. This measurement is usually called inversion recovery. Figure 5.5b shows the cavity transmission coefficient at resonance $|S_{21}(f_\mathrm{r})|$ as a function of delay time Δt. This graph clearly shows an exponential decay. By fitting the curve with a simple model

$$p_\mathrm{e}(t) = A + Be^{-t/T_1}, \tag{5.6}$$

we can extract the longitudinal relaxation time of our superconducting qubit $T_1 = 0.6\,\mu$s. Here, A represents an offset and B a scaling factor.

The value of the transverse relaxation time T_2^* can be extracted by performing a Ramsey fringe experiment. This measurement consists of applying two $\pi/2$ pulses detuned by few MHz from the qubit frequency and separated by a time interval Δt as shown in Fig. 5.5a. The first $\pi/2$ pulse rotates the qubit state around the x axis of

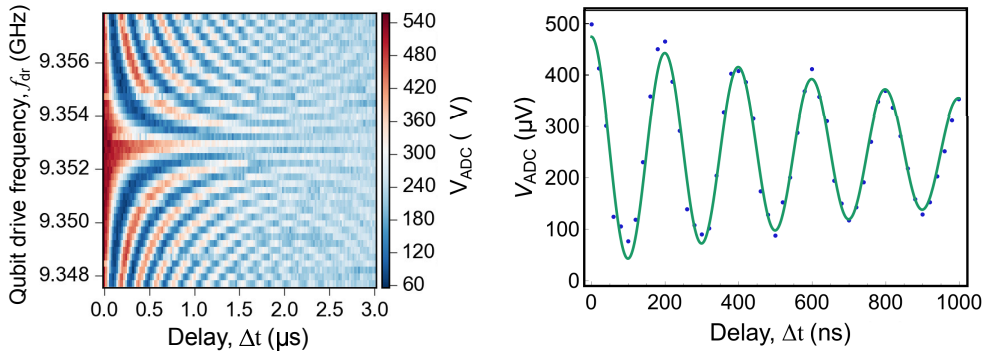

Figure 5.6 | Ramsey fringes. **a**, Ramsey fringe experiment as a function of drive frequency. **b**, Ramsey fringe experiment for the extraction of T_2^* (blue points). The green curve is a fit to equation (5.7).

the Bloch sphere and brings it to a balanced superposition state. In addition, since this pulse is slightly detuned from the qubit frequency, the qubit state starts rotating around the z axis of the Bloch sphere with frequency $\delta_\mathrm{d} = |f_\mathrm{d} - f_\mathrm{q}|$. The second $\pi/2$ pulse rotates the qubit state around the x axis. Depending on the amount of time between the two pulses, the second pulse brings the qubit state back to the ground state (this happens when $\Delta t = n/\delta_\mathrm{d}$) or to the excited state (this takes place when $\Delta t = 1/2\delta_\mathrm{d} + n/\delta_\mathrm{d}$) leading to the oscillations shown in Fig. 5.6b. The fitted exponentially decaying envelope of these oscillations gives the transverse relaxation time according to the fit function:

$$p_e(\Delta t) = A\cos(\delta_\mathrm{d}\Delta t)e^{-\Delta t/T_2^*}. \tag{5.7}$$

For our quartz transmon, we find $T_2^* = 1.18\,\mu$s.

Similar experiments have been performed with a transmon qubit on diamond embedded in a 3D cavity. The extracted coherence time of this qubit was found to be $T_1 = 0.6\,\mu$s, $T_2^* = 0.53\,\mu$s. The main parameters of the quartz and diamond qubits are summarised in Table 5.1. Note that the values of T_1 values are not Purcell limited[4].

[4]When a quantum system with discrete energy levels is placed inside a cavity, its spontaneous emission rate from upper to lower levels is altered. This effect is known as Purcell effect. In circuit-QED, when the qubit frequency is close to the resonator frequency, the decay rate Γ_1 significantly increases.

Table 5.1 | Measured parameters of the 3D quartz and diamond transmons.

	quartz	diamond
f_{r} [GHz]	11.17	11.54
f_{01} [GHz]	9.29	8.12
$f_{02}/2$ [GHz]	9.05	7.89
α [MHz]	-480	-460
$E_{\mathrm{J}}/E_{\mathrm{C}}$	51	43
T_1 [μs]	0.6	0.6
T_2^* [μs]	1.18	0.53

In fact, theory predicts that the upper bound for T_1 due to the Purcell effect is:

$$T_1^{\mathrm{Purcell}} = \frac{(g/\Delta)^2}{k}, \tag{5.8}$$

where k is the cavity linewidth. For the quartz qubit, we find $T_1^{\mathrm{Purcell}} \approx 32\,\mu$s well above the measured value.

5.8 Conclusions

In this chapter, we have presented measurements of superconducting qubits on two new substrates: quartz and diamond. These measurements have been performed by dispersively coupling transmon qubits to 3D cavities. The cavity has been employed as readout component of the qubit state. We found that the dephasing time of the quartz transmon is T_1 limited. On the other hand, the values of T_1 are not Purcell limited. Both the quartz and diamond qubit have coherence times of the order of $1\,\mu$s.

From this preliminary characterisation, it is too early to draw definitive conclusions about the origin of the qubit decoherence: several devices with different fre-

quencies should be measured and compared. The short lifetime of the quartz qubit might be attributed to the piezoelectricity of this material: the electric field across the transmon capacitance can, in principle, couple to bulk modes and limit the overall coherence. However, an accurate FEM simulation would be necessary to fully understand this mechanism.

Our measurements suggest that the coherence time of superconducting qubits on these substrates are long enough to proceed to to couple them to SAW resonators.

Chapter 6

Circuit quantum acoustodynamics with surface acoustic waves

Circuit quantum acoustodynamics deals with the interaction between sound and matter on a chip.

6.1 Introduction

In this chapter, we present measurements of a device in which a tuneable transmon qubit [43] is piezoelectrically coupled to a surface acoustic wave cavity, displaying a surface acoustic version of cavity QED which we coin circuit quantum acoustodynamics (QAD). Unlike the SAWRs discussed in previous chapters of this thesis, the SAW cavity used for this experiment contains two IDTS for transmission measurements. The coupling between the transmon and the SAW cavity is probed in different ways. First, we measure the frequency shift of the acoustic mode as the qubit is flux tuned. Secondly, we measure the acoustic Stark shift of the qubit due to the population of the mechanical resonator and we observe a preferential coupling of the qubit to one longitudinal mode of the acoustic cavity. From these measurements, we extract the coupling and we show that it is in agreement with theoretical expectations. In order to demonstrate the possibility of controlling the device in the time domain, we

demonstrate a time delayed Stark shift made possible by the slow travel of the wave. We also present spectroscopic measurements of the qubit via the Stark shift of the acoustic cavity, indicating that SAWRs can, in principle, be adopted as an alternative qubit readout scheme in quantum information processors.

We also present preliminary measurements of a similar device fabricated on Si/diamond/AlN. This device comprises a tuneable transmon piezoelectrically coupled to a two-port SAWR with a working frequency of 3.15 GHz. Due to the high frequency of the SAW cavity, direct interaction between the acoustic system and the qubit is observed. We also present spectroscopic measurements of the qubit performed with the acoustic cavity and we show measurements of the acoustic Stark shift of the qubit measured via the SAWR. These measurements indicate that strong coupling circuit QAD can be realised with acoustic cavities based on SAW.

The main results of this chapter can be found in reference [51]. In the same year, similar quantum acoustic experiments were performed by other research groups [11, 21, 60, 65, 67].

6.2 Description of the device

In Fig. 6.1, we present a schematic of our measured device consisting of a tuneable transmon embedded in a 2-port SAW resonator. The acoustic resonator has two interdigitated transducers (IDTs) and two gratings. Each IDT is an interdigitated capacitance with $N_\mathrm{t} = 51$ fingers. The periodicity of the transducers is $\lambda_0 = 6\,\mu$m and their horizontal length is $L_\mathrm{t} = (2N_\mathrm{t}-1)\lambda_0/4 = 151.5\,\mu$m. One bus bar of the IDT is grounded whereas the opposite one is connected to a waveguide. As regards the gratings, they consist of $N_\mathrm{g} = 400$ shorted metallic strips connected to ground with a periodicity of $\lambda_0/2$. The horizontal length of each grating is $L_\mathrm{g} = (2N_\mathrm{g} - 1)\lambda_0/4 =$

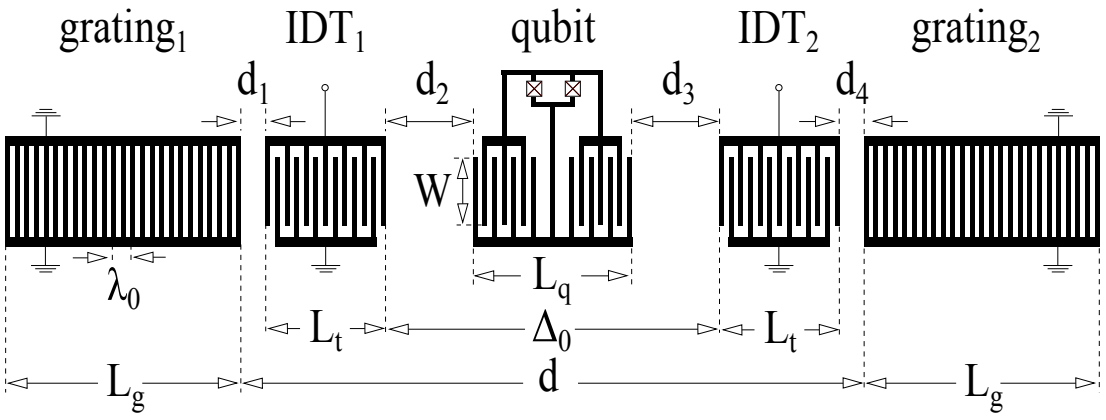

Figure 6.1 | Schematic of a transmon qubit embedded in a 2-port SAW resonator. The 2-port SAW resonator consists of two IDTs and two gratings. The tuneable qubit is formed by a SQUID shunted by an interdigitated capacitance. Due to limited space, the device represented in this figure is not to scale and the number of fingers in the qubit, IDTs and gratings has been reduced with respect to the real device (see text for further details).

1198.5 μm. In the remainder, we will call the left and right transducers IDT_1 and IDT_2 respectively. An analogous nomenclature is adopted for the gratings.

For optimal reflection, the minimal distance between IDT_1 and $\mathrm{grating}_1$ must satisfy the relation $d_1 = (n_1/2 - 1/4)\lambda_0 - \lambda_0/8$, where $n_1 \in \mathbb{N}^+$ [24]. To minimise the cavity length we opted for $n_1 = 3$, leading to $d_1 = 6.75\,\mu$m (a lower value of n_1 might have caused some fabrication issues). The distance d_4 between IDT_2 and $\mathrm{grating}_2$ is the same as d_1. Finally, the minimal distance between the two IDTs satisfies the relation $\Delta_0 = (n_2 - 3/4)\lambda_0$ where $n_2 \in \mathbb{N}^+$. The value of n_2 can be chosen by considering the following. From previous experiments, it has been noted that the internal quality factor of a SAW resonator increases as the distance between the two gratings increases (see Section 4.2). It has also been observed that the number of longitudinal modes supported by the acoustic cavity increases with increasing distance between the two gratings (see Section 4.2). Lastly, the coupling between the qubit and the SAWR is inversely proportional to the square root of the acoustic cavity area (see Section 6.4). For a better coherence, we aimed at having an internal quality factor as high as possible; at the same time, we wanted to maximise the acoustic coupling and

we wanted our cavity to support a small number of longitudinal modes. For these reasons, we have set n_2 to the reasonable value of 158 and therefore $\Delta_0 = 943.5\,\mu$m. As we shall see later, our acoustic cavity supports three longitudinal modes separated by about 1 MHz.

The tuneable transmon is placed in the middle of the acoustic cavity. It consists of a $4 \times 4.57\,\mu\text{m}^2$ SQUID shunted by an interdigitated capacitance. The capacitance of the qubit resembles a transducer itself: it consists of $N_\text{q} = 30$ fingers with one additional central finger connecting the two electrodes of the capacitance (see Fig. 6.1). The interdigitated structure of the qubit capacitance has the same periodicity as the IDTs. Unlike the acoustic components, the qubit is neither directly connected to ground nor to any other waveguide: it is simply capacitively coupled to ground and to an auxiliary 5.85 GHz CPWR employed for independent dispersive qubit readout [93].

The length of the fingers in the IDTs and qubit is denoted by W. A large value of W would considerably decrease diffraction losses (see Section 4.1); at the same time, a small value of W would decrease the acoustic cavity area and increase the acoustic coupling (see Section 6.4). A tradeoff between these two considerations leads us to $W = 11.66\lambda_0 = 70\,\mu$m. Note that at low temperatures, the device undergoes a non-isotropic contraction and the distances between, as well as the dimensions of the acoustic components may vary on the order of tens of nanometers.

Figure 6.2 shows an optical image of the measured device and its equivalent circuit. It has been fabricated on ST-X quartz, which has a SAW speed of $v_\text{f} \approx 3158\,\text{m/s}$ at room temperature. The ground planes, alignment marks and waveguides were patterned with standard photolithographic techniques. These 100 nm thick metallic structures were deposited with our home-made electron-beam evaporator. The SAWR

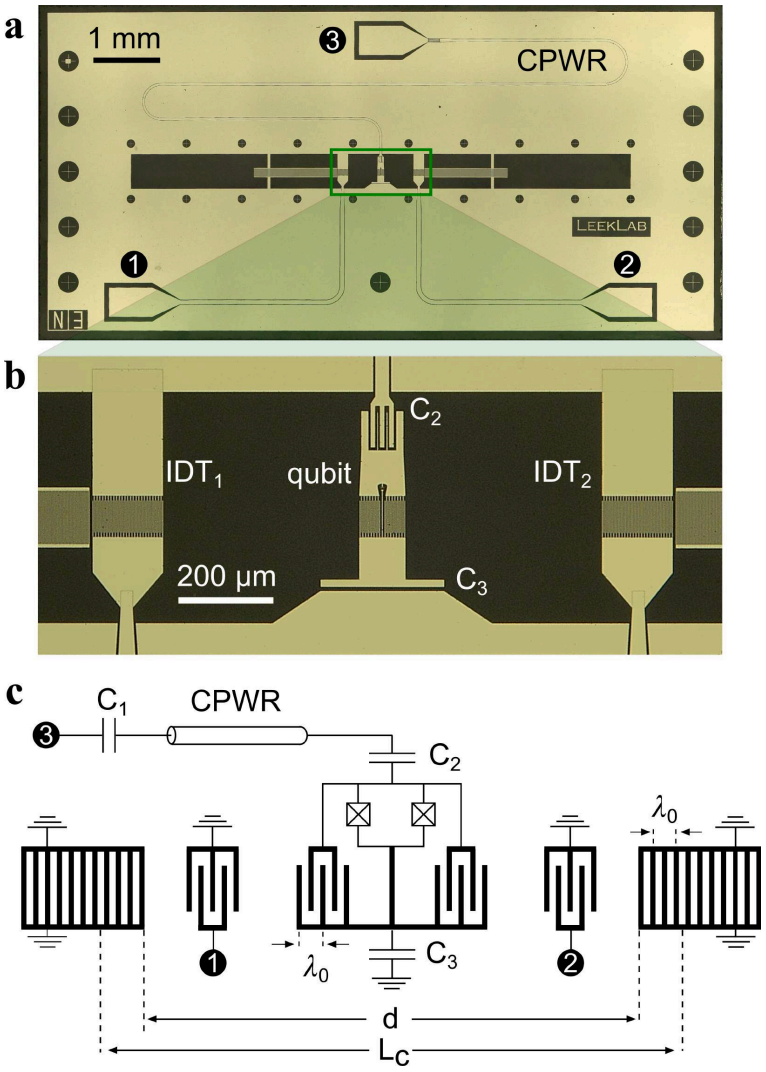

Figure 6.2 | Circuit quantum acoustodynamics device. a, Optical image of the measured device. In the centre of the chip, a transmon is embedded in a SAW cavity. A coplanar waveguide resonator (CPWR) is coupled to the transmon and measured via port 3. The SAW cavity is probed via two interdigitated transducers (IDTs) connected to ports 1 and 2. **b**, Close-up image showing the transmon qubit and SAW IDTs in between the two Bragg gratings that form the SAW cavity. **c**, Equivalent electrical circuit of the device incorporating a spatial schematic of the SAW cavity. The geometrical parameters λ_0, d and L_c denote the wavelength, the distance between the two Bragg gratings, and the effective length of the cavity, respectively.

and the qubit were patterned together in a second electron-beam lithography step. The $200 \times 200\,\mathrm{nm}^2$ junctions were fabricated with the usual Dolan bridge technique and with a double angle evaporation in the following way: firstly 30 nm of aluminium

was deposited, followed by an in-situ oxidation step and a second deposition of 60 nm of aluminium. The overall height of the qubit and SAWR is therefore 90 nm.

The microchip was bonded onto a circuit board, placed inside a home-made oxygen-free copper sample holder and mechanically anchored to the 10 mK plate of the dilution refrigerator (Triton200, Oxford Instruments). The microwave line connecting the CPWR to the external instrumentation is highly attenuated by means of three -20 dBm attenuators. The measured attenuation of this line is -67 dB. The reflected signal coming from the CPWR passes through two 4-8 GHz circulators and reaches a 1-12 GHz HEMT cold amplifier. The signal is then amplified, downconverted and acquired with an analog-to-digital converter at room temperature. The lines connecting IDT_1 and IDT_2 to the VNA have an estimated overall attenuation of -16 dB. These lines are amplified with room temperature microwave components. All measurements presented hereafter have been performed at the base temperature of our dilution refrigerator. For more details on our experimental setup, see Chapter 3.

6.3 SAW cavity characterisation

We performed a preliminary characterisation of the acoustic cavity by measuring its transmission coefficient S_{21} in the frequency domain as shown in Fig. 6.3a. Three mechanical modes are seen at $f_{\mathrm{m1}} = 522.83$ MHz, $f_{\mathrm{m2}} = 523.435$ MHz and $f_{\mathrm{m3}} = 524.58$ MHz. Assuming that f_{m2} is the central resonance, we can extract an effective speed of sound of $v_{\mathrm{e}} = \lambda_0 \times f_{\mathrm{m2}} = 3140.6$ m/s. The slight difference between v_{e} and the textbook room temperature value $v_{\mathrm{f}} = 3158$ m/s may be due to slight device asymmetry and/or stiffness tensor changes or crystal contraction at millikelvin temperatures. Finally, note that these SAW modes are not in their ground state,

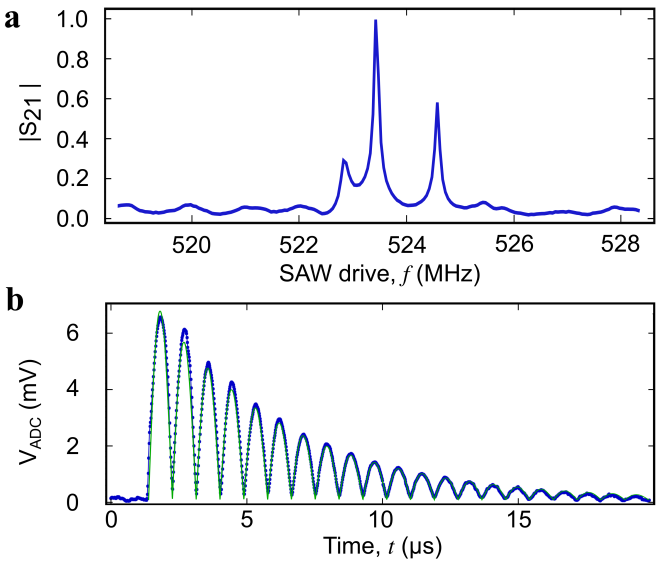

Figure 6.3 | SAW cavity response. a, Normalised linear magnitude of the measured transmission coefficient S_{21} of the 2-port SAWR (blue solid line). The transmitted signal has been acquired with a vector network analyser with input power set at $-30\,\mathrm{dBm}$. **b**, Time resolved measurement of the 2-port SAWR. This measurement has been performed by applying a $800\,\mathrm{ns} \lesssim 2L_c/v_e$ electrical pulse to IDT_1 and acquiring the output signal from IDT_2. The graph shows the voltage difference at the input of the acquisition card. The green curve is a fit to equation 6.1.

due to the mode frequencies $f_{mi} \lesssim k_B T/h$ and low-attenuation connections to room temperature[1].

The acoustic nature of the observed resonant modes can be further tested by measuring the device response to a short coherent drive pulse (see Fig. 6.3b). An exponentially decaying train of pulses is clearly observed in the response, consistent with the applied 800 ns pulse reflecting back and forth between the mirrors of the cavity. The response of the cavity can be described with an heuristic model, in which a train of pulses is modulated by an exponential decay:

$$S_{21}(t) = A \left| \sin\left[\frac{\pi(t-t_0)}{\Delta t}\right] \right| e^{-(t-t_0)/2\tau}, \tag{6.1}$$

where A is a scaling factor, t_0 is a time offset, τ is a decay constant and Δt is the time interval separating adjacent peaks. The decay time of the pulses (i.e. the

[1]The circuit QAD diamond device, that we are going to present at the end of this chapter, exhibits SAW modes f_{mi} satisfying the quantum condition $hf_{mi} \gg k_B T$.

lifetime of phonons in the SAW cavity) is $\tau \approx 2.4\,\mu$s. The pulses measured in the response are separated by $\Delta t = 870\,$ns, consistent with a cavity length of $L_\mathrm{c} = v_\mathrm{e}\Delta t/2 \approx 1365\,\mu$m. As expected, the cavity length is slightly longer than the distance between the two gratings $d = 1260\,\mu$m. This is consistent with the fact that SAWs slightly penetrate into the gratings by an amount $L_\mathrm{p} = (L_\mathrm{c} - d)/2 = 55\,\mu$m (this is a distributed reflection with an effective plane of reflection slightly inside the grating). The reflectivity $|r_s|$ of each finger in the grating can be easily obtained from the relation $4|r_s|L_\mathrm{p} = \lambda_0 \tanh(|r_s|N_\mathrm{g})$, whence $r_s = |0.0273|$, which is higher than the one obtained for high frequency SAW devices in Section 4.2.

The frequency spacing of adjacent modes (the free spectral range) of the cavity is also consistent with the same cavity length, $L_\mathrm{c} = v_\mathrm{e}/2\,|f_\mathrm{m2} - f_\mathrm{m3}| \approx 1365\,\mu$m, where we have used the two higher-quality modes f_m2 and f_m3. Note however that f_m1 is slightly closer in frequency to f_m2. This asymmetric behaviour in the frequency domain may be due to the fact that the grating stopband does not perfectly coincide with the resonance frequency of the IDTs [90].

We have also measured our SAWR in reflection. In Fig. 6.4a-c we present the measured reflection coefficient $S_{11}(f)$ around the three longitudinal modes f_m1, f_m2 and f_m3. Close to resonance, the SAWR can be modelled with an RLC equivalent circuit. According to this model, the analytical expression for the reflection coefficient takes the form:

$$S_{11}(f) = \frac{(Q_\mathrm{m,e} - Q_\mathrm{m,i})/Q_\mathrm{m,e} + 2iQ_\mathrm{m,i}(f - f_\mathrm{m})/f}{(Q_\mathrm{m,e} + Q_\mathrm{m,i})/Q_\mathrm{m,e} + 2iQ_\mathrm{m,i}(f - f_\mathrm{m})/f}. \tag{6.2}$$

Here $Q_\mathrm{m,i}$ is the internal quality factor of the mechanical mode and $Q_\mathrm{m,e}$ is the external quality factor due to the presence of the IDT and the measurement port. From a fit to the experimental data, we find $Q_\mathrm{m1,i} = 4830$, $Q_\mathrm{m2,i} = 7020$, $Q_\mathrm{m3,i} = 7600$,

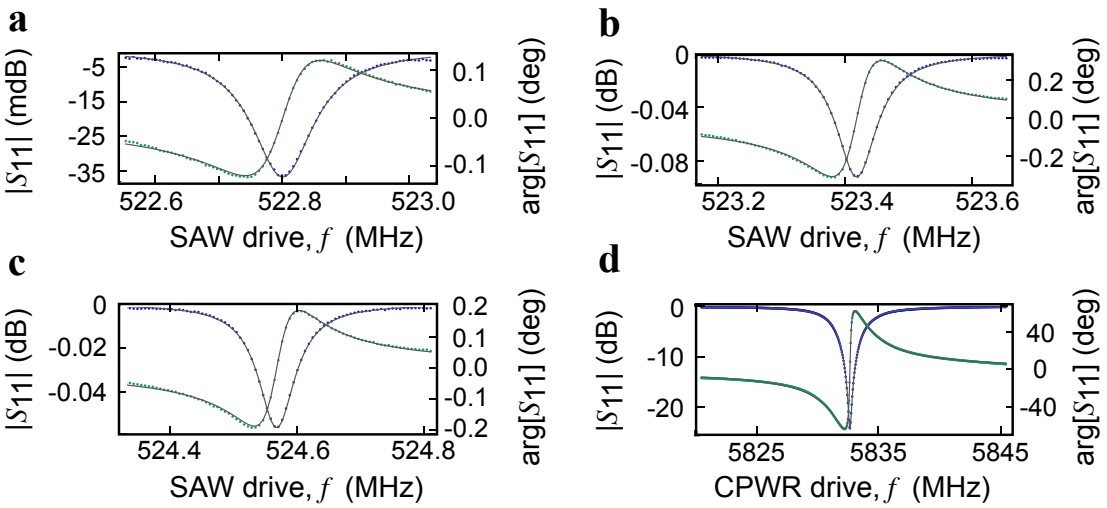

Figure 6.4 | Reflection coefficient of the 2-port SAWR and CPWR. a-c, Magnitude (blue) and phase (green) of the measured reflection coefficient $S_{11}(f)$ of the longitudinal modes f_{m1}, f_{m2} and f_{m3}. Solid lines are a fit to equation (6.2). **d**, Magnitude (blue) and phase (green) of the measured reflection coefficient $S_{11}(f)$ of the CPWR mode f_{r}. Solid lines are a fit to equation (6.2). A background due to the measurement setup has been subtracted in all these frequency responses.

$Q_{\mathrm{m1,e}} = 2.34 \times 10^6$, $Q_{\mathrm{m2,e}} = 1.33 \times 10^6$, and $Q_{\mathrm{m3,e}} = 2.33 \times 10^6$. In terms of loss rate, these values can be expressed as $\kappa_{\mathrm{m1}} = 108\,\mathrm{kHz}$, $\kappa_{\mathrm{m2}} = 75\,\mathrm{kHz}$ and $\kappa_{\mathrm{m3}} = 69\,\mathrm{kHz}$.

For completeness, we also report the measured reflection coefficient of the CPWR in Fig. 6.4d. Its resonance frequency depends on its length L_{r} and the effective dielectric constant of the substrate $\varepsilon_{\mathrm{eff}}$ in the following way: $f_{\mathrm{r}} = c/2L_{\mathrm{r}}\sqrt{\varepsilon_{\mathrm{eff}}}$, where $L_{\mathrm{r}} = 14100\,\mu\mathrm{m}$, and $\varepsilon_{\mathrm{eff}} \approx 3.3$ for quartz. By fitting the CPWR response in the frequency domain, we obtain $Q_{\mathrm{m2,i}} = 3240$ and $Q_{\mathrm{m3,e}} = 3630$. In terms of loss rate, these values can be expressed as $\kappa_{\mathrm{r}} = 3.41\,\mathrm{MHz}$.

6.4 Coupling strength between a charge qubit and a SAW cavity

When a surface perturbation on a piezoelectric crystal travels through an interdigitated capacitor with the same periodicity as the incoming wave, the capacitor develops an oscillating voltage on its electrodes. This phenomenon can be exploited to couple a surface acoustic wave to a transmon with a suitably shaped capacitance.

The coupling strength between a transmon and a SAW cavity can be calculated by considering the charge q and the potential difference V_0 generated by a single phonon on the electrodes of the transmon. Let us first derive the potential difference V_0. The zero-point mechanical motion associated with a single phonon inside a SAW cavity is:

$$U_0 = \sqrt{\frac{\hbar}{2\rho A_\mathrm{c} v_\mathrm{e}}}, \tag{6.3}$$

where $A = W \times L_\mathrm{c} = 95900\,\mu\mathrm{m}^2$ is the area of the acoustic cavity and $\rho = 2647\,\mathrm{kg/m}^3$ is the quartz mass density. From the zero-point mechanical motion, we can easily derive the value of the zero-point electric potential [83]:

$$\phi_0 \approx \frac{e_\mathrm{pz}}{\varepsilon} U_0 = \frac{e_\mathrm{pz}}{\varepsilon} \sqrt{\frac{\hbar}{2\rho A_\mathrm{c} v_\mathrm{e}}}, \tag{6.4}$$

where ε is the permittivity of the substrate and e_pz is a component of the quartz piezoelectric tensor which depends on the propagation direction (for ST-X quartz [62], $e_\mathrm{pz}/\varepsilon \approx 2.0\,\mathrm{V/nm}$). As mentioned earlier, the transmon capacitance responds in a more effective way to waves sharing the same periodicity as its structure. Hence, the electric potential ϕ_0 has to be scaled according to the following normalised array factor [62]:

$$A(f) = \left| \frac{\sin\left[N_\mathrm{q}\pi(f - f_0)/2f_0\right]}{N_\mathrm{q}\pi(f - f_0)/2f_0} \right|. \tag{6.5}$$

Note that for $f = f_0$, $A(f) = 1$. The potential difference is thus $V_0 = \phi_0 A(f)$. As regards the charge generated by the surface acoustic wave on the transmon electrodes, its value is given by

$$\hat{q} = 2e\beta\hat{n}$$

where $2e$ is the charge of a Cooper pair, β is a prefactor, $|j\rangle$ is an eigenstate of the transmon and $\hat{n}$ is a quantum operator indicating the number of Cooper pairs in

excess (or deficit) on the superconducting island. To calculate the coupling in the transmon eigenbasis, we need the matrix element [43]

$$\langle j+1|\hat{q}|j\rangle = 2e\beta\langle j+1|\hat{n}|j\rangle \approx 2e\beta\sqrt{\frac{j+1}{2}}\left(\frac{E_{\mathrm{J}}(\phi)}{8E_{\mathrm{C}}}\right)^{1/4}.$$

For the first two levels of the transmon, we have $\langle 1|\hat{q}|0\rangle \approx e\beta\left(E_{\mathrm{J}}(\phi)/2E_{\mathrm{C}}\right)^{1/4}$. It remains to calculate the prefactor β. This parameter originates from the fact that not all of the charge generated by the surface acoustic wave will be localised on the transmon capacitance: part of it will be distributed on the gate capacitance C_2, on the junction capacitance C_{J}, and on strain capacitances C_s to ground planes and other metallic components of the chip. Hence

$$\beta = \frac{C_{\mathrm{q}}}{C_2 + C_s + C_{\mathrm{J}} + C_{\mathrm{q}}} = \frac{C_{\mathrm{q}}}{C_{\Sigma}}.$$

where $C_{\mathrm{q}} = WN_{\mathrm{q}}\varepsilon/2$ is the capacitance of the qubit interdigitated structure. The coupling strength between a transmon and a SAW cavity can be written as follows:

$$\begin{aligned}\lambda(\phi, f) &= \frac{\langle 1|\hat{q}|0\rangle\, V_0}{h} \approx \frac{2e}{h}\beta\langle 1|\hat{n}|0\rangle\phi_0 A(f) = \\ &= \frac{e\beta}{h}\left(\frac{E_{\mathrm{J}}(\phi)}{2E_{\mathrm{C}}}\right)^{1/4}\phi_0 A(f),\end{aligned}$$

where the value of $E_{\mathrm{J}}(\phi)$ depends on the qubit frequency in the following way $E_{\mathrm{J}}(\phi) = [hf_{\mathrm{q}}(\phi) + E_{\mathrm{C}}]^2/8E_{\mathrm{C}}$. Substituting values related to our device and assuming that the frequency of the qubit is $f_{\mathrm{q}} = 2.52\,\mathrm{GHz}$ and approximating $\beta \approx 1$ and $A(f) \approx 1$, we have:

$$\begin{aligned}\lambda &\approx \frac{e}{h}\left(\frac{3.4\,[\mathrm{GHz}]}{2.0\times 0.31\,[\mathrm{GHz}]}\right)^{1/4} 2\left[\frac{\mathrm{nV}}{\mathrm{m}}\right]\sqrt{\frac{\hbar}{2\times 2647\,[\mathrm{kg/m^3}]\times 95900\,[\mu\mathrm{m}^2]\times 3140.6\,[\mathrm{m/s}]}} = \\ &= 6.0\,\mathrm{MHz}.\end{aligned}$$

This value provides an estimate of the maximum coupling attainable between a superconducting qubit and a SAW cavity in our experiment.

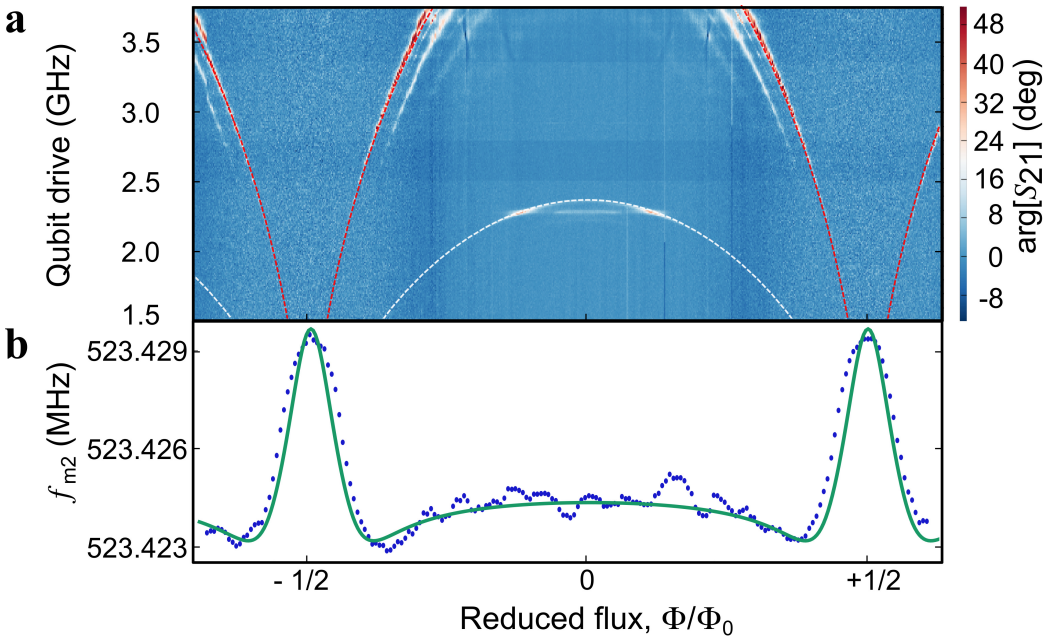

Figure 6.5 | Flux dependent acoustic shift. a, Qubit spectroscopy performed with the CPWR as a function of reduced magnetic flux. The red dashed line is a fit to equation (6.7) and indicates the qubit transition frequency $f_{\mathrm{q}}(\Phi)$. The white dashed line, with analytical form $f_{\mathrm{q}}(\Phi)/2$, denotes an excitation of the qubit via a two photon process. **b**, Measured resonance frequency of the acoustic mode f_{m2} as a function of reduced flux at fixed SAW drive power of $-80\,\mathrm{dBm}$ (blue points) and numerical model based on equation (6.6) (green solid curve).

6.5 SAW resonance as a function of flux

Having characterised the SAW cavity, we now proceed to examine its interaction with the superconducting qubit, a flux-tuneable transmon. An appropriate quantum-mechanical description of this system (including the readout CPWR) is the generalized Jaynes-Cummings Hamiltonian of two resonators both coupled to the same transmon qubit (for reasons that shall become clear, we will only consider the central acoustic mode at f_{m2}, which we hereafter refer to as the SAW resonator, SAWR):

$$\begin{aligned}\hat{H}/h &= \sum_j f_j(\Phi)|j\rangle\langle j| + f_{\mathrm{r}}\hat{a}^\dagger\hat{a} + f_{\mathrm{m2}}\hat{b}^\dagger\hat{b} + \\ &+ \sum_{i,j}\left[g_{ij}(\Phi)|i\rangle\langle j|\left(\hat{a}+\hat{a}^\dagger\right) + \lambda_{\mathrm{m2},ij}(\Phi)|i\rangle\langle j|(\hat{b}+\hat{b}^\dagger)\right],\end{aligned} \tag{6.6}$$

where $f_j(\Phi)$ are the flux dependent transmon transition frequencies, $f_\mathrm{r} = 5.83\,\mathrm{GHz}$ is the CPWR frequency, $\hat{a}$ ($\hat{a}^\dagger$) and $\hat{b}$ ($\hat{b}^\dagger$) are the annihilation (creation) operators of the microwave cavity and of the mechanical resonator, respectively, and $g_{ij}(\Phi)$ [$\lambda_{\mathrm{m2},ij}(\Phi)$] is the coupling strength between the qubit and the CPWR (SAWR). Hereafter, we shall denote the coupling strength between the CPWR (SAWR) and the first energy level of the qubit simply by g (λ_m2). The transition frequency f_q between the first two energy levels of the qubit is tuned by applying an external magnetic flux Φ to its superconducting loop, and its value is given by:

$$hf_\mathrm{q}(\Phi) = \sqrt{8E_\mathrm{C}E_\mathrm{J0}\cos|\pi\Phi/\Phi_0|} - E_\mathrm{C}, \tag{6.7}$$

where $\Phi_0 = h/2e$ is the magnetic flux quantum, and $E_\mathrm{C} = h \times 0.31\,\mathrm{GHz}$, $E_\mathrm{J0} = h \times 10.7\,\mathrm{GHz}$ are the Coulomb and maximum Josephson energy of the qubit (obtained from standard qubit spectroscopy). The electrical coupling between the CPWR and the qubit mainly originates from the capacitance C_2 shown in Fig. 6.1b. The acoustic coupling is instead due to the potential difference generated by the acoustic wave on the electrodes of the qubit as explained in Section 6.4. For convenience, we report here its analytical form:

$$\lambda_\mathrm{m2}(\Phi, f) = \frac{e}{h}\frac{C_\mathrm{q}}{C_\Sigma}\left(\frac{E_\mathrm{J}(\Phi)}{2E_\mathrm{C}}\right)^{1/4}\frac{e_\mathrm{pz}}{\varepsilon}\sqrt{\frac{\hbar}{2\rho A_\mathrm{c} v_\mathrm{e}}}A(f), \tag{6.8}$$

where e is the electron charge, C_q and C_Σ are the qubit capacitance and the total capacitance seen by the qubit respectively, e_pz is the piezoelectric coupling coefficient, ε is the substrate permittivity, ρ is the substrate mass density, A_c is the acoustic cavity area, and $A(f)$ is a normalized array factor.

As a first probe of the interaction between the qubit and the SAW mode, we measure both the frequency of the qubit (via the CPWR) and the acoustic mode f_m2 as a function of magnetic flux Φ (see Fig. 6.5). The qubit frequency (see Fig. 6.5a) fits

well to equation (6.7), while the SAW mode frequency (see Fig. 6.5b) also shows a flux dependence with the same periodicity. By fitting the experimental curve of Fig. 6.5b with a QuTiP[2] numerical model [41] based on equation (6.6), we can extract the value of the acoustic coupling and we find $\lambda_{\mathrm{m2}} = 5.7 \pm 0.5\,\mathrm{MHz}$ at $f_{\mathrm{q}} = 2.52\,\mathrm{GHz}$, which is in good agreement with an estimate based on equation (6.8), $\lambda_{\mathrm{m2}} = 6.0\,\mathrm{MHz}$. In our simulation, the transmon coupling strengths and level spacings are calculated by diagonalising the Hamiltonian for a Cooper-pair box including many charge states [43]. The free parameters of the model are the coupling strength λ_{m2}, the asymmetry of the critical currents of the two Josephson junctions [$d_{\mathrm{sym}} = (I_{c1} - I_{c2})/(I_{c1} + I_{c2}) = 0.09$] and the effective temperature of the device ($T = 85\,\mathrm{mK}$). The additional SAW modes at f_{m1} and f_{m3} do not show any detectable flux dependence. This is in agreement with the expectation that these modes are antisymmetric with respect to the center of the cavity, whereas the central mode f_{m2} and the qubit transducer geometry are both symmetric.

6.6 Acoustic Stark shift of the qubit

A second method to investigate the acoustic coupling between the qubit and the SAW is to measure the AC Stark shift between the two systems in the far-detuned limit (see Fig. 6.4), in which the Hamiltonian of the SAW-qubit system becomes:

$$\hat{H}_{\mathrm{disp}}/h \approx f_{\mathrm{m2}}\hat{b}^{\dagger}\hat{b} + \frac{1}{2}\left(f_{\mathrm{q}} + 2\chi\hat{b}^{\dagger}\hat{b} + \chi\right)\hat{\sigma}_z, \tag{6.9}$$

where $\hat{\sigma}_z$ is a Pauli operator and we have approximated the transmon as a two-level system for simplicity. We first set the magnetic flux such that the qubit frequency is $f_{\mathrm{q}} = 3.29$ GHz, and the qubit-SAW detuning is $\Delta = 2.77\ \mathrm{GHz} \gg \lambda_{\mathrm{m2}}$. In Fig. 6.6a-b, we show the qubit frequency shift as a function of SAW drive frequency close to the

[2]This model has been developed in collaboration with A. F. Kockum.

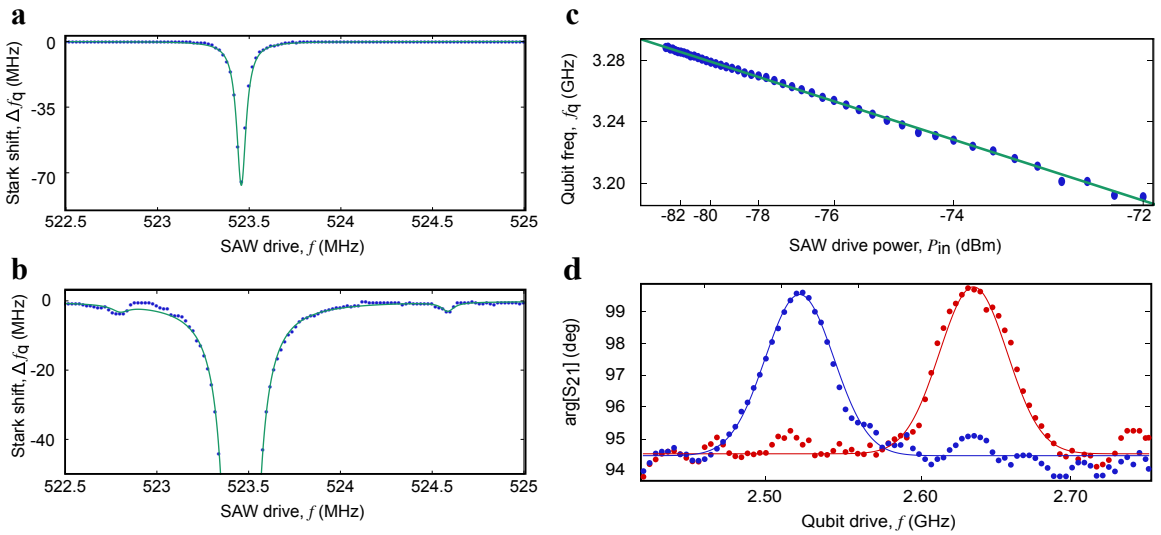

Figure 6.6 | Acoustic Stark shift. a-b, Qubit frequency as a function of SAW drive at two different powers: −74 dBm (**a**) and −64 dBm (**b**). The green curves are Lorentzian fits to the data points. **c**, Qubit frequency as a function of SAW drive power $P_{\rm in}$ at a fixed SAW frequency $f_{\rm m2}$ (blue points). The green solid line is a linear fit to the data. Note that the x axis is in dBm and the scale is logarithmic. **d**, Qubit spectroscopy performed with the SAWR at two different flux values [$0.395\Phi_0$ (red points) and $0.403\Phi_0$ (blue points)]. The solid lines are gaussian fits to the data points.

acoustic modes at two different drive powers. At the lower power of $P_{\rm in} = -74$ dBm, we clearly observe a qubit frequency shift only at the frequency of the central SAW mode $f_{\rm m2}$. The shift fits well to a Lorentzian centered at $f_{\rm m2}$, and has a FWHM of 60 ± 5 kHz, close to that obtained for the SAW mode measured via S_{21}. No such frequency shift is observed at the other SAW mode frequencies $f_{\rm m1}$ and $f_{\rm m3}$ until higher powers. From a second measurement at $P_{\rm in} = -64$ dBm, high enough to observe small shifts at $f_{\rm m1}$ and $f_{\rm m3}$, we can estimate the coupling of the qubit to these additional modes. Assuming that $\lambda_{\rm m2} = 5.7$ MHz from the fit to the flux dependence of $f_{\rm m2}$, and taking into account the different drive powers of the two experiments, we can estimate the coupling to the two side modes to be $\lambda_{\rm m1} \approx 380$ kHz and $\lambda_{\rm m3} \approx 340$ kHz, more than an order of magnitude lower than the coupling to the central mode. Figure 6.6c illustrates the qubit frequency shift as a function of drive power at frequency $f_{\rm m2}$. The shift is observed to be linear, in agreement with the AC

Stark effect.

6.7 Qubit spectroscopy using the SAWR as readout component

In a complementary experiment, we measure the Stark shift of the SAW mode frequency when the qubit excited state is populated (see Fig. 6.6d), an acoustic equivalent of circuit QED dispersive qubit readout [93]. This measurement can be used to extract an independent estimate of the acoustic coupling λ_{m2} and it is performed as follows: a continuous qubit drive is swept across the qubit frequency, while a measurement tone is applied to the SAWR. When the qubit drive is in resonance with the qubit frequency, the SAWR resonance experiences a coherent shift as shown in Fig. 6.6d (since we are applying a saturating pulse to the qubit, the qubit profile is not lorentzian but gaussian). We carry out such a measurement at two different values of the magnetic flux, in both cases measuring the phase shift $\Delta\phi$ of a probe drive at f_{m2} under strong driving of the qubit. We have $\Delta\phi = 2\arctan(|\chi|/\kappa_{m2})$, where κ_{m2} is the mechanical mode linewidth, $\chi = -\lambda_{m2}^2 E_C/\Delta(\Delta - E_C)$ is the dispersive shift for a transmon and $\Delta = f_q - f_{m2}$ is the frequency detuning. From Fig. 6.6d, we have $\Delta = 2.00\,\text{GHz}$ and $\Delta\phi = 4.9^\circ \pm 0.3^\circ$ and since $\kappa_{m2} = 75\,\text{kHz}$, we find $|\chi| = 3.2$ kHz and $\lambda_{m2} = 5.9 \pm 0.2\,\text{MHz}$, in close agreement with our earlier estimate obtained by fitting the flux dependence of f_{m2}. We can now use this measurement of χ to obtain an estimate for the average coherent phonon population $\bar{n} = \langle \hat{b}^\dagger \hat{b} \rangle$ of the SAW mode in the experiment shown in Fig. 6.6a, obtaining $\bar{n} \approx 10^4 (10^5)$ for $P_{in} = -74(-64)\,\text{dBm}$. These values are within the limit in which the dispersive Hamiltonian remains valid [10], $\lambda_{m2}\sqrt{\bar{n}} < \Delta$.

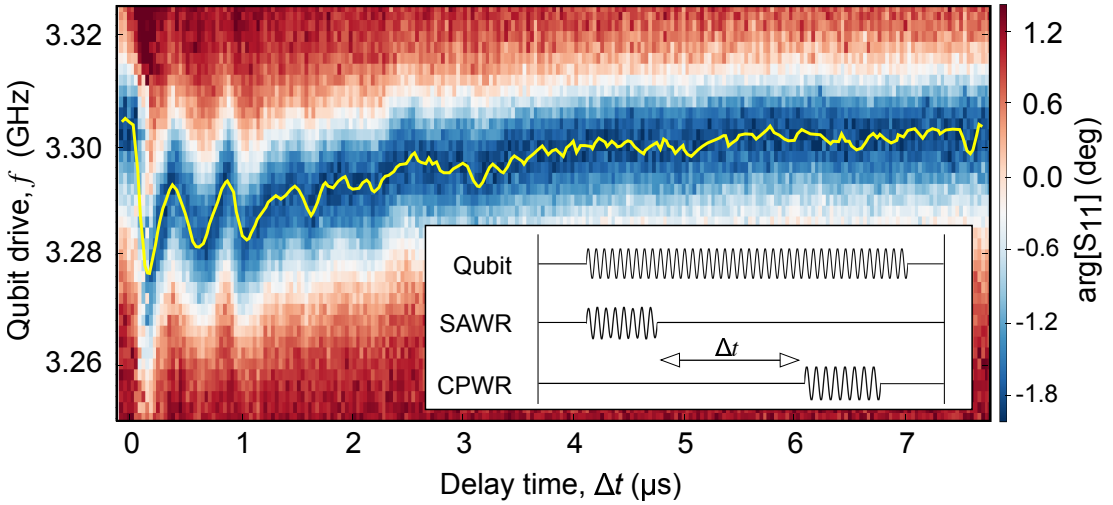

Figure 6.7 | Time-delayed acoustic Stark shift. Measured time-delayed acoustic Stark shift of the qubit. The yellow solid line indicates the qubit frequency. Inset: pulse scheme related to this experiment: a continuous drive excites the qubit, while two short 100 ns pulses delayed by Δt drive the SAWR and the CPWR for the readout.

6.8 Time-delayed acoustic Stark shift

We finally report an experiment in which we use the slow speed of the acoustic wave to apply a time-delayed Stark shift to the qubit, occurring as a SAW pulse passes to the qubit inside the SAW cavity (see Fig. 6.7). A short 100 ns pulse is first applied to one SAW IDT, then a time delayed pulsed measurement of the qubit is subsequently carried out via the CPWR (with a 100 ns measurement pulse). A continuous drive is applied to the qubit throughout the experiment, the frequency of which is varied to determine the qubit frequency. The qubit is observed to shift lower in frequency initially at a time 170 ns after the SAW pulse is applied, exactly consistent with the time-of-flight of the SAW pulse between the IDT and qubit. Several further frequency dips are then observed, spaced by approximately 430 ns, again consistent with the SAW time-of-flight from qubit to one Bragg mirror and back again. The qubit frequency is observed to decay back to its undisturbed value over a timescale of 3 μs, similar to the phonon lifetime of the SAW cavity. The

multiple reflections between qubit, IDTs, and Bragg mirrors likely serve to smooth out the response beyond a time delay of around 1 μs. As well as demonstrating the uniquely slow propagation of SAWs in a quantum device, this experiment also serves to further prove that the Stark shifts that we observe are indeed due to the acoustic field of the SAW mode, rather than a crosstalk of the electromagnetic signal applied to the IDT directly to the qubit.

6.9 Preliminary measurements on diamond: direct coupling

In this section we present preliminary measurements of the direct coupling between a superconducting qubit and an acoustic cavity on diamond. The device under investigation is similar to the one presented at the beginning of this chapter: an interdigitated transmon is embedded in a 2-port SAW resonator and a CPWR is employed as readout component of the qubit state. The main difference is the substrate adopted for this experiment, which consists of three layers:

- a 500 μm silicon base,
- a 100 μm polycristalline diamond layer grown with CVD techniques,
- a 1 μm AlN film sputtered on top of the diamond.

The silicon serves as support for the chemical deposition of the diamond, which is mainly used for its very high speed of sound. Aluminium nitride provides the piezoelectricity needed for the acoustic transduction. The diamond and AlN layers provide a speed of sound of $v_e \approx 10600\,\mathrm{m/s}$ and a coupling strength of $K = 0.3\,\%$. More information about the fabrication of this substrate can be found in [77].

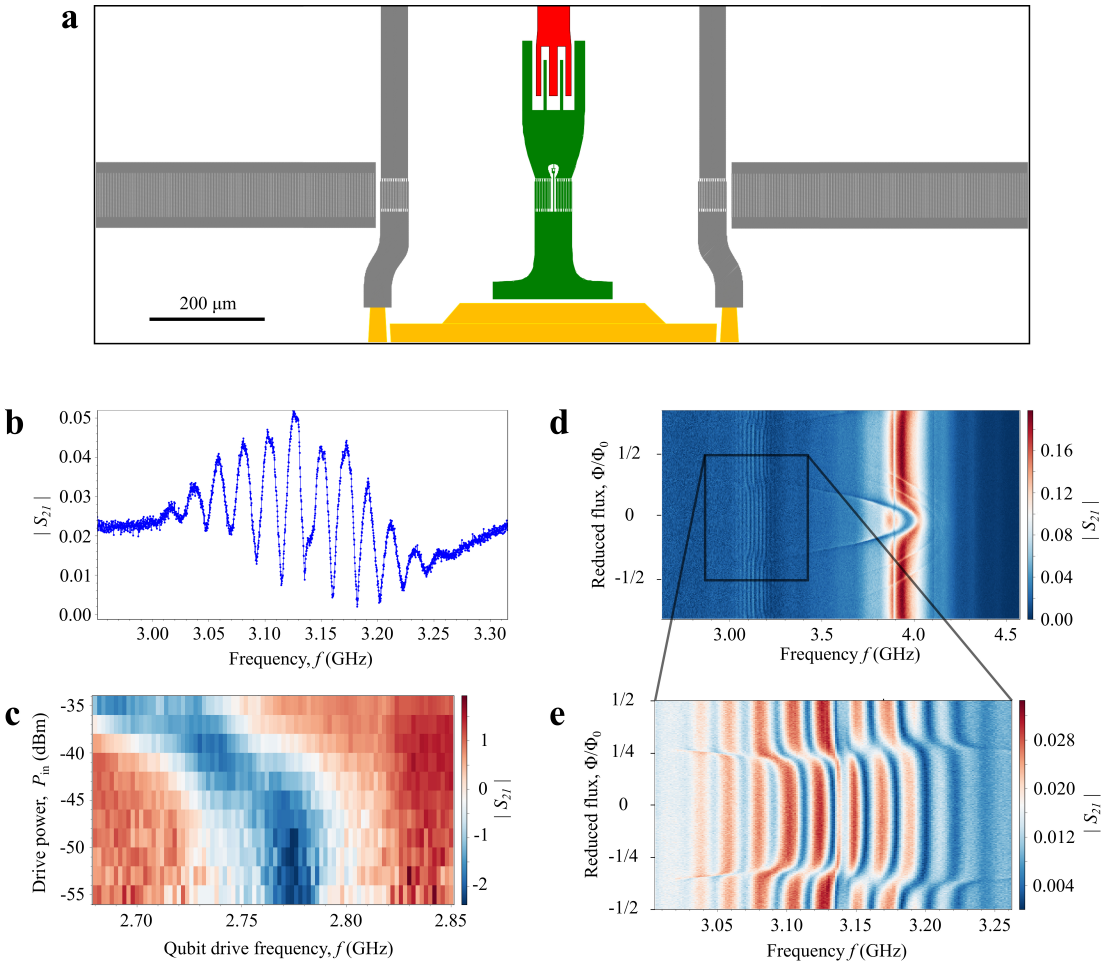

Figure 6.8 | Circuit QAD on diamond. a, CAD design of the device, illustrating the ground planes and waveguides (yellow), the 2-port SAW resonator (dark grey), the transmon (green) and part of the CPWR (red). **b,** Magnitude of the measured transmission coefficient $S_{21}(f)$ of the acoustic cavity. **c,** Qubit spectroscopy (performed with the acoustic cavity) as a function of readout power. **d,** Qubit spectroscopy of the tuneable transmon as a function of flux. **e,** Acoustic cavity response as a function of flux threading the SQUID loop.

Figure 6.8a shows the CAD design of the device. The CPWR is capacitively coupled to the qubit which consists of a SQUID loop shunted by an interdigitated capacitance. The qubit is also capacitively coupled to ground and piezoelectrically coupled to a SAW resonator. The device was fabricated in two steps of electron beam lithography. The geometric parameters related to this device are listed in Table 6.2.

The acoustic cavity resonance is centred around $f_0 = 3.12\,\text{GHz}$ as shown in Fig. 6.8b. The frequency response of the mechanical resonator shows multiple peaks

separated by 28 MHz. This frequency separation should not be confused with the free spectral range of the cavity, since $FSR = v_e/2L_c \approx 8\,\text{MHz}$. The multiple peaks and their frequency separation are probably due to a severe mismatch between the $50\,\Omega$ feedline and the transducer impedance. Further experimental studies are necessary to corroborate this hypothesis.

The piezoelectric coupling between the acoustic cavity and the transmon make it possible to perform spectroscopy of the qubit *via the acoustic cavity* as shown in Fig 6.8c. As expected, the qubit frequency shifts as a function of the input power used to probe the mechanical resonator. This is a clear evidence of an acoustic Stark shift of the qubit.

The qubit spectroscopy indicates possible anti-crossings between the qubit and SAW cavity modes (see Fig 6.8d-e), but these measurements are not easy to interpret conclusively due to the presence of the interference features, which are unlikely to actually be different SAW modes. Nevertheless the strong frequency shifting of the SAW cavity response indicates coupling to the qubit at least on the order of 10 MHz, suggesting that strong coupling between these two quantum systems could in principle have been obtained.

6.10 Conclusions

The prototype quantum acoustic device that we have presented here may be significantly improved, opening up the possibility of using cavity-trapped SAWs for quantum memories, time delays, and quantum signal filtering applications. In particular, we have used a relatively weak piezoelectric substrate for our experiment, nevertheless achieving a qubit-SAWR coupling strength of 5.7 MHz. Stronger piezoelectrics such as lithium niobate or zinc oxide could dramatically increase this coupling strength.

This could have the additional benefit of enabling the qubit coherence to be improved, as the electric field of the qubit could be designed to only partially rather than fully reside in the piezoelectric substrate (which in the present case likely limits coherence due to undesired bulk acoustic emission). The 10^5-times reduced speed of travel of SAWs compared to electromagnetic signals also makes our device a miniaturised mechanical implementation of traditional cavity QED, and an ideal engineered platform to push the boundaries of cavity QED physics, opening up the possibility to explore, for instance, strong coupling multimode cavity QED with mechanical devices.

Qubit	Coulomb energy	$E_{\mathrm{C}} = 0.310\,\mathrm{GHz}$
	Maximum Josephson energy	$E_{\mathrm{J0}} = 10.704\,\mathrm{GHz}$
	$E_{\mathrm{J0}}/E_{\mathrm{C}}$	34.5
	Relaxation time	$T_1 = 46\,\mathrm{ns}$ (at $f_{\mathrm{q}} = 2.6\,\mathrm{GHz}$)
	Dephasing time	$T_2 = 67\,\mathrm{ns}$ (at $f_{\mathrm{q}} = 2.6\,\mathrm{GHz}$)
	Qubit frequency	$f_{\mathrm{q}}(\Phi) = \left(\sqrt{8E_{\mathrm{C}}E_{\mathrm{J0}}\cos\lvert\pi\Phi/\Phi_0\rvert} - E_{\mathrm{C}}\right)/h$
CPWR	Resonance frequency and linewidth	$f_{\mathrm{r}} = 5.83\,\mathrm{GHz}$ $\kappa_{\mathrm{r}} = 3.41\,\mathrm{MHz}$
	Internal and external quality factor	$Q_{\mathrm{r,i}} = 3240$ $Q_{\mathrm{r,e}} = 3630$
	Qubit - CPWR coupling strength	$g = 69\,\mathrm{MHz}$
SAWR	Resonance frequencies and linewidths (in reflection)	$f_{\mathrm{m1}} = 522.825\,\mathrm{MHz}$ $\kappa_{\mathrm{m1}} = 108\,\mathrm{kHz}$ $f_{\mathrm{m2}} = 523.426\,\mathrm{MHz}$ $\kappa_{\mathrm{m2}} = 75\,\mathrm{kHz}$ $f_{\mathrm{m3}} = 524.575\,\mathrm{MHz}$ $\kappa_{\mathrm{m3}} = 69\,\mathrm{kHz}$
	Internal/external quality factors (in reflection)	$Q_{\mathrm{m1,i}} = 4830$ $Q_{\mathrm{m1,e}} = 2.34 \times 10^6$ $Q_{\mathrm{m2,i}} = 7020$ $Q_{\mathrm{m2,e}} = 1.33 \times 10^6$ $Q_{\mathrm{m3,i}} = 7600$ $Q_{\mathrm{m3,e}} = 2.33 \times 10^6$
	Periodicity	$\lambda_0 = 6\,\mu\mathrm{m}$
	Effective speed of sound	$v_{\mathrm{e}} = 3140.6\,\mathrm{m/s}$
	Fingers in each IDT	$N_{\mathrm{t}} = 51$
	Fingers in each grating	$N_{\mathrm{g}} = 400$
	Fingers in the qubit capacitance	$N_{\mathrm{q}} = 31$
	Length of each finger	$W = 70\,\mu\mathrm{m} = 11.66\lambda_0$
	Distance between grating and IDT	$d_1 = (n_1/2 - 1/4)\lambda_0 - \lambda_0/8\lvert_{n_1=3} = 6.75\,\mu\mathrm{m}$
	Distance between gratings	$d = 1260\,\mu\mathrm{m} = v_{\mathrm{e}} \times 401\,\mathrm{ns} =$
	Distance between centre of IDTs	$d_{\mathrm{IDT}} = 1100\,\mu\mathrm{m}$
	Cavity length	$L_{\mathrm{c}} = 1365\,\mu\mathrm{m}$
	Cavity area	$A = W \times L_{\mathrm{c}} = 95900\,\mu\mathrm{m}^2$
	Qubit - SAWR coupling strength	$\lambda_{\mathrm{m2}}(f_{\mathrm{q}} = 2.5\,\mathrm{GHz}) = 5.7\,\mathrm{MHz}$

Table 6.1 | Device parameters of our circuit-QAD architecture on quartz.

SAWR	Resonance frequency	$f_{\mathrm{m0}} = 3.12\,\mathrm{GHz}$
	Periodicity	$\lambda_0 = 3.4\,\mu\mathrm{m}$
	Effective speed of sound	$v_{\mathrm{e}} = 10600\,\mathrm{m/s}$
	Fingers in each IDT	$N_{\mathrm{t}} = 31$
	Fingers in each grating	$N_{\mathrm{g}} = 600$
	Fingers in the qubit capacitance	$N_{\mathrm{q}} = 37$
	Length of each finger	$W = 50\,\mu\mathrm{m} = 14.71\lambda_0$
	Distance between grating and IDT	$d_1 = (n_1/2 - 1/4)\lambda_0 - \lambda_0/8\lvert_{n_1=6} = 8.925\,\mu\mathrm{m}$
	Distance between gratings	$d = 656.25\,\mu\mathrm{m} = v_{\mathrm{e}} \times 62\,\mathrm{ns} =$
	Distance between centre of IDTs	$d_{\mathrm{IDT}} = 586.5\,\mu\mathrm{m}$

Table 6.2 | Device parameters of our circuit-QAD architecture on diamond.

Chapter 7

Conclusions

In this thesis, we have investigated several SAW devices in the quantum regime. Firstly, we performed a systematic characterisation of SAW resonators, showing that their quality factor can reach values of the order of $10^4 - 10^5$ at low temperatures. We showed that the performance of these resonators is strictly related to their geometry and design. In particular, the quality factor of SAW cavities decreases in a polynomial way as a function of frequency. We also observed a weak drive power dependence of their internal quality factor that saturates at low power consistent with coupling to a bath of two-level systems. Furthermore, time-domain measurements directly showed the acoustic nature of these cavities. This preliminary study strongly suggests that SAW resonators are promising devices for integration with superconducting quantum circuits and artificial atoms.

Secondly, we have successfully measured superconducting qubits on quartz and diamond. These devices have been probed inside 3D cavities with a typical 3D circuit quantum electrodynamics platform. The values of T1 and T2 have been extracted with standard Rabi and Ramsey fringe experiments. The measured coherence time of the qubits was found to be of the order of $1\,\mu$s. Their coherence was long enough to proceed with more advanced experiments in which the coherent interaction between a SAW resonator and a superconducting qubit was explored.

Thirdly, we presented measurements of a device in which a tuneable transmon qubit is piezoelectrically coupled to a surface acoustic wave cavity, displaying a surface acoustic version of cavity QED which we call circuit quantum acoustodynamics. We have characterised the dispersive interaction between the two systems in several ways including the measurement of the frequency shift of the acoustic mode as the qubit is flux tuned and the measurement of the acoustic Stark shift of the qubit due to the population of the mechanical resonator. We have also performed qubit spectroscopy using the SAW resonator as readout component, proving that these acoustic cavities are a viable alternative for qubit readout schemes in quantum information processors.

Finally, we presented preliminary measurements of direct coupling between a superconducting qubit and a SAW cavity on a Si/diamond/AlN substrate. This exploratory study indicates that the strong coupling between these two quantum systems is within reach.

7.1 Outlook

Our architecture can be improved in several ways; for instance, it would be possible to deposit piezoelectric films only on specific parts of the chip. In this way, electrical components not used for transduction (such as CPWRs and qubits) could be fabricated on non-piezoelectric areas of the device, potentially enabling better performance. Furthermore, by engineering the cavity length of the device such that the FSR is in the order of $15 - 20\,\mathrm{MHz}$, it would be possible to observe the coupling between a $\sim 3\,\mathrm{GHz}$ multimode resonator and a superconducting qubit with a linewidth of few MHz, realising an acoustic version of multimode circuit quantum electrodynamics.

The intrinsic advantage of circuit QAD platforms will be fully exploited once the

transfer of quantum information between delocalised qubits on a chip is obtained by means of acoustic waves. The slow speed of the mechanical wave will give the possibility to manipulate the qubit state while the wave is still travelling, an exquisite feature of these acoustic devices. Furthermore, in traditional quantum optics where the interaction between atoms and light at optical frequencies is investigated, the atoms are usually approximated as point-like when compared to the wavelength of the incoming wave. This approximation is no longer valid in the field of quantum acoustics, where superconducting qubits are several wavelengths long opening up a new physical regime not yet explored. Lastly, the high performance of SAW cavities at 500 MHz suggests that they will soon find interesting applications in the field of optomechanics.

Bibliography

[1] B. Abbott et al. Observation of a kilogram-scale oscillator near its quantum ground state. *New J. Phys.*, 11:073032, 2009. (Cited on page 5).

[2] L. Allen and J. Eberly. *Optical resonance and two-level atoms.* Dover, 1987. (Cited on page 120).

[3] P. W. Anderson, B. I. Halperin, and C. M. Varma. Anomalous low-temperature thermal properties of glasses and spin glasses. *Philosophical Magazine*, 25(1):1–9, 1972. (Cited on page 100).

[4] R. W. Andrews, R. W. Peterson, T. P. Purdy, K. Cicak, R. W. Simmonds, C. A. Regal, and K. W. Lehnert. Bidirectional and efficient conversion between microwave and optical light. *Nat Phys*, 10(4):321–326, 2014. (Cited on page 6, 58).

[5] T. Aref, P. Delsing, M. K. Ekström, A. F. Kockum, M. V. Gustafsson, G. Johansson, P. J. Leek, E. Magnusson, and R. Manenti. *Quantum Acoustics with Surface Acoustic Waves*, pages 217–244. Springer International Publishing, 2016. (Cited on page 6, 7, 60, 103).

[6] E. A. Ash. Surface Wave Grating Reflectors and Resonators. In *G-MTT 1970 International Microwave Symposium*, pages 385–386, May 1970. (Cited on page 8).

[7] M. Aspelmeyer, T. J. Kippenberg, and F. Marquardt. Cavity optomechanics. *Rev. Mod. Phys.*, 86(4):1391, 2014. (Cited on page 6).

[8] C. Axline, M. Reagor, R. Heeres, P. Reinhold, C. Wang, K. Shain, W. Pfaff, Y. Chu, L. Frunzio, and R. J. Schoelkopf. An architecture for integrating planar and 3D cQED devices. *Appl. Phys. Lett.*, 109:042601, 2016. (Cited on page 69).

[9] D. T. Bell and R. C. M. Li. Surface-Acoustic-Wave resonators. *Proc. IEEE*, 64:711, 1976. (Cited on page 8, 95, 96).

[10] M. Boissonneault, J. M. Gambetta, and A. Blais. Dispersive regime of circuit QED: Photon-dependent qubit dephasing and relaxation rates. *Phys. Rev. A*, 79:013819, Jan 2009. (Cited on page 143).

[11] A. N. Bolgar, J. I. Zotova, D. D. Kirichenko, I. S. Besedin, A. V. Semenov, R. S. Shaikhaidarov, and O. V. Astafiev. Experimental demonstration of a two-dimensional phonon cavity in the quantum regime. *arXiv:1710.06476*, 2017. (Cited on page 129).

[12] V. Bouchiat, D. Vion, P. Joyez, D. Esteve, and M. H. Devoret. Quantum coherence with a single Cooper pair. *Physica Scripta*, pages 165–170, 1998. (Cited on page 43, 45).

[13] T. Brecht, M. Reagor, Y. Chu, W. Pfaff, C. Wang, L. Frunzio, M. H. Devoret, and R. J. Schoelkopf. Demonstration of superconducting micromachined cavities. *Appl. Phys. Lett.*, 107:192603, 2015. (Cited on page 87).

[14] A. Bruno, G. de Lange, S. Asaad, K. van der Enden, N. K. Langford, and L. DiCarlo. Reducing intrinsic loss in superconducting resonators by surface treatment and deep etching of silicon substrates. *Appl. Phys. Lett.*, 106:182601, 2015. (Cited on page 89).

[15] A. J. Budreau and P. H. Carr. Temperature dependence of the attenuation of microwave frequency elastic surface waves in quartz. *Appl. Phys. Lett.*, 18:239, 1971. (Cited on page 8).

[16] M. Buttiker. Zero-current persistent potential drop across small-capacitance Josephson junctions. *Physical Review B*, 36(7):3548, 1987. (Cited on page 43).

[17] S. Büyükköse, B. Vratzov, D. Atacand J. van der Veen, P. V. Santos, and W. G. van der Wiel. Ultrahigh-frequency surface acoustic wave transducers on ZnO/SiO2/Si using nanoimprint lithography. *Nanotechnology*, 23:315303, 2012. (Cited on page 8).

[18] O. Carnal and J. Mlynek. Young's double-slit experiment with atoms: A simple atom interferometer. *Phys. Rev. Lett.*, 66:2689–2692, 1991. (Cited on page 4).

[19] J. Chan, T. P. M. Alegre, A. H. Safavi-Naeini, J. T. Hill, A. Krause, S. Gröblacher, M. Aspelmeyer, and O. Painter. Laser cooling of a nanomechanical oscillator into its quantum ground state. *Nature*, 478(89-92), 2011. (Cited on page 5, 6, 57).

[20] J. Chaste, M. Sledzinska, M. Zdrojek, J. Moser, and A. Bachtold. High-frequency nanotube mechanical resonators. *Appl. Phys. Lett.*, 99:213502, 2011. (Cited on page 5).

[21] Y. Chu, P. Kharel, W. H. Renninger, L. D. Burkhart, L. Frunzio, P. T. Rakich, and R. J. Schoelkopf. Quantum acoustics with superconducting qubits. *Science*, 2017. (Cited on page 59, 129).

[22] J. Clarke and F. K. Wilhelm. Superconducting quantum bits. *Nature*, 453:1031–1042, 2008. (Cited on page 43).

[23] A. Cottet. *Implementation of a quantum bit in a superconducting circuit*. PhD thesis, l'Universite Paris VI, 2002. (Cited on page 47).

[24] P. S. Cross. Reflective Arrays for SAW Resonators. In *1975 Ultrasonics Symposium*, pages 241–244, Sept 1975. (Cited on page 41, 130).

[25] S. Eibenberger, S. Gerlich, M. Arndt, M. Mayor, and J. Tüxen. Matter wave interference of particles selected from a molecular library with masses exceeding 10 000 amu. *Phys. Chem. Chem. Phys.*, 15:14696–14700, 2013. (Cited on page 5).

[26] K. L. Ekinci and M. L. Roukes. Nanoelectromechanical systems. *Rev. Sci. Instrum.*, 76:061101, 2005. (Cited on page 5).

[27] M. K. Ekström, T. Aref, J. Runeson, J. Björck, and I. Boström. Surface acoustic wave unidirectional transducers for quantum applications. *Appl. Phys. Letters*, 110:073105, 2017. (Cited on page 60).

[28] S. Galliou, M. Goryachev, R. Bourquin, P. Abbe, J. P. Aubry, and M. E. Tobar. Extremely Low Loss Phonon-Trapping Cryogenic Acoustic Cavities for Future Physical Experiments. *Sci. Rep.*, 3, 2013. (Cited on page 106).

[29] J. Gao, M. Daal, A. Vayonakis, S. Kumar, J. Zmuidzinas, B. Sadoulet, B. A. Mazin, P. K. Day, and H. G. Leduc. Experimental evidence for a surface distribution of two-level systems in superconducting lithographed microwave resonators. *Appl. Phys. Lett.*, 92:152505, 2008. (Cited on page 106).

[30] C. Gerry and P. Knight. *Introductory Quantum Optics*. Cambridge University Press, 2005. (Cited on page 56).

[31] D. A. Golter, T. Oo, M. Amezcua, I. Lekavicius, K. A. Stewart, and H. Wang. Coupling a Surface Acoustic Wave to an Electron Spin in Diamond via a Dark State. *Phys. Rev. X*, 6:041060, 2016. (Cited on page 60).

[32] M. Goryachev, D. L. Creedon, E. N. Ivanov, S. Galliou, R. Bourquin, and M. E. Tobar. Extremely low-loss acoustic phonons in a quartz bulk acoustic wave resonator at millikelvin temperature. *Appl. Phys. Lett.*, 100:243504, 2012. (Cited on page 106).

[33] L. Guo, A. Grimsmo, A. F. Kockum, M. Pletyukhov, and G. Johansson. Giant acoustic atom: A single quantum system with a deterministic time delay. *Phys. Rev. A*, 95:053821, 2017. (Cited on page 60).

[34] M. V. Gustafsson, T. Aref, A. F. Kockum, M. K. Ekström, G. Johansson, and P. Delsing. Propagating phonons coupled to an artificial atom. *Science*, 346:207–211, 2014. (Cited on page 6, 8).

[35] M. V. Gustafsson, P. V. Santos, G. Johansson, and P. Delsing. Local probing of propagating acoustic waves in a gigahertz echo chamber. *Nat. Phys.*, 8:338–343, 2012. (Cited on page 8, 59).

[36] A. El Habti, F. Bastien, E. Bigler, and T. Thorvaldsson. High-frequency surface acoustic wave devices at very low temperature: Application to loss mechanisms evaluation. *J. Acoust. Soc. Am.*, 100:272–277, 1996. (Cited on page 8, 59, 97).

[37] W. Heisenberg. Über quantentheoretische Umdeutung kinematischer und mechanischer Beziehungen. *Zeitschrift für Physik*, 33(1):879–893, 1925. (Cited on page 4).

[38] P. Heyliger, Hassel Ledbetter, and Sudook Kim. Elastic constants of natural quartz. *J. Acoust. Soc. Am.*, 114:644–650, 2003. (Cited on page 20).

[39] S. Hunklinger and W. Arnold. *Ultrasonic Properties of Glasses at Low Temperatures*, page 155. Academic Press, 1980. (Cited on page 100).

[40] M. Imboden, P. Mohanty, A. Gaidarzhy, J. Rankin, and B. W. Sheldon. Scaling of dissipation in megahertz-range micromechanical diamond oscillators. *Appl. Phys. Lett.*, 90(17), 2007. (Cited on page 5).

[41] J. R. Johansson, P. D. Nation, and F. Nori. QuTiP 2: A Python framework for the dynamics of open quantum systems. *Computer Physics Communications*, 184(4):1234–1240, 2013. (Cited on page 141).

[42] C. Jönsson. Electron diffraction at multiple slits. *Am. J. Phys.*, 42:4–11, 1974. (Cited on page 4).

[43] J. Koch, T. M. Yu, J. Gambetta, A. A. Houck, D. I. Schuster, J. Majer, A. Blais, M. H. Devoret, S. M. Girvin, and R. J. Schoelkopf. Charge-insensitive qubit design derived from the Cooper pair box. *Phys. Rev. A*, 76:042319, Oct 2007. (Cited on page 43, 50, 57, 85, 123, 124, 128, 138, 141).

[44] A. F. Kockum, P. Delsing, and G. Johansson. Designing frequency-dependent relaxation rates and Lamb shifts for a giant artificial atom. *Phys. Rev. A*, 90:013837, 2014. (Cited on page 7, 60).

[45] M. D. LaHaye, J. Suh, P. M. Echternach, K. C. Schwab, and M. L. Roukes. Nanomechanical measurements of a superconducting qubit. *Nature*, 459(7249):960–964, 2009. (Cited on page 6, 58).

[46] F. Lecocq, I. M. Pop, Z. Peng, I. Matei, T. Crozes, T. Fournier, C. Naud, W. Guichard, and O. Buisson. Junction fabrication by shadow evaporation without a suspended bridge. *Nanotechnology*, page 315302, 2011. (Cited on page 93).

[47] F. Lecocq, J. D. Teufel, J. Aumentado, and R. W. Simmonds. Resolving the vacuum fluctuations of an optomechanical system using an artificial atom. *Nat. Phys.*, 11:635 – 639, 2015. (Cited on page 58).

[48] R. C. M. Li, R. C. Williamson, D. C. Flanders, and J. A. Alusow. On the Performance and Limitations of the Surface-Wave Resonator Using Grooved Reflectors. *Ultrasonics Symposium*, pages 257–262, 1974. (Cited on page 92, 98).

[49] P. Macha, S. H. W. van de Ploeg, G. Oelsner, E. Il'ichev, H. G. Meyer, S. Wünsch, and M. Siegel. Losses in coplanar waveguide resonators at millikelvin temperatures. *Appl. Phys. Lett.*, 96:062503, 2010. (Cited on page 106).

[50] E. B. Magnusson, B. H. Williams, R. Manenti, M. S. Nam, A. Nersisyan, M. J. Peterer, A. Ardavan, and P. J. Leek. Surface acoustic wave devices on bulk ZnO at low temperature. *Appl. Phys. Lett.*, 106:063509, 2015. (Cited on page 7, 60).

[51] R. Manenti, A. F. Kockum, A. Patterson, T. Behrle, J. Rahamim, G. Tancredi, F. Nori, and P. J. Leek. Circuit quantum acoustodynamics with surface acoustic waves. *Nat. Comm.*, 8, October 2017. (Cited on page 8, 129).

[52] R. Manenti, M. J. Peterer, A. Nersisyan, E. B. Magnusson, A. Patterson, and P. J. Leek. Surface acoustic wave resonators in the quantum regime. *Phys. Rev. B*, 93:041411, Jan 2016. (Cited on page 7).

[53] A. A. Maradudin and D. L. Mills. Calculation of the Anharmonic Damping of Rayleigh Surface Modes. *Phys. Rev.*, 173:881–898, Sep 1968. (Cited on page 8, 59).

[54] H. J. Maris. On the mean free path of low energy phonons in single crystal quartz. *Philosophical Magazine*, 9(102):901–910, 1964. (Cited on page 96, 97).

[55] H. J. Maris. *Interaction of Sound Waves with Thermal Phonons in Dielectric Crystals*, page 279. Academic Press, 1971. (Cited on page 97).

[56] F. Massel, T. T. Heikkila, J. M. Pirkkalainen, S. U. Cho, H. Saloniemi, P. J. Hakonen, and M. A. Sillanpää. Microwave amplification with nanomechanical resonators. *Nature*, 480(7377):351–354, 2011. (Cited on page 6, 58).

[57] Th. K. Mavrogordatos, G. Tancredi, M. Elliott, M. J. Peterer, A. Patterson, J. Rahamim, P. J. Leek, E. Ginossar, and M. H. Szymańska. Simultaneous Bistability of a Qubit and Resonator in Circuit Quantum Electrodynamics. *Phys. Rev. Lett.*, 118:040402, 2017. (Cited on page 114).

[58] S. M. Meenehan, J. D. Cohen, S. Gröblacher, J. T. Hill, A. H. Safavi-Naeini, M. Aspelmeyer, and O. Painter. Silicon optomechanical crystal resonator at millikelvin temperatures. *Phys. Rev. A*, 90:011803, 2014. (Cited on page 5).

[59] A. Megrant, C. Neill, R. Barends, B. Chiaro, Yu Chen, L. Feigl, J. Kelly, E. Lucero, M. Mariantoni, P. J. J. O'Malley, D. Sank, A. Vainsencher, J. Wenner, T. C. White, Y. Yin, J. Zhao, C. J. Palmstrøm, J. M. Martinis, and A. N. Cleland. Planar superconducting resonators with internal quality factors above one million. *Appl. Phys. Lett.*, 100:113510, 2012. (Cited on page 106).

[60] B. A. Moores, L. R. Sletten, J. J. Viennot, and K. W. Lehnert. Cavity quantum acoustic device in the multimode strong coupling regime. *arXiv:1711.05913*. (Cited on page 129).

[61] D. P. Morgan. History of SAW devices. In *Proceedings of the 1998 IEEE International Frequency Control Symposium (Cat. No.98CH36165)*, pages 439–460, May 1998. (Cited on page 8).

[62] D. P. Morgan. *Surface Acoustic Wave Filters*. Academic Press, Amsterdam, 2007. (Cited on page 7, 8, 36, 42, 102, 137).

[63] O. Nairz, M. Arndt, and A. Zeilinger. Quantum interference experiments with large molecules. *Am. J. Phys.*, 71:319, 2003. (Cited on page 4).

[64] Y. Nakamura, Y. A. Pashkin, and J. S. Tsai. Coherent control of macroscopic quantum states in a single-Cooper-pair box. *Nature*, 398:786, 1999. (Cited on page 43).

[65] A. Noguchi, R. Yamazaki, Y. Tabuchi, and Y. Nakamura. Qubit-Assisted Transduction for a Detection of Surface Acoustic Waves near the Quantum Limit. *Phys. Rev. Lett.*, 119:180505, Nov 2017. (Cited on page 129).

[66] A. D. O'Connell, M. Hofheinz, M. Ansmann, R. C. Bialczak, M. Lenander, E. Lucero, M. Neeley, D. Sank, H. Wang, M. Weides, J. Wenner, J. M. Martinis, and A. N. Cleland. Quantum ground state and single-phonon control of a mechanical resonator. *Nature*, 464:697–703, 2010. (Cited on page 5, 6, 58, 59).

[67] A. Okada, F. Oguro, A. Noguchi, Y. Tabuchi, R. Yamazaki, K. Usami, and Y. Nakamura. Cavity optomechanics with surface acoustic waves. *https://arxiv.org/abs/1705.04593*, 2017. (Cited on page 60, 129).

[68] T. A. Palomaki, J. W. Harlow, J. D. Teufel, R. W. Simmonds, and K. W. Lehnert. Coherent state transfer between itinerant microwave fields and a mechanical oscillator. *Nature*, 495(7440):210–214, 2013. (Cited on page 6).

[69] T. E. Parker and G. K. Montress. Precision surface-acoustic-wave (SAW) oscillators. *IEEE Transactions on Ultrasonics, Ferroelectrics, and Frequency Control*, 35(3):342–364, 1988. (Cited on page 8, 92, 95).

[70] W. A. Phillips. Two-level states in glasses. *Rep. Prog. Phys.*, 50:1657–1708, 1987. (Cited on page 99, 100).

[71] J.-M. Pirkkalainen, S. U. Cho, Jian Li, G. S. Paraoanu, P. J. Hakonen, and M. A. Sillanpää. Hybrid circuit cavity quantum electrodynamics with a micromechanical resonator. *Nature*, 494:211–215, 2013. (Cited on page 6, 59).

[72] J.-M. Pirkkalainen, E. Damskägg, M. Brandt, F. Massel, and M. A. Sillanpää. Squeezing of Quantum Noise of Motion in a Micromechanical Resonator. *Phys. Rev. Lett.*, 115:243601, Dec 2015. (Cited on page 6).

[73] M. Poot and H. S. J. van der Zant. Mechanical systems in the quantum regime. *Phy. Rep.*, 511:273–335, 2012. (Cited on page 5).

[74] D. N. Pozar. *Microwave Engineering*. Wiley Inter-Science, 1990. (Cited on page 38, 86).

[75] J. Rahamim, T. Behrle, M. J. Peterer, A. Patterson, P. Spring, T. Tsunoda, R. Manenti, G. Tancredi, and P. J. Leek. Double-sided coaxial circuit QED with out-of-plane wiring. *Appl. Phys. Lett.*, 110:222602, 2017. (Cited on page 69).

[76] R. Riedinger, S. Hong, R. A. Norte, J. A. Slater, J. Shang, A. G. Krause, V. Anant, M. Aspelmeyer, and S. Gröblacher. Non-classical correlations between single photons and phonons from a mechanical oscillator. *Nature*, 530(7590):313–316, 2016. (Cited on page 6).

[77] J. G. Rodrguez-Madrid, G. F. Iriarte, J. Pedrs, O. A. Williams, D. Brink, and F. Calle. Super-High-Frequency SAW Resonators on AlN/Diamond. *IEEE ELECTRON DEVICE LETTERS*, 33(4), 2012. (Cited on page 145).

[78] F. Rouxinol, Y. Hao, F. Brito, A. O. Caldeira, E. K. Irish, and M. D. LaHaye. Measurements of nanoresonator-qubit interactions in a hybrid quantum electromechanical system. *Nanotechnology*, 27:364003, 2016. (Cited on page 6, 59).

[79] D. Royer and E. Dieulesaint. *Elastic Waves in Solids I: Free and Guided Propagation*. Springer-Verlag, 2000. (Cited on page 27).

[80] T. Sakuma and T. Nakayama. Attenuation of elastic surface waves by anharmonic interactions at low temperatures. *Appl. Phys. Lett.*, 25(4):176–177, 1974. (Cited on page 97, 105).

[81] E. Salzmann, T. Plieninger, and K. Dransfeld. Attenuation of elastic surface waves in quartz at frequencies of 316 MHz and 1047 MHz. *Appl. Phys. Lett.*, 13, 1968. (Cited on page 59, 97).

[82] E. Schrödinger. Quantisierung als Eigenwertproblem. *Annalen der Physik*, 384(4):361–376, 1926. (Cited on page 4).

[83] M. J. A. Schuetz, E. M. Kessler, G. Giedke, L. M. K. Vandersypen, M. D. Lukin, and J. I. Cirac. Universal Quantum Transducers Based on Surface Acoustic Waves. *Phys. Rev. X*, 5:031031, 2015. (Cited on page 7, 30, 60, 137).

[84] V. S. Shumeiko. Quantum acousto-optic transducer for superconducting qubits. *Phys. Rev. A*, 93:023838, Feb 2016. (Cited on page 7, 60).

[85] A. J. Slobodnik. *Materials and Their Influence on Performance*, page 225. Springer, 1978. (Cited on page 98).

[86] Lord Rayleigh (J. Strutt). On waves propagated along the plane surface of an elastic solid. *Proc. London Math. Soc.*, 17:4–11, 1885. (Cited on page 30).

[87] W. J. Tanski. Surface Acoustic Wave Resonators on Quartz. *IEEE Transactions on Sonics and Ultrasonics*, 26(2):93–104, March 1979. (Cited on page 8).

[88] J. D. Teufel, T. Donner, Dale Li, J. W. Harlow, M. S. Allman, K. Cicak, A. J. Sirois, J. D. Whittaker, K. W. Lehnert, and R. W. Simmonds. Sideband cooling of micromechanical motion to the quantum ground state. *Nature*, 475(7356):359–363, 2011. (Cited on page 6, 57).

[89] A. Tonomura, J. Endo, T. Matsuda, T. Kawasaki, and H. Ezawa. Demonstration of single-electron buildup of an interference pattern. *American Journal of Physics*, 57:117, 1989. (Cited on page 4).

[90] T. Uno and H. Jumonji. Optimization of quartz SAW resonator structure with groove gratings. *IEEE Trans. on Sonics and Ultrasonics*, 29(6):299–309, 1982. (Cited on page 135).

[91] D. Vion, A. Aassime, A. Cottet, P. Joyez, H. Pothier, C. Urbina, D. Esteve, and M. H. Devoret. Manipulating the Quantum State of an Electrical Circuit. *Science*, 296:886–889, 2002. (Cited on page 48).

[92] A. Wallraff, D. I. Schuster, A. Blais, L. Frunzio, R. S. Huang, J. Majer, S. Kumar, S. M. Girvin, and R. J. Schoelkopf. Strong coupling of a single photon to a superconducting qubit using circuit quantum electrodynamics. *Nature*, 431(7005):162–167, 2004. (Cited on page 6, 43, 56).

[93] A. Wallraff, D. I. Schuster, A. Blais, L. Frunzio, J. Majer, M. H. Devoret, S. M. Girvin, and R. J. Schoelkopf. Approaching Unit Visibility for Control of a Superconducting Qubit with Dispersive Readout. *Phys. Rev. Lett.*, 95:060501, Aug 2005. (Cited on page 131, 143).

[94] E. E. Wollman, C. U. Lei, A. J. Weinstein, J. Suh, A. Kronwald, F. Marquardt, A. A. Clerk, and K. C. Schwab. Quantum squeezing of motion in a mechanical resonator. *Science*, 349(6251):952–955, 2015. (Cited on page 6).

[95] E. E. Wollman, C. U. Lei, A. J. Weinstein, J. Suh, A. Kronwald, F. Marquardt, A. A. Clerk, and K. C. Schwab. Quantum squeezing of motion in a mechanical resonator. *Science*, 349(6251):952–955, 2015. (Cited on page 58).

[96] K. Yamanouchi, H. Nakagawa, J. A. Qureshi, and H. Odagawa. 10 GHz-Range Surface Acoustic Wave Low Loss Filter Measured at Low Temperature. *Japanese Journal of Applied Physics*, 38(5B), 1999. (Cited on page 8, 59).

[97] A. Zeilinger, R. Gähler, C. G. Shull, W. Treimer, and W. Mampe. Single and double-slit diffraction of neutrons. *Rev. Mod. Phys.*, 60:1067–1073, 1988. (Cited on page 4).